

NOTE TO USERS

This reproduction is the best copy available.

UMI[®]

NUCLEAR MAGNETIC RESONANCE STUDIES OF RELAXOR
FERROELECTRICS

A Dissertation

Presented to

The Faculty of the Department of Physics
The College of William and Mary in Virginia

In Partial Fulfillment

Of the Requirements for the Degree of

Doctor of Philosophy

by


William J. Brouwer

2005

APPROVAL SHEET

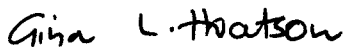
This dissertation is submitted in partial fulfillment of
the requirements for the degree of

Doctor of Philosophy



William J. Brouwer

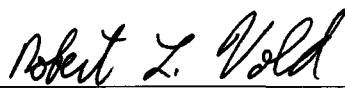
Approved by the Committee, October 2005



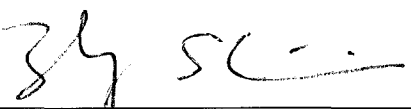
Gina Hoatson, Chair




Henry Krakauer



Robert Vold



Shiwei Zhang



Robert Michael Lewis, Department of Mathematics

For Rebecca

TABLE OF CONTENTS

Acknowledgements	vii
List of Tables	viii
List of Figures	ix
Abstract	xv
Chapter	
1 Introduction	2
2 Nuclear Magnetic Resonance	4
2.1 Spin and Zeeman Levels	4
2.2 Internal Interactions	9
2.2.1 Quadrupole Coupling	9
2.2.2 Chemical Shift Interaction	14
2.3 The Density Operator	19
2.3.1 Time Evolution of the density operator	21
2.4 Experimental NMR	25
2.4.1 Average Hamiltonian	25
2.4.2 Phase Cycling	33
2.4.3 Data Acquisition	38
2.4.4 Lineshape Simulation	46
2.4.5 Enhanced Resolution in Disordered Systems	49

3	Ferroelectric Materials	61
3.1	Crystal Chemistry	61
3.2	Ferroelectrics	64
4	Calculations	69
4.1	Simulating the ionic lattice	69
4.2	Electric Field Gradient	75
4.3	Chemical Shift	78
4.3.1	Distribution Models and Lineshape Simulation	83
5	Experiment	87
5.1	Lead Scandium Tantalate (PST) 3QMAS	87
5.1.1	Results	88
5.1.2	Calculations	91
5.2	Model Compounds	92
5.3	(1-x)PSW-xPT/PZ Magic Angle Spinning	97
5.4	(1-x)PSW-xPT/PZ 3QMAS experiments	108
5.4.1	Calculations	114
5.5	Three Dimensional, Multiple Quantum MAS	117
6	Conclusions	123
Appendix A		
	Elementary Group Theory	127
A.0.1	Angular Momentum	131
Appendix B		
	Data Processing	135
Appendix C		
	Computer Programs	138
	Bibliography	156

Vita 164

ACKNOWLEDGEMENTS

Naturally I am indebted to my advisers Drs G. L. Hoatson and R. L. Vold for several years of guidance, encouragement, and the occasional (frequent) indulgence of my own scientific curiosity. I would also acknowledge my committee members who also assisted in my overall development. They were chosen because they have all at some point provided me with superior teaching or at the very least a kind word when it probably wasn't expected or deserved. I am grateful for my present (and past) colleagues with whom I enjoy warm friendship and vibrant humor. However, it was the support of my parents and most recently my dear, loving wife that chiefly brought me to this point, and it is to them that I owe the most. Their example of love through personal sacrifice is something I have yet to return fully, although I know it was offered unconditionally.

LIST OF TABLES

2.1	Phase cycle for split-t1 (whole echo) MQMAS experiment.	37
2.2	Powder averaging schemes	48
4.1	Summary of results at room temperature for SPuDS calculations. .	70
4.2	Structural parameters for undistorted PSW	72
5.1	Deconvolutions for ^{45}Sc MAS at 7T, of several model scandium compounds.	95
5.2	Deconvolutions for ^{45}Sc 3QMAS, 17.6T of scandium oxide and sulfate.	95
5.3	Scandium Oxide unit cell (Ia-3) parameters	97
5.4	MAS deconvolutions for (1-x)PSW-xPT, ^{45}Sc , 19.6T, $\nu_r = 10\text{kHz}$	106
5.5	MAS deconvolutions for (1-x)PSW-xPZ, ^{45}Sc , 19.6T, $\nu_r = 10\text{kHz}$	106
5.6	Parameter distributions for solid solutions (1-x)PSW-xPZ/PT . . .	114
5.7	Phase cycle for 3D-MQMAS experiment	119
A.1	Proper covering operations of the group D_4	128

LIST OF FIGURES

2.1	Euler angles for: (a) the Principal Axis System (PAS) in the crystal frame (b) PAS in rotor fixed frame, (c) PAS and rotor relationship to static B field.	30
2.2	A trivial three pulse experiment with phase cycle, showing the behavior of complex amplitude for two coherence transfer pathways. .	36
2.3	Cumulative sums of coherence transfer pathways for split t_1 MQ-MAS experiment. Phase cycling successfully eliminates all but desired pathway, the unwanted pathways having different numerical periodicities.	37
2.4	Block schematic for a Fourier transform NMR spectrometer. Radio frequency energy is pulsed and after gain gated into the sample within RF coil (the probe). A system response is acquired by the receiver and after sufficient gain and demodulation using the Intermediate Frequency (IF), digitized and processed. Control and processing functions are carried out by a combination of software and hardware.	39
2.5	Frequency spectrum of the absorption Lorentzian; frequency 159.15 Hz, broadening or full width at half maximum height 500 Hz	41
2.6	Frequency spectrum of the dispersion Lorentzian; frequency 159.15 Hz, broadening or full width at half maximum height 500 Hz	42
2.7	Block schematic for single pulse experiment. Pulse duration p_1 , power level pl_1 , phase ph_1 . Acquisition time is t_1	43
2.8	Block schematic for two dimensional NMR experiment. Fourier transforms are performed for direct and indirect dimensions t_2 and t_1 respectively.	44

2.9	Phase twist peaks in the real component of the 2D FFT of the Lorentzian $\exp(-(0.6 + i)x) \exp(-(0.6 + i)y)$; x and y are two independent time variables and it is assumed that the dwell time was 0.2 ms i.e., a frequency sweep-width of ± 2500 Hz	56
2.10	Simulated powder pattern for the three distinct chemical sites in scandium sulfate, for ^{45}Sc MAS at 17.6T	57
2.11	Simulated spectrum for scandium sulfate, ^{45}Sc 3QMAS at 17.6T. The number of frequency grid points is 331×41 ($F2 \times F1$), 633 powder increments for each site, 30 Hz line broadening. Left to right, site parameters for chemical shift are -6.1, 2.4 and 4.5 ppm, with respect to Scandium Chloride reference. Quadrupole coupling constants C_Q are 4.6, 4.2 and 5.5 MHz, and asymmetry parameter η 0.5, 0.9, 0.1	58
2.12	(Top) ^{87}Rb Double Quantum Filtered STMAS at 17.6T and 15 kHz spinning speed. (Bottom) 1D Slices, parallel to F2, taken through frequencies as indicated in F1, corresponding to distinct chemical sites.	59
2.13	(a) Proposed three dimensional multiple quantum MAS experiment. Pulse block 1 represents a double quantum filter and pulse block 2 a triple quantum filter. Pulse five and delay τ_z comprise the z-filter, with a selective 90 degree pulse for detection. (b) Coherence transfer pathway for 3D-MQMAS	60
3.1	Simple model of microscopic domains in two dimensions, through displaced A anions and B cations.	65
3.2	The four phases of ferroelectric Barium Titanate. The phase transitions occur over narrow temperature ranges, in distinction to the relaxor ferroelectrics. All ferroelectrics are distinguished by the absence of polarization above the Curie temperature.	66
4.1	Space group $\text{Im}\bar{3}m$, with tilt system $a^0b^-b^-$ and 1:1 order along $[1,1,1]$. Red and green octahedra illustrate the different species on the B-site.	73

4.2	(Left) quadrupole coupling constant and (right) asymmetry parameter distributions for PSW. The lattice size was $17 \times 17 \times 17$, with 0.15 radians tilting in the Imma system. Random site (β') unit cells were 1.18 times as large as β' unit cells, lead are displaced 0.1 Angstroms along $[-1,0,0]$ and B site atoms are displaced randomly along the major axis of octahedra, up to 0.1 Angstroms.	77
4.3	Convergence of electric field gradient calculation, proportional to $1/r^3$, versus radius from central scandium ion in RS model for ordering in PSW.	78
4.4	Divergence of sum in chemical shift calculation, versus radii from central scandium ion in RS model for ordering in PSW.	83
4.5	Distribution of quadrupole coupling constant in PSW, using RS model for ordering with no structural distortions.	84
4.6	Gamma distribution for various values of a	85
5.1	^{45}Sc MAS spectra of PST at 17.6 T and 20kHz spinning speed. Clearly visible are peaks at 125.4ppm and 159.9ppm, with respect to ScCl_3 reference. The smaller peak most likely corresponds to small amounts of Scandium in the pure Tantalum layer.	88
5.2	Experimental spectra (top) for PST, 3QMAS at 19.6T, with simulation (bottom)	89
5.3	Experimental and simulated (broken line) 3QMAS F2 projection for PST, 7T	90
5.4	Calculated C_Q distribution with least squares fit. Mean and standard deviation are 2.8 and 0.9 MHz, respectively. These are slightly lower than experimental values, perhaps due to the presence of covalency.	91

5.5	(Top) Plot of interaction energy versus x and y coordinates for lead in an undistorted perovskite lattice. Interaction energy is calculated in a point charge model between lead, first shell (12 Oxygen) and second shell (8 B sites), for cubic symmetry and no oxygen distortions. Out of four possible directions for displacement, none are more likely. (Bottom) Rendering of 3D oxygen polyhedra around lead for the same assumptions.	93
5.6	Structure of scandium oxide, revealing distorted and undistorted (dashed) oxygen octahedra	96
5.7	^{45}Sc MAS experiment and simulation (broken line) at 7T, 20kHz spinning speed, for: (a) scandium acetate, (b) scandium oxalate, (c)scandium carbonate and (d) scandium nitrate. (a) and (b) have single sites, whilst (c) and (d) have two and three respectively, indicated by letters. A spinning side band (*) is visible in (b).	98
5.8	Experimental spectra (top) for scandium oxide, ^{45}Sc 3QMAS at 17.6T and 15 kHz spinning speed, with simulation (bottom).	99
5.9	Experimental spectra (top) for scandium sulfate, ^{45}Sc 3QMAS at 17.6T and 15 kHz spinning speed, with simulation (bottom)	100
5.10	Experimental and simulated (broken line) direct dimensions for 3QMAS experiments; scandium sulfate (top) and scandium oxide (bottom)	101
5.11	^{45}Sc MAS experiments for $(1-x)\text{PSW}-x\text{PT}$, conducted at 19.6T and 10 kHz spinning speed; (a) $x=0$, (b) $x=0.15$, (c) $x=0.25$ and (d) $x=0.35$. In (a), (b) and (c) narrow peak one arises from scandium on mixed β' sites, surrounded by six nBn scandium. In all, broad peaks correspond to scandium on pure β'' sites surrounded by mixed nBn shells, comprised of varying quantities of scandium, titanium and tungsten atoms.	104

5.12	^{45}Sc MAS experiments for $(1-x)\text{PSW}-x\text{PZ}$, conducted at 19.6T and 10 kHz spinning speed; (a) $x=0$, (b) $x=0.15$ and (c) $x=0.35$. In (a), (b) and (c) narrow peak one arises from scandium on mixed β' sites, surrounded by six nBn scandium. In all, broad peaks correspond to scandium on pure β'' sites surrounded by mixed nBn shells, comprised of varying quantities of scandium, zirconium and tungsten atoms.	105
5.13	Broad MAS peaks correspond to scandium on β'' ordered sites, surrounded by mixed charges in 1:1 RS model. The B cation on β' sites (labeled M) may be Ti/W/Zr/Sc.	107
5.14	Nearest B-site Neighbor (nBn) configuration probabilities for scandium in $(1-x)\text{PSW}-x\text{PT}/\text{PZ}$; M may be either titanium or zirconium. The number of tungsten cations is constant along diagonals, scandium along rows and M along columns.	107
5.15	$(1-x)\text{PSW}-x\text{PT}$ 3QMAS, 19.6T. Clockwise from top left: $x=0$, $x=0.15$, $x=0.35$, $x=0.25$	109
5.16	$(1-x)\text{PSW}-x\text{PZ}$ 3QMAS, 19.6T. (Clockwise from top left): $x=0$, $x=0.15$, $x=0.35$	111
5.17	Simulation of $(1-x)\text{PSW}-x\text{PZ}$ 3QMAS spectra, 19.6T. Grid size was 256×128 points, based on 1k samples for each distribution. Clockwise from top left, $x=0$, $x=0.15$ (PT), $x=0.25$ (PT), $x=0.15$ (PZ)	112
5.18	Experimental spectra with simulations (dashed) of $(1-x)\text{PSW}-x\text{PZ}$ 3QMAS spectra, 19.6T, F2 projections. Grid size was 256×128 points, based on 1k samples for each distribution. Clockwise from top left, $x=0$, $x=0.15$ (PT), $x=0.25$ (PT), $x=0.15$ (PZ)	113
5.19	Space group Imma, with tilt system $a^0b^-b^-$ and 1:1 order along [1,1,1]. Red and green octahedra illustrate the different species on the B-site.	115
5.20	Calculated C_Q distribution for 0.85PSW-0.15PT (left), and 0.85PSW-0.15PZ (right)	117

5.21	(Top) Plot of interaction energy versus x and y coordinates for lead in a distorted PSW perovskite lattice, using rotation system $a^0b^-b^-$ and ratio of 1:1.2 for $\beta'' : \beta'$ site B-O bond lengths in the RS model. For a variety of Pb sites surveyed, a displacement along $[-1,0,0]$ appears preferable and the minima for the energy is deeper than a more ferroelectric counterpart such as PST, without random sites. (Bottom) Rendering of the distorted 3D oxygen polyhedra around lead for the same assumptions.	118
5.22	Model for acquisition and separation of all four quadrants, $S_{xx} = (c, c)$, $S_{xy} = (c, s)$, $S_{yx} = (s, c)$ and $S_{yy} = (ss)$. Arrows correspond to fid's; there are t_1/n increments along columns of length n and t_2/m increments along rows of length m . Fourier transform of all matrix 'elements' produces F3 and combination of columns or rows in the States method reproduces phase signals for t_2 and t_1 respectively.	120
5.23	(a) Three dimensional multiple quantum MAS experiment, based on the scheme suggested by Donghua Zhou. Pulse block 1 represents a double quantum filter and pulse block 2 a triple quantum filter. Pulse five and delay τ_z comprise the z-filter, with a selective 90 degree pulse for detection. (b) Coherence transfer pathway for 3D-MQMAS	121
5.24	Three dimensional MQMAS of Rubidium Nitrate, displaying the three chemically distinct sites. Single, double and triple quantum frequencies are F3, F1 and F2 respectively and isosurface is drawn at 40% of maximum value.	122
5.25	High resolution contour plot of double (F1) and triple (F2) quantum frequency dimensions, devoid of anisotropy. Ten contours are drawn in linear increments from 20 to 95 %.	122

ABSTRACT

This work is devoted to the study of local order in the ferroelectric $\text{Pb}(\text{Sc}_{1/2}\text{Ta}_{1/2})\text{O}_3$ (PST) and relaxor ferroelectric solid solutions $(1-x)\text{Pb}(\text{Sc}_{2/3}\text{W}_{1/3})\text{O}_3 - (x)\text{PbTiO}_3$ (PSW-PT), $(1-x)\text{Pb}(\text{Sc}_{2/3}\text{W}_{1/3})\text{O}_3 - (x)\text{PbZrO}_3$ (PSW-PZ). Novel Magic Angle Spinning (MAS) Solid State Nuclear Magnetic Resonance (SS-NMR) experiments, including Multiple Quantum MAS (MQMAS) and Double Quantum Filtered Satellite Transition (DQF-STMAS), have been performed on these materials. The underlying NMR parameter distributions, which may be attributed to local disorder, complicate interpretation. A Gamma function model is proposed for the distribution of quadrupole coupling constants, based on the Poissonian nature of atomic displacements. Moments for distributions may be subsequently extracted through agreement between experimental spectra and simulations implemented in novel programs. A survey of model compounds was also undertaken in an effort to determine correlations between structural features such as bond lengths, angles and NMR parameters. A direct correlation could not be established to provide quantitative information for the Relaxors. However the simple crystal compound Scandium Oxide provides a reasonable analogue and assists in spectral interpretation. Point charge calculations of NMR parameters provides further insight into the relationships between local order and NMR spectra. Support is given to the Random Site (RS) model for atomic ordering in Relaxor Ferroelectrics. The random site (β') unit cells in these materials which contains a mixture of atoms is generally 1.1-1.2 times as large as the ordered layer (β'') cells, composed of a single species. The implications for lead displacement are rather significant; a study of the point charge interaction energy between lead atoms and two nearest neighbor shells demonstrates a clear preference for lead displacement along $[-1,0,0]$. In June 2004 Donghua Zhou proposed an experimental scheme to expedite the interpretation of experimental spectra of disordered materials, by resolving interactions along independent frequency axes. An experimental realization with analysis is given here.

NUCLEAR MAGNETIC RESONANCE STUDIES OF RELAXOR
FERROELECTRICS

Chapter 1

Introduction

Relaxor ferroelectric materials continue to be fundamentally interesting and technologically significant materials. Based on their large dielectric constants and electromechanical response they are invaluable as transducers, actuators and capacitors. Their broad para- to ferroelectric phase transition stands in distinction to their normal ferroelectric counterparts. The microscopic origins of this phase transition behavior, as well as the accompanying dielectric anomaly remain features of intense study and discussion.

Complementing the wide array of long range structure determination methods is Nuclear Magnetic Resonance (NMR), which serves as a short range or local structural probe, sensitive to length scales less than 100 Angstroms. NMR exploits the magnetic property of any nucleus with a non-zero quantum mechanical spin. When a sample is placed in a magnetic field, the degeneracy of its spin energy levels is lifted; the exact values are perturbed by the presence of spin-spin interactions which contain useful information. Radio frequency energy is used to excite the system and the subsequent frequency response of the system is digitized

and collected. Recently, ab-initio methods have permitted a direct comparison to be drawn between atomic information and NMR parameters extracted from experimental data [54, 31, 45].

Previously, NMR experiments were used to characterize chemical disorder [35, 17] in the (1-x)PMN-xPSN series solutions of relaxor ferroelectrics, produced at the University of Pennsylvania [52]. Results supported the Random Site Model [23] for most concentrations. In addition it was observed that the isotropic chemical shift of well resolved peaks depended linearly on the number of magnesium atoms within nearest B-site neighbor configurations. It was also observed that niobium devoid configurations have small Electric Field Gradients (EFG) (P_Q 6-12 MHz), whilst niobium containing configurations have a large EFG (P_Q 19-41 MHz). ^{207}Pb 2D-PASS experiments were used to characterize the Pb-O bond environment [18]. While a particular model for lead displacement could be discerned, a unique direction could not be unambiguously determined.

The present materials under consideration were synthesized and characterized by dielectric, X-ray and Neutron diffraction at the University of Pennsylvania [64]. The tungstate relaxor ferroelectric perovskite $\text{Pb}(\text{Sc}_{2/3}\text{W}_{1/3})\text{O}_3$ PSW has 1:1 random site structure along the [1,1,1] direction; layers of pure Sc are interleaved with mixed layers containing 2:1 ratio of Sc/W. It was determined [64] that introduction of Zr (PSW-PZ) destabilizes the RS order, whilst Ti (PSW-PT) maintains order up until $x \approx 0.25$. Beyond the Morphotropic Phase Boundary (MPB) at $x = 0.25$ all materials display marked relaxor behavior and in the vein of previous work are amenable to study via Solid State Nuclear Magnetic Resonance.

Chapter 2

Nuclear Magnetic Resonance

2.1 Spin and Zeeman Levels

A large number of atomic nuclei in their ground state have a non-zero spin angular momentum $I\hbar$ and corresponding magnetic dipole moment $\mu = \gamma\hbar I$. The constant of proportionality γ is called the magneto-gyric ratio and is typically many orders of magnitude smaller than analogous electronic moments. Quite frequently discussion of the different types of magnetism (ferro-, dia- and para-) is restricted to contributions from electron orbital motion alone. Nuclear magnetism may be classified analogously, although the observed nuclear magnetic behavior is paramagnetic, that is a macroscopic nuclear magnetization is present only when a sample containing non-zero nuclear spin is placed in a field H_0 . A nucleus in this condition has an energy $E = -\mu \cdot H_0 = -\gamma\hbar I H_0$. The occupation of the energy levels is determined by the Boltzmann energy distribution. Assuming that the spins are non-interacting and expressed with the usual basis $|j, m\rangle$, statistical mechanics gives for the macroscopic magnetization [7]:

$$M = N\gamma\hbar \frac{\sum_{m=-I}^I m \exp(-\gamma\hbar m H_0/kT)}{\sum_{m=-I}^I \exp(-\gamma\hbar m H_0/kT)}. \quad (2.1)$$

The ‘high temperature’ approximation holds very well for almost all practical situations, for which $\gamma\hbar H_0/kT \ll 1$ and:

$$M = \frac{N\gamma^2\hbar^2 I(I+1)}{3kT} H_0 = \chi_0 H_0 \quad (2.2)$$

where χ_0 is the nuclear magnetic susceptibility, around seven orders of magnitude smaller than electronic paramagnetic susceptibility. Resonance methods are exclusively required to observe the nuclear counterpart. The essential idea is to drive the resonant absorption of these nuclear magnetic levels with radio frequency energy and observe the frequency response of the system.

We consider now the motion of an isolated spin with angular momentum $\mathbf{I}\hbar$ and magnetic moment $\boldsymbol{\mu} = \gamma\hbar\mathbf{I}$. This moment (classically) experiences a torque $\boldsymbol{\tau} = \boldsymbol{\mu} \times \mathbf{H}$ equivalent to its change in angular momentum $\hbar(d\mathbf{I}/dt)$, ie.,

$$\frac{d\boldsymbol{\mu}}{dt} = \gamma\boldsymbol{\mu} \times \mathbf{H}, \quad (2.3)$$

The method of solution may be simplified considerably by transforming to a coordinate frame S' rotating at angular velocity $\boldsymbol{\omega}$ with respect to the stationary laboratory frame¹ S . Following the transformation law for a vector in a rotating frame,

$$\left(\frac{d\mathbf{A}}{dt}\right)_S = \left(\frac{\partial\mathbf{A}}{\partial t}\right)_{S'} + \boldsymbol{\omega} \times \mathbf{A} \quad (2.4)$$

Hence the motion for the magnetic moment in the rotating frame is given by

¹Group Theory describes angular momentum as a generator for rotation, see Appendix A

$$\frac{\partial \mu}{\partial t} = \gamma \mu \times \left(\mathbf{H} + \frac{\omega}{\gamma} \right). \quad (2.5)$$

This is the same form as earlier, with *effective field* $\mathbf{H}_e = \mathbf{H} + (\omega/\gamma)$. The simplification is made obvious by choosing a frame for which $\omega = -\gamma \mathbf{H}_0$ where we assume for now that the field is constant. In this frame the magnetic moment is a fixed vector, rotating in the lab frame at the *Larmor Frequency* $\omega_0 = -\gamma H_0$.

Suppose now that in addition to the applied static field $\mathbf{H}_0 = H_0 \mathbf{k}$ there exists a field \mathbf{H}_1 perpendicular to the static field, rotating at the angular velocity ω . Hence for the effective field we may write:

$$\mathbf{H}_e = \left(H_0 + \frac{\omega}{\gamma} \right) \mathbf{k} + H_1 \mathbf{i} \quad (2.6)$$

Define $\omega_1 = -\gamma H_1$; then

$$H_e = \left[\left(H_0 + \frac{\omega}{\gamma} \right)^2 + H_1^2 \right]^{1/2} = -\frac{a}{\gamma} \quad (2.7)$$

where

$$a = -[(\omega_0 - \omega)^2 + \omega_1^2]^{1/2} \frac{\gamma}{|\gamma|} \quad (2.8)$$

The angle between \mathbf{H}_e and the applied field \mathbf{H}_0 ;

$$\tan \theta = \frac{H_1}{H_0 + (\omega/\gamma)} = \frac{\omega_1}{\omega_0 - \omega} \quad (2.9)$$

Hence, in the rotating frame the motion of the magnetic moment is also a Larmor precession around the effective field. In general the time dependent radio frequency field H_1 is much smaller than static field H_0 so the angle theta or ‘tip angle’ will be insignificant unless $|\omega - \omega_0| \approx |\omega_1|$, which is the resonance condi-

tion. This elegant description while classical is still of the form of the quantum mechanical solution, made explicit in the following [79].

In the Heisenberg representation, equations of motion for angular momentum operator are;

$$\frac{\hbar}{i} \frac{d\mathbf{I}}{dt} = [\mathcal{H}, \mathbf{I}] = [-\gamma\hbar\mathbf{H} \cdot \mathbf{I}, \mathbf{I}], \quad (2.10)$$

In this case, we have considered only the Zeeman Hamiltonian, without regard to possible interactions between the spins. The z -component has a familiar form:

$$\frac{\hbar}{i} \frac{dI_z}{dt} = \frac{\gamma\hbar}{i} [\mathbf{I} \times \mathbf{H}]_z \quad (2.11)$$

It is obvious at this stage that the expectation value of the operator obeys the classical expression. We proceed to the expression for the wave function of a spin subject to a steady field in the z direction, perturbed by an r.f. field of the form:

$$\mathbf{H}_1 = H_1(I_x \cos \omega t + I_y \sin \omega t) \quad (2.12)$$

The wave function is a solution to Schrodinger's equation:

$$i \frac{\partial \psi}{\partial t} = \frac{\mathcal{H}}{\hbar} \psi = -\gamma \{ H_0 I_z + H_1 (I_x \cos \omega t + I_y \sin \omega t) \} \psi \quad (2.13)$$

$$= \{ \omega_0 I_z + \frac{1}{2} \omega_1 (I_+ e^{-i\omega t} + I_- e^{i\omega t}) \} \psi \quad (2.14)$$

By substituting $\psi = U\psi' = e^{-i\omega I_z t} \psi'$ we effectively transform to a rotating co-ordinate frame; Schrodinger's equation becomes:

$$i\frac{\partial\psi'}{\partial t} = \left\{ U^{-1}\frac{\mathcal{H}}{\hbar}U - iU^{-1}\frac{\partial U}{\partial t} \right\} \psi' \quad (2.15)$$

equating;

$$\psi' = \exp[-i\{(\omega_0 - \omega)I_z + \omega_1 I_x\}t]\psi'(0) \quad (2.16)$$

But $\psi'(0) = \psi(0)$, so

$$\psi = \exp(-i\omega I_z t) \exp\{-ia(\mathbf{n} \cdot \mathbf{I})t\}\psi(0) \quad (2.17)$$

where a is given earlier, \mathbf{n} is a unit vector. The probability $P_{mm'}$ to find the spin in state m' given that it was in state m earlier is:

$$P_{mm'} = |\langle m' | \exp\{-ia(\mathbf{n} \cdot \mathbf{I})t\} | m \rangle|^2 \quad (2.18)$$

$$= (\cos \frac{1}{2}\alpha)^{4I} (I+m)!(I+m')!(I-m)!(I-m')! \times \left[\sum_{\lambda=0}^{2I} (-1)^\lambda \frac{(\tan \frac{1}{2}\alpha)^{2\lambda-m+m'}}{\lambda!(\lambda-m+m')!(I+m-\lambda)!(I-m'-\lambda)!} \right]^2 \quad (2.19)$$

where $\sin^2 \frac{1}{2}\alpha = \sin^2 \theta \sin^2(\frac{1}{2}at)$. A spin subjected to radio frequency energy has therefore a finite probability to change states. This is a feature of the interaction between spins and the external influence of a field. In experiments, this interaction serves as the perturbing presence with which to test the influence of internal interactions, and thus glean information from the atomic system.

2.2 Internal Interactions

2.2.1 Quadrupole Coupling

Approximately seventy isotopes possess a nuclear spin greater than one-half. As such, they have a quadrupole moment and thus may couple with the surrounding electric field gradient. In developing an appreciation for this interaction, one begins by describing the interaction between nuclear and electronic charge distributions as [7]:

$$W_E = \int \int \frac{\rho_e(r_e)\rho_n(r_n)dr_edr_n}{|\mathbf{r}_n - \mathbf{r}_e|}. \quad (2.20)$$

In the usual manner, we may expand in terms of the spherical harmonics as

$$\frac{1}{|\mathbf{r}_n - \mathbf{r}_e|} = 4\pi \sum_{l=0}^{\infty} \sum_{m=-l}^l \frac{1}{2l+1} \frac{r_{<}^l}{r_{>}^{l+1}} Y_l^{m*}(\theta_n, \phi_n) Y_l^m(\theta_e, \phi_e), \quad (2.21)$$

where $r_{<}$ and $r_{>}$ refer to the lesser and greater of r_e, r_n respectively. Assuming $r_e > r_n$ for logical reasons,

$$W_E = \sum_{l,m} A_l^m B_l^{m*}, \quad (2.22)$$

$$A_l^m = \sqrt{\left(\frac{4\pi}{2l+1}\right)} \int \rho_n(r_n) r_n^l Y_l^m(\theta_n, \phi_n) dr_n, \quad (2.23)$$

$$B_l^m = \sqrt{\left(\frac{4\pi}{2l+1}\right)} \int \rho_e(r_e) r_e^{-l-1} Y_l^m(\theta_e, \phi_e) dr_e. \quad (2.24)$$

These quantities² may be considered the classical expectation values of quantum operators,

$$\mathcal{A}_l^m = \sqrt{\left(\frac{4\pi}{2l+1}\right)} \sum_i e_i R_i^l Y_l^m(\Theta_i, \Phi_i), \quad (2.25)$$

²Using identities for spherical harmonics, one may show that $\mathcal{B}_l^{m*} = (-1)^m \mathcal{B}_l^{-m}$ which gives an expression for W_E which agrees with the convention of Rose

with R_i, Θ_i, Φ_i the polar coordinates of the A nucleons. Likewise B_l^m is the expectation value of the electron operator

$$\mathcal{B}_l^m = -e \sqrt{\left(\frac{4\pi}{2l+1}\right)} \sum_{i=1}^N r_i^{-l-1} Y_l^m(\theta_i, \phi_i) \quad (2.26)$$

with r_i, θ_i, ϕ_i are the coordinates of the electrons. Therefore the quantum mechanical Hamiltonian for the interaction is given by:

$$\mathcal{H}_E = \sum_{l,m} \mathcal{A}_l^m \mathcal{B}_l^{m*}. \quad (2.27)$$

Since these operators are built upon spherical harmonics of order l , they transform in a like manner. \mathcal{A}_l^m is the multipole moment of order l of the nucleus, with $2l+1$ components. There are at least two limitations on the form of the matrix elements for this operator, including the disappearance of terms with l an odd value, corresponding to the nuclear states having well defined parities. Also, l is bounded according to the relation given for the transformation of operators from one basis to another, i.e.,

$$|J - J'| \leq l \leq |J + J'|.$$

So a nucleus of spin $I \geq 1$ will have quadrupole moments, $I \geq 2$ moments of order 4 etc. The magnitude of the various moments drop off rapidly and is common to restrict interest to the quadrupole interaction. The components of \mathcal{A}_2^m in Cartesian co-ordinates:

$$\mathcal{A}_2^{\pm 2} = \frac{\sqrt{6}}{4} \sum_i e_i (x_i \pm iy_i)^2, \quad (2.28)$$

$$\mathcal{A}_2^{\pm 1} = \frac{\sqrt{6}}{2} \sum_i e_i z_i (x_i \pm iy_i), \quad (2.29)$$

$$\mathcal{A}_2^{\pm 1} = \frac{1}{2} \sum_i e_i (3z_i^2 - r_i^2). \quad (2.30)$$

Expressed in a basis for a nuclear state with spin I ,

$$Q^{\pm 2} = \alpha(\sqrt{6}/4)(I_{\pm})^2, \quad (2.31)$$

$$Q^{\pm 1} = \alpha(\sqrt{6}/4)\{I_z I_{\pm} + I_{\pm} I_z\}, \quad (2.32)$$

$$Q^0 = \frac{1}{2}\alpha(3I_z^2 - I(I+1)). \quad (2.33)$$

Defining the quadrupole constant as

$$eQ = \langle I, m = I | \sum_{i=1}^A e_i (3z_i^2 - r_i^2) | I, m = I \rangle, \quad (2.34)$$

we may write

$$eQ = 2\langle I, m = I | \mathcal{A}_2^0 | I, m = I \rangle = 2\langle I, m = I | Q^0 | I, m = I \rangle \quad (2.35)$$

$$= \alpha \langle I, m = I | 3I_z^2 - I(I+1) | I, m = I \rangle \quad (2.36)$$

hence,

$$Q^{\pm 2} = \frac{eQ}{I(2I-1)} \frac{\sqrt{6}}{4} I_{\pm}^2, \quad (2.37)$$

$$Q^{\pm 1} = \frac{eQ}{I(2I-1)} \frac{\sqrt{6}}{4} \{I_z I_{\pm} + I_{\pm} I_z\}, \quad (2.38)$$

$$Q^0 = \frac{eQ}{I(2I-1)} \frac{1}{2} \{3I_z^2 - I(I+1)\}. \quad (2.39)$$

Similarly for the electronic tensor, where

$$\mathcal{B}_2^0 = \frac{1}{2} \sum_{i=1}^N \frac{e_i(3z_i^2 - r_i^2)}{r_i^5} = \frac{1}{2} \left(\frac{\partial^2 \mathcal{V}}{\partial z^2} \right)_{r=0} = \frac{1}{2} \mathcal{V}_{zz} \quad (2.40)$$

$\mathcal{V}(x, y, z)$ is the electrostatic potential produced by the electrons at the point (x, y, z) . Further,

$$\mathcal{B}_2^{\pm 2} = \frac{1}{2\sqrt{6}} (\mathcal{V}_{xx} - \mathcal{V}_{yy} \pm 2i\mathcal{V}_{xy}), \quad (2.41)$$

$$\mathcal{B}_2^{\pm 1} = \frac{1}{\sqrt{6}} (\mathcal{V}_{xz} \pm i\mathcal{V}_{yz}). \quad (2.42)$$

Re-writing the Hamiltonian for the quadrupole coupling;

$$\mathcal{H}_2 = \sum_{m=-2}^2 \mathcal{A}_2^m \mathcal{B}_2^{-m} = \sum_{m=-2}^2 Q^m \mathcal{B}_2^{-m}, \quad (2.43)$$

Further inspection allows us to write:

$$\mathcal{H}_2 = \sum_{j,k} \left(\frac{\partial^2 \mathcal{V}}{\partial x_j \partial x_k} \right)_{r=0} Q_{jk}, \quad (2.44)$$

where

$$Q_{jk} = \frac{eQ}{6I(2I-1)} \left\{ \frac{3}{2} (I_j I_k + I_k I_j) - \delta_{jk} I(I+1) \right\} \quad (2.45)$$

is a traceless Cartesian tensor. The operator $\left(\frac{\partial^2 \mathcal{V}}{\partial x_j \partial x_k} \right)_{r=0}$ is the *electric field gradient* (EFG) at the nuclear position. In bulk matter we may treat the electric field tensor operators as classical, owing to an absence of orbital degeneracy in most materials. Introducing:

$$V^0 = \frac{1}{2} V_{zz} = \frac{1}{2} \langle \mathcal{V}_{zz} \rangle$$

$$V^{\pm 1} = \frac{1}{\sqrt{6}} (V_{zx} \pm iV_{zy})$$

$$V^{\pm 2} = \frac{1}{2\sqrt{6}}(V_{xx} - V_{yy} \pm 2iV_{xy}) \quad (2.46)$$

hence the quadrupole interaction in bulk matter may be written

$$\mathcal{H} = \sum_m Q^m V^{-m} \quad (2.47)$$

If the co-ordinates chosen correspond to the so-called Principal Axis System (PAS) [61] where $V_{XZ} = V_{YZ} = V_{XY} = 0$ and $|V_{ZZ}| \geq |V_{XX}| \geq |V_{YY}|$, and if one defines $eq = V_{ZZ}$, $\eta = (V_{XX} - V_{YY})/V_{ZZ}$ the quadrupole Hamiltonian becomes:

$$\mathcal{H} = \frac{e^2 q Q}{4I(2I - 1)} \left\{ 3I_z^2 - I(I + 1) + \frac{1}{2}\eta(I_+^2 + I_-^2) \right\} \quad (2.48)$$

The quadrupole coupling constant eq and asymmetry parameter η are of great import since their value is directly related to the immediate chemical environment. Quadrupole moments Q have been measured for many nuclei of interest, and the most recent work gives -0.231 barns for scandium [40]. In ionic crystals, coupling between nuclei and immediate electronic environments is negligible owing to almost spherical symmetry. The electric field gradient therefore arises from charges removed from the ion; these same charges produce a distortion of the electronic environment of the ion and hence the total gradient experienced by the nuclei is given by:

$$(1 + \gamma)V_{jk}^e \quad (2.49)$$

where γ is the anti-shielding factor [80, 81]. When the electric field gradient tensor is expressed throughout the remainder of this work, the anti-shielding factor will be assumed to be included.

2.2.2 Chemical Shift Interaction

The magnetic interaction which exists between the nuclear dipole moment and moment(s) of the electronic shell gives rise to the chemical shift [73, 74]. Using the relations for the vector potential,

$$\nabla \cdot \mathbf{A} = 0; \nabla \times \mathbf{A} = \mathbf{H}, \quad (2.50)$$

the vector potential of the dipole [7],

$$\mathbf{A} = \frac{\boldsymbol{\mu} \times \mathbf{r}}{r^3} = \nabla \times \left(\frac{\boldsymbol{\mu}}{r} \right), \quad (2.51)$$

we may write for the Hamiltonian for the electron in the presence of the dipolar field:

$$\mathcal{H} = \frac{1}{2m} \left(\mathbf{p} + \frac{e}{c} \mathbf{A} \right)^2 + 2\beta \mathbf{s} \cdot (\nabla \times \mathbf{A}) \quad (2.52)$$

with β the Bohr magneton and \mathbf{s} the electron spin. To first order, the spin dependent portion is:

$$\begin{aligned} \mathcal{H}_1^s &= 2\beta \mathbf{s} \cdot \left[\nabla \times \left(\nabla \times \frac{\boldsymbol{\mu}}{r} \right) \right] \\ &= 2\beta [(\mathbf{s} \cdot \nabla)(\boldsymbol{\mu} \cdot \nabla) - (\mathbf{s} \cdot \boldsymbol{\mu}) \nabla^2] \frac{1}{r} \end{aligned} \quad (2.53)$$

This straightforward expression describes two important effects, namely the chemical shift and indirect spin-spin interactions. For chemical shift, the immediate electronic environment of a nuclei changes the local field experienced by the nuclei due to both:

1. Polarization of the electronic shells by the applied static field H_0 producing a field H_p (subscript p, paramagnetic) proportional to it, and

2. the Larmor precession of the electrons forming a current density and subsequently a magnetic field at the nucleus, H_d (subscript d, diamagnetic).

For spin-spin interactions, a given nuclei produces a distortion in its electronic shells, which in turn produces a field at a second nuclear site, indirectly coupling the nuclei. In all practical cases one deals with a very large number of both nuclear moments N and electrons n ; the Hamiltonian in the presence of the static field is:

$$\mathcal{H} - V = \frac{1}{2m} \sum_{k=1}^n \left(\mathbf{p}_k + \frac{e}{c} \mathbf{A}_k^0 + \frac{e}{c} \sum_{q=1}^N \mathbf{A}_k^q \right)^2 + 2\beta \sum_{k=1}^n \mathbf{s}_k \cdot \nabla \times \mathbf{A}_k^0 + 2\beta \sum_{k=1}^n \sum_{q=1}^N \mathbf{s}_k \cdot \nabla \times \mathbf{A}_k^q \quad (2.54)$$

where $\mathbf{A}_k^0 = \frac{1}{2}(\mathbf{H}_0 \times \mathbf{r}_k)$ is the vector potential of the external field at the k th electron, $\mathbf{A}_k^q = \frac{(\mu_q \times \mathbf{r}_{qk})}{r_{qk}^3}$ is the vector potential of the q th nuclear moment experienced by the k th electron and V is the electrostatic potential. The result should be independent of the choice of origin owing to gauge invariance. An perturbative expansion gives the following terms:

$$\mathcal{H} - V - T - D = (Z_L + Z_S) + (O_1 + S_1 + S_2) + (O_2 + O_3), \quad (2.55)$$

Terms T and D deal with the kinetic energy and are not relevant to the calculation.

$Z_S = 2\beta \mathbf{H}_0 \cdot \mathbf{S}$ is the electron spin Zeeman energy and

$$Z_L = \frac{e}{2mc} \sum_{k=1}^n (\mathbf{p}_k \cdot \mathbf{A}_k^0 + \mathbf{A}_k^0 \cdot \mathbf{p}_k) = \beta \mathbf{H}_0 \cdot \mathbf{L} \quad (2.56)$$

is the orbital Zeeman energy of the electrons. The other terms comprise the magnetic couplings between the n electrons and the N nuclei.

$$\begin{aligned}
O_1 &= 2\beta \sum_{k=1}^n \sum_{q=1}^N \frac{\mu_k \cdot (\mathbf{r}_{qk} \times \mathbf{p}_k)}{r_{qk}^3} \\
S_1 &= 2\beta \sum_{k=1}^n \sum_{q=1}^N \frac{1}{r_{qk}^3} \left\{ \frac{3(\mathbf{s}_k \cdot \mathbf{r}_{qk})(\mu_q \cdot \mathbf{r}_{qk})}{r_{qk}^2} - (\mathbf{s}_k \cdot \mu_q) \right\}, \\
S_2 &= \frac{16\pi}{3} \beta \sum_{k=1}^n \sum_{q=1}^N (\mathbf{s}_k \cdot \mu_q) \delta(\mathbf{r}_{qk}). \\
O_2 &= \frac{e^2}{2mc^2} \sum_{k=1}^n \sum_{q=1}^N (\mathbf{H}_0 \times \mathbf{r}_{qk}) \cdot (\mu_q \times \mathbf{r}_{qk}) / r_{qk}^3 \\
O_3 &= \frac{e^2}{2mc^2} \sum_{k,q,q'} \frac{(\mu \times \mathbf{r}_{qk}) \cdot (\mu_{q'} \times \mathbf{r}_{q'k})}{r_{qk}^3} \tag{2.57}
\end{aligned}$$

The terms $O_1 + S_1 + S_2$ are the sum of the couplings between the n electrons and the N nuclei; O_2 represents the coupling between the nuclear dipole moments and the magnetic field of the currents induced by the Larmor precession of the electrons in the static field.

The expectation value of the energy using the ground state functions for diamagnetic materials has non-zero values for only terms O_2 and O_3 . Taking as the origin the particular nucleus for which the shift is being calculated, one may write:

$$\langle O_2 \rangle = \frac{e^2}{2mc^2} \left\langle 0\rho \left| \sum_k \frac{(\mathbf{H}_0 \times \mathbf{r}_k) \cdot (\mu \times \mathbf{r}_k)}{r_k^3} \right| 0\rho \right\rangle. \tag{2.58}$$

The ground states $|0\rangle$ contain various degrees of freedom, including rotational, vibrational etc. This expectation value may be decomposed into three parts³,

$$\boldsymbol{\mu} \cdot \boldsymbol{\Sigma}_d \cdot \mathbf{H}_0 \quad (2.59)$$

Further, the tensor $\boldsymbol{\Sigma}$ may be decomposed into a traceless component:

$$\Sigma_d'^{pq} = -\frac{e^2}{2mc^2} \left\langle 0\rho \left| \sum_k \frac{x_k^p x_k^q}{r_k^3} - \frac{1}{3} \frac{\delta^{pq}}{r_k} \right| 0\rho \right\rangle \quad (2.60)$$

and a scalar component:

$$\Sigma_d''^{pq} = \sigma_d \delta_{pq}; \sigma_d = \frac{e^2}{3mc^2} \left\langle 0\rho \left| \sum_k \frac{1}{r_k} \right| 0\rho \right\rangle. \quad (2.61)$$

As it turns out, σ_d is independent of the rotational state of the atom/molecule, hence

$$\sigma_d = \frac{e^2}{3mc^2} \left\langle 0 \left| \sum_k \frac{1}{r_k} \right| 0 \right\rangle \quad (2.62)$$

The average of the traceless component over the rotational states is negligible, corresponding to the case in liquids where rapid tumbling performs the operation. However in static samples, the term corresponds to the chemical shift anisotropy. There are further terms in the expression for energy which when considered together are bilinear in $\boldsymbol{\mu}$ and \mathbf{H}_0 , therefore contributing to the chemical shift. A combination of O_1 and Z_L gives, using second order perturbation theory:

$$\Delta = 2\beta^2 \sum_{n,k} \frac{\langle 0\rho | \mathbf{L} \cdot \mathbf{H}_0 | n \rangle \langle n | \boldsymbol{\mu} \cdot \mathbf{l}_k / r_k^3 | 0\rho \rangle}{E_0 - E_n} + c.c$$

³Subscript d stands for diamagnetic

$$= 2\beta^2 \sum_k \left\langle 0\rho \left| (\mathbf{L} \cdot \mathbf{H}_0) C \left(\frac{\boldsymbol{\mu} \cdot \mathbf{l}_k}{r_k^3} \right) \right| 0\rho \right\rangle + c.c. \quad (2.63)$$

where

$$C = \sum \frac{|n\rangle\langle n|}{E_0 - E_n}.$$

As before, this equation may also be written in the form⁴:

$$\boldsymbol{\mu} \cdot \boldsymbol{\Sigma}_p \cdot \mathbf{H}_0 \quad (2.64)$$

Again, $\boldsymbol{\Sigma}_p$ may be decomposed into a traceless component:

$$\boldsymbol{\Sigma}_p'^{mn} = 2\beta^2 \sum_k \left\langle 0\rho \left| L^m C \frac{l_k^n}{r_k^3} - \frac{1}{3} \frac{\mathbf{L}C \cdot \mathbf{l}_k}{r_k^3} \right| 0\rho \right\rangle + c.c. \quad (2.65)$$

and a scalar component:

$$\boldsymbol{\Sigma}_p''^{mn} = \sigma_p \delta^{mn}; \sigma_p = \frac{2\beta^2}{3} \sum_k \left\langle 0 \left| \frac{\mathbf{L}C \cdot \mathbf{l}_k + \mathbf{l}_k C \cdot \mathbf{L}}{r_k^3} \right| 0 \right\rangle \quad (2.66)$$

Rotational degrees of freedom in the basis functions may be neglected. The paramagnetic contribution to the chemical shift anisotropy is non-zero as before in the case of solids. Further, the paramagnetic shielding constant σ_p is significantly more difficult to calculate than its diamagnetic counterpart, involving excited states of the molecule/atom. The contribution of the paramagnetic term can be significant where there are excited states close to the molecular ground states.

⁴Subscript p stands for paramagnetic

2.3 The Density Operator

We return to the single spin system whose quantum state is described by ψ ;

$$|\psi\rangle = \sum_n c_n |n\rangle.$$

For a particular spin I there exist $2I + 1$ states $|I, -m\rangle, |I, -m + 1\rangle, \dots, |I, m - 1\rangle, |I, m\rangle$ which span a $2I + 1$ dimensional Hilbert space. They provide a convenient basis set since the Zeeman energy levels for a nuclei embedded in a magnetic field directly correspond to these eigenstates. The label m is the quantum number of the spin projection in the z -direction.

Physical observables correspond to the expectation value of some quantum mechanical operator, e.g., the x -component of the magnetization;

$$\langle M_x \rangle = \langle \psi | M_x | \psi \rangle = \sum_{n,m} c_m^* c_n \langle m | M_x | n \rangle \quad (2.67)$$

The sum over two quantum numbers constitutes a matrix equation and accordingly the terms $c_m^* c_n$ represent elements of the *quantum density operator*, defined as

$$\rho = |\psi\rangle\langle\psi| = \sum_{n,m} c_m^* c_n |n\rangle\langle m| \quad (2.68)$$

More generally we are concerned with a large number of spins, an ensemble of say N spins. We distinguish between *pure* and *mixed states*. A pure state is distinguished by having all spins in the same state $|\psi(t)\rangle$ and the density operator is defined as;

$$\begin{aligned} \rho(t) &= |\psi(t)\rangle\langle\psi(t)| = \sum_{i,j} \rho_{ij}(t) |i\rangle\langle j| \\ \rho_{ij}(t) &= c_i(t)c_j^*(t) = \langle i | \rho(t) | j \rangle. \end{aligned} \quad (2.69)$$

A mixed state contains various $|\psi_k(t)\rangle$ with weights p_k , $\sum_k p_k = 1$. The density operator is an average over all possible states;

$$\rho(t) = \sum_k^N p_k |\psi_k(t)\rangle \langle \psi_k(t)| = \sum_{i,j} \rho_{ij}(t) |i\rangle \langle j|,$$

$$\rho_{ij}(t) = \sum_k^N p_k c_{i(k)}(t) c_{j(k)}^*(t) = \langle i | \rho(t) | j \rangle. \quad (2.70)$$

To illustrate these ideas, consider an isolated spin 1/2 system, with basis functions:

$$|\alpha\rangle = |1/2, 1/2\rangle$$

$$|\beta\rangle = |1/2, -1/2\rangle$$

The system state is therefore:

$$|\psi\rangle = c_\alpha |\alpha\rangle + c_\beta |\beta\rangle$$

and hence the density operator:

$$\rho = \begin{pmatrix} \overline{c_\alpha c_\alpha^*} & \overline{c_\alpha c_\beta^*} \\ \overline{c_\beta c_\alpha^*} & \overline{c_\beta c_\beta^*} \end{pmatrix}, \quad (2.71)$$

where the bar denotes the average over the ensemble. A difference between the populations or diagonal density matrix elements, corresponds to a net longitudinal magnetization. The presence of coherences (off diagonal matrix elements) indicates transverse spin magnetization, a net spin perpendicular to the magnetic field. The coherences are complex and have both magnitude and phase; the phase of the (-1) coherence is equal to the angle of the transverse magnetization with the x -axis.

Coherences correspond to states which are in a *coherent* superposition of basis states $|i\rangle$ and $|j\rangle$; for this condition to persist throughout the ensemble, the phase differences between different members must be constant. The order of coherence is defined by the difference between the z -angular momentum numbers for the basis states, $\Delta m_{ij} = m_i - m_j$. There is a strong distinction in more complex systems between a *single* ($\Delta m_{ij} = \pm 1$) and *multiple quantum coherence* ($\Delta m_{ij} \neq \pm 1$). Due to the quantum mechanical selection rule for electromagnetic radiation, the single quantum coherence elements represent dipole transitions, which may be observed directly in experiment. Multiple quantum coherences involve higher order multipole transitions and can only be observed indirectly by magnetic resonance, without additional methods of excitation such as acoustic resonance. [7].

2.3.1 Time Evolution of the density operator

Quantum mechanics gives an expression for the density operator:

$$i\frac{\partial\rho}{\partial t} = [\mathcal{H}, \rho] \quad (2.72)$$

In most realistic cases, the solution of the equation of motion is quite difficult. However for equilibrium, statistical mechanics gives for the density operator:

$$\rho_{eq} = \frac{\exp(-\hbar\hat{\mathcal{H}}_0/kT)}{\sum_k \langle k | \exp(-\hbar\mathcal{H}_0/kT) | k \rangle} \quad (2.73)$$

where $\hat{\mathcal{H}}$ is the time independent portion of the Hamiltonian which can be used to derive the classical expression(s) for magnetization derived earlier.

In general spins are not isolated and interact with their environment to take up or expel energy, change state and move toward equilibrium. In NMR one usually

deals with a reduced spin density operator σ , where all other degrees of freedom are relegated to a vestige ρ_R [70]. The total density operator is the product of both, but for the determination of spin properties we consider σ alone; the remaining degrees of freedom comprise the ‘lattice’. It is the interactions with the lattice that allow the spin system to return to equilibrium. This process in NMR is called ‘spin-lattice’ relaxation and occurs with characteristic time T_1 . Interactions between spins give rise to ‘spin-spin’ relaxation, with characteristic time T_2 . This effect in solid state NMR is often attributed to the dipolar broadening, a coupling between the magnetic moments of individual nuclei. Further broadening is also introduced through the effects of anisotropy.

If we ignore the effects of the lattice which for small time scales is acceptable, we may write for the evolution of the density operator:

$$i\frac{d}{dt}(\sigma - \sigma_{eq}) = [\mathcal{H}, (\sigma - \sigma_{eq})] \quad (2.74)$$

Direct integration applying time ordering (T) gives the *Dyson* series, familiar from the interaction picture of quantum mechanics and time dependent perturbation theory [2];

$$\begin{aligned} \sigma(t) &= \sigma(0) - iT \int_0^t [\mathcal{H}(t'), \sigma(0) - \sigma_{eq}] dt' \\ &+ (-i)^2 T \int_0^t dt' \int_0^{t'} dt'' [\mathcal{H}(t), [\mathcal{H}(t''), \sigma(0) - \sigma_{eq}]] + \dots \\ &+ (-i)^n T \int_0^t dt' \int_0^{t'} dt'' \dots \int_0^{t^{(n-1)}} dt^{(n)} \\ &\times [\mathcal{H}(t'), [\mathcal{H}(t''), [\dots, [\mathcal{H}(t^{(n)}), \sigma(0) - \sigma_{eq} \dots]]]] + \dots \end{aligned} \quad (2.75)$$

One assumes that the time dependent Hamiltonian may be approximated by

an average Hamiltonian $\overline{\mathcal{H}}(t_1, t_2)$, within a specific time interval $t_1 < t < t_2$. It may be derived through either diagonalization of the time evolution operator or Baker-Campbell-Hausdorff (or Magnus) expansion. We take $\mathcal{H}(t)$ to be piecewise constant in successive small time intervals;

$$\mathcal{H}(t) = \mathcal{H}_k \text{ for } (\tau_1 + \tau_2 + \dots + \tau_{k-1}) < t < (\tau_1 + \tau_2 + \dots + \tau_k) \quad (2.76)$$

The time dependence of the density operator,

$$\dot{\sigma} = -i[\mathcal{H}(t), \sigma] \quad (2.77)$$

may be integrated to give:

$$\sigma(t_c) = U(t_c)\sigma(0)U(t_c)^{-1} \quad (2.78)$$

where

$$U(t_c) = \exp(-i\mathcal{H}_n\tau_n)\dots\exp(-i\mathcal{H}_1\tau_1)$$

$$t_c = \sum_{k=1}^n \tau_k \quad (2.79)$$

Continuing the process over successive intervals and remembering that the product of the unitary transformations, is itself a unitary transformation, one obtains:

$$U(t_c) = \exp\{-i\overline{\mathcal{H}}(t_c)t_c\} \quad (2.80)$$

The Baker-Campbell-Hausdorff relation

$$e^B e^A = \exp\left\{A + B + \frac{1}{2}[B, A] + \frac{1}{2}([B, [B, A]] + [[B, A], A]) + \dots\right\} \quad (2.81)$$

may be used for two sequential time intervals τ_1, τ_2 to give:

$$\begin{aligned} \overline{\mathcal{H}}(t_c) = & \frac{i}{t_c} \left\{ -i(\mathcal{H}_1\tau_1 + \mathcal{H}_2\tau_2) - \frac{1}{2}[\mathcal{H}_2\tau_2, \mathcal{H}_1\tau_1] \right. \\ & \frac{1}{12}(i[\mathcal{H}_2\tau_2, [\mathcal{H}_2\tau_2, \mathcal{H}_1\tau_1]] \\ & + i[[\mathcal{H}_2\tau_2, \mathcal{H}_1\tau_1], \mathcal{H}_1\tau_1]) \\ & \left. + \dots \right\} \end{aligned} \quad (2.82)$$

The average Hamiltonian can be decomposed into different terms:

$$\overline{\mathcal{H}}(t_c) = H^0 + H^1 + H^2 + \dots \quad (2.83)$$

For an interval composed of discrete time periods;

$$\begin{aligned} H^0 &= \frac{1}{t_c} \{ \mathcal{H}_1\tau_1 + \mathcal{H}_2\tau_2 + \dots + \mathcal{H}_n\tau_n \} \\ H^1 &= -\frac{i}{2t_c} \{ [\mathcal{H}_2\tau_2, \mathcal{H}_1\tau_1] + [\mathcal{H}_3\tau_3, \mathcal{H}_1\tau_1] + [\mathcal{H}_3\tau_3, \mathcal{H}_2\tau_2] + \dots \}, \\ H^2 &= -\frac{1}{6t_c} \{ [\mathcal{H}_3\tau_3, [\mathcal{H}_2\tau_2, \mathcal{H}_1\tau_1]] + [[\mathcal{H}_3\tau_3, \mathcal{H}_3\tau_3, \mathcal{H}_2\tau_2], \mathcal{H}_1\tau_1] \\ & \frac{1}{2}[\mathcal{H}_2\tau_2, [\mathcal{H}_2\tau_2, \mathcal{H}_1\tau_1]] + \frac{1}{2}[[\mathcal{H}_2\tau_2, \mathcal{H}_2\tau_2, \mathcal{H}_1\tau_1], \mathcal{H}_1\tau_1] + \dots \} \end{aligned} \quad (2.84)$$

In the infinitesimal limit as $\tau_k \rightarrow 0$ and allowing \mathcal{H} to vary continuously, then we find:

$$U(t_c) = T \exp \left\{ -i \int_0^{t_c} \mathcal{H}(\tau) d\tau \right\} = \exp(-i\overline{\mathcal{H}}t_c) \quad (2.85)$$

where T is the Dyson time ordering operator. Equating, one finds:

$$\begin{aligned}
 H^0 &= \frac{1}{t_c} \int_0^{t_c} \mathcal{H}(t_1) dt_1, \\
 H^1 &= -\frac{i}{2t_c} \int_0^{t_c} dt_2 \int_0^{t_2} dt_1 [\mathcal{H}(t_2), \mathcal{H}(t_1)], \\
 H^2 &= -\frac{1}{6t_c} \int_0^{t_c} dt_3 \int_0^{t_3} dt_2 \int_0^{t_2} dt_1 \{[\mathcal{H}(t_3), [\mathcal{H}(t_2), \mathcal{H}(t_1)]] \\
 &\quad + [[\mathcal{H}(t_3), \mathcal{H}(t_2)], \mathcal{H}(t_1)]\}, \tag{2.86}
 \end{aligned}$$

the Magnus expansion. This technique is of central importance in developing expressions for frequency eigenvalues of the quadrupolar Hamiltonian and thus experimental spectra for quadrupolar nuclei.

2.4 Experimental NMR

2.4.1 Average Hamiltonian

The density operator is a popular means of describing experimental NMR. It's matrix representation in a particular basis is diagonalized and the time evolution propagated under an average Hamiltonian. In this work, it is implicitly assumed that the Magic Angle Spinning (MAS) speed is synchronized with evolution periods in the pulse sequence. MAS [26] is essential for scaling or eliminating second rank NMR interactions proportional to $P_2(\cos \beta)$. These interactions include the chemical shift anisotropy, the first-order quadrupole interaction and heteronuclear dipole-dipole interaction. Of most importance to this work is the quadrupole interaction, to be discussed here.

Before determining an average Hamiltonian, the quadrupole interaction is

recast in light of irreducible tensor operator notation [59, 60, 61].

$$\mathcal{H}_Q = \nu_Q \sum_{u=-2}^2 (-1)^u V_{2,-2} K^{(2,u)}$$

$$\text{with } \nu_Q = \frac{eQ}{2I(2I-1)\hbar} \quad (2.87)$$

In any frame, the relationship between the spherical and Cartesian tensors:

$$\begin{aligned} V_{2,0} &= \frac{1}{2}\sqrt{6}V_{zz} & V_{2,1} &= -V_{xz} - iV_{yz} & V_{2,-1} &= V_{xz} - iV_{yz} \\ V_{2,2} &= \frac{1}{2}(V_{xx} - V_{yy}) + iV_{xy} & V_{2,-2} &= \frac{1}{2}(V_{xx} - V_{yy}) - iV_{xy} & K^{(2,0)} &= \frac{1}{\sqrt{6}}[3I_z^2 - I(I+1)] \\ K^{(2,1)} &= -\frac{1}{2}I_+(2I_z + 1) & K^{(2,-1)} &= \frac{1}{2}I_-(2I_z - 1) & K^{(2,2)} &= \frac{1}{2}I_-I_- \end{aligned}$$

By substituting back into the previous equation, one finds in the PAS by comparison:

$$V_{2,0}^{\text{PAS}} = \sqrt{\frac{3}{2}}eq; \quad V_{2,\pm 1}^{\text{PAS}} = 0; \quad V_{2,\pm 2} = \frac{1}{2}eq\eta \quad (2.88)$$

Now it is assumed for the remainder of this work that the quadrupole interaction may be treated as a weak perturbation on the Zeeman levels, which is relevant where the quadrupole coupling constant is less than the Larmor frequency. One begins by considering the time evolution of the operator in the ‘interaction’ representation:

$$\begin{aligned} H_Q(t) &= \exp(iH_z t) H_Q \exp(-iH_z t) \\ &= N_Q \sum_{u=-2}^2 (-1)^u V_{2,-u} K^{(2,u)} \exp(-iu\omega_o t) \end{aligned} \quad (2.89)$$

Using the previously mentioned Magnus expansion to find the average value of the Hamiltonian, since the oscillations of equation 2.89 occur very rapidly;

$$H_{Q0} = \frac{1}{t_L} \int_0^{t_L} H_Q(t) dt = N_Q V_{2,0} K^{(2,0)} \quad (2.90)$$

$$\begin{aligned}
H_{Q1} &= \frac{-i}{2t_L} \int_0^{t_L} dt \int_0^t dt' [H_Q(t), H_Q(t')] \\
&= \frac{-N_Q^2}{\omega_0} \sum_{u \neq 0} \frac{1}{u} \left(\frac{1}{2} V_{2,u} V_{2,-u} [K^{(2,u)}, K^{(2,-u)}] + (-1)^u V_{2,0} V_{2,-u} [K^{(2,0)}, K^{(2,u)}] \right) \\
&= \frac{-N_Q^2}{\omega_0} \left(\sqrt{\frac{3}{8}} V_{2,0} V_{2,-1} I_+ (2I_z + 1)^2 - \sqrt{\frac{3}{8}} V_{2,0} V_{2,1} I_- (2I_z - 1)^2 \right. \\
&\quad + \sqrt{\frac{3}{2}} V_{2,0} V_{2,-2} I_+^2 (I_z + 1) + \sqrt{\frac{3}{2}} V_{2,0} V_{2,2} I_-^2 (I_z - 1) + \frac{1}{2} V_{2,-1} V_{2,1} I_z \\
&\quad \left. \times [4I(I+1) - 8I_z^2 - 1] + \frac{1}{2} V_{2,-2} V_{2,2} I_z [2I(I+1) - 2I_z^2 - 1] \right) \quad (2.91)
\end{aligned}$$

Generally, only secular terms (those that commute with \mathcal{H}_z) are considered, in which case one is left with:

$$H_Q^{(1)} = H_{Q0} = N_Q \frac{1}{\sqrt{6}} [3I_z^2 - I(I+1)] V_{2,0} \quad (2.92)$$

$$\begin{aligned}
H_Q^{(2)} = H_{Q1} &= \frac{-N_Q^2}{\omega_0} \left(\frac{1}{2} V_{2,-1} V_{2,1} [4I(I+1) - 8I_z^2 - 1] \right. \\
&\quad \left. + \frac{1}{2} V_{2,-2} V_{2,2} [2I(I+1) - 2I_z^2 - 1] \right) I_z \quad (2.93)
\end{aligned}$$

More convenient for ascertaining eigenvalues and frequencies is their expression in the form of higher rank tensors e.g.,

$$\begin{aligned}
H_Q^{(2)} &= \frac{-N_Q^2}{\omega_0} \left(\frac{1}{70} \sqrt{7} W_{4,0} [17L^{(3,0)} - 6L^{(1,0)}] \right. \\
&\quad \left. + \frac{1}{\sqrt{35}} W_{2,0} [3L^{(3,0)} + L^{(1,0)}] - \frac{1}{10} \sqrt{2} W_{0,0} [3L^{(3,0)} - 4L^{(1,0)}] \right) \quad (2.94)
\end{aligned}$$

The tensor W contains components of the electric field gradient, whilst L pertains to the spin operators. Explicitly, the tensor W is related to the tensor V via the

Clebsch-Gordon coefficients,

$$W_{j,M} = \sum_{m_1, m_2} \langle j_1 j_2 m_1 m_2 | JM \rangle V_{j_1, m_1} V_{j_2, m_2} \quad (2.95)$$

and the L are given by:

$$L^{(1,0)} = \frac{1}{5} \sqrt{10} [I(I+1) - \frac{3}{4}] I_z \quad (2.96)$$

$$L^{(3,0)} = \frac{1}{5} \sqrt{10} [3I(I+1) - 5I_z^2 - 1] I_z \quad (2.97)$$

The latter are not normalized; in terms of normalized tensor operators $P^{(1,0)}$ and $P^{(3,0)}$ one may write:

$$L^{(1,0)} = \sqrt{\frac{2}{5}} [I(I+1) - \frac{3}{4}] P^{(1,0)} \quad (2.98)$$

$$L^{(3,0)} = -2P^{(3,0)} \quad (2.99)$$

Therefore

$$\begin{aligned} H_Q^{(2)} = \frac{-N_Q^2}{\omega_0} & \left(\frac{-17}{5\sqrt{7}} W_{4,0} P^{(3,0)} - \frac{3}{35} \sqrt{\frac{16}{5}} [I(I+1) - \frac{3}{4}] \right. \\ & \times W_{4,0} P^{(1,0)} - \frac{6}{\sqrt{35}} W_{2,0} P^{(3,0)} + \frac{\sqrt{14}}{35} [I(I+1) - \frac{3}{4}] \\ & \left. \times W_{2,0} P^{(1,0)} + \frac{3\sqrt{2}}{5} W_{0,0} P^{(3,0)} + \frac{4}{5\sqrt{5}} [I(I+1) - \frac{3}{4}] W_{0,0} P^{(1,0)} \right) \quad (2.100) \end{aligned}$$

If one denotes distinct energy levels by r, c , then the shift to the standard Zeeman frequency may be determined as,

$$\omega_{r,c} = \langle r | (H_Q^{(1)} + H_Q^{(2)}) | r \rangle - \langle c | (H_Q^{(1)} + H_Q^{(2)}) | c \rangle$$

which is the sum of first and second order contributions:

$$\omega_{r,c}^{(1)} + \omega_{r,c}^{(2)} \quad (2.101)$$

To first order, the shift is:

$$\omega_{r,c}^{(1)} = N_Q \sqrt{\frac{3}{2}} (r^2 - c^2) V_{2,0}, \quad (2.102)$$

which for a symmetric transition ($r = -c$) is zero. To second order:

$$\omega_{r,c}^{(2)} = \frac{-N_Q^2}{\omega_0} (r - c) \left\{ \frac{1}{70} \sqrt{\frac{35}{2}} W_{4,0} A^{(4)} + \frac{1}{28} \sqrt{14} W_{2,0} A^{(2)} - \frac{1}{\sqrt{5}} W_{0,0} A^{(0)} \right\} \quad (2.103)$$

where

$$\begin{aligned} A^{(4)}(I, r, c) &= 18I(I+1) - 34(r^2 + rc + c^2) - 5 \\ A^{(2)}(I, r, c) &= 8I(I+1) - 12(r^2 + rc + c^2) - 3 \\ A^{(0)}(I, r, c) &= I(I+1) - 3(r^2 + rc + c^2) \end{aligned} \quad (2.104)$$

Static Crystal

The transformation for $V_{2,0}$ from the principal axis system is rather simple in the case of a non-rotating single crystal:

$$\begin{aligned} V_{2,0} &= \sum_{u=-2}^2 V_{2,u}^{\text{PAS}} D_{u,0}^{(2)}(\alpha, \beta, \phi) = \\ &= \frac{1}{2} \sqrt{6} e q \left[\frac{1}{2} (3 \cos^2 \beta - 1) + \frac{1}{2} \eta \sin^2 \beta \cos 2\alpha \right] \end{aligned} \quad (2.105)$$

One may then write the 1st order quadrupole interaction as:

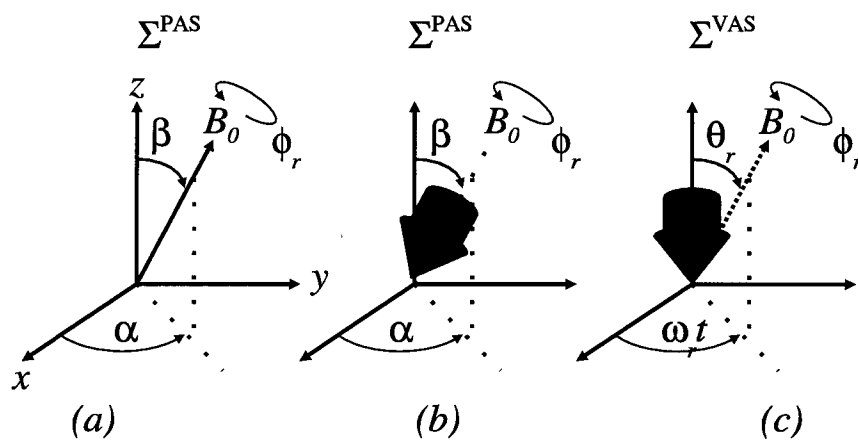


FIG. 2.1: Euler angles for: (a) the Principal Axis System (PAS) in the crystal frame (b) PAS in rotor fixed frame, (c) PAS and rotor relationship to static B field.

$$H_Q^{(1)} = \frac{1}{4}(3I_z^2 - I(I+1))\Omega_Q[3\cos^2\beta - 1 + \eta\sin^2\beta\cos 2\alpha] \quad (2.106)$$

with

$$\Omega_Q = eq\nu_Q = \frac{e^2qQ}{2I(2I-1)\hbar}$$

Tensor components $W_{4,0}$, $W_{2,0}$ and $W_{0,0}$ of the electric field gradient;

$$W_{2x,0} = \sum_{u=-x}^x W_{2x,2u}^{\text{PAS}} D_{2u,0}^{(2x)}(\alpha, \beta, \phi) \quad (2.107)$$

Hence for the second order quadrupole frequency:

$$w_{r,c}^{(2)} = -\frac{r-c}{2\omega_0}\Omega_Q^2 \sum_k^{0,1,2} A^{(2k)}(I, r, c) \sum_{u=-k}^k B_{2k,2u}(\eta) D_{2u,0}^{(2k)}(\alpha, \beta, \phi) \quad (2.108)$$

with

$$\begin{aligned} B_{0,0}(\eta) &= -\frac{1}{5}(\eta^2 + 3), & B_{2,0}(\eta) &= \frac{1}{14}(\eta^2 - 3), \\ B_{2,\pm 2}(\eta) &= \frac{1}{14}\eta\sqrt{6}, & B_{4,0}(\eta) &= \frac{1}{140}(\eta^2 + 18), \\ B_{4,\pm 2}(\eta) &= \frac{3}{140}\eta\sqrt{10}, & B_{4,\pm 4}(\eta) &= \frac{1}{4\sqrt{70}}\eta^2 \end{aligned}$$

Magic Angle Spinning

In the variable angle experiment, an additional step in transforming between the PAS and the rotor frame is necessary:

$$V_{2,u}^{\text{VAS}} = \sum_{j=-2}^2 V_{2,j}^{\text{PAS}} D_{j,u}^{(2)}(\alpha_1, \beta_1, \phi_1), \quad (2.109)$$

$$V_{2,0} = \sum_{u=-2}^2 V_{2,u}^{\text{VAS}} D_{u,0}^{(2)}(\omega_r t, \theta_r, \phi_r) \quad (2.110)$$

For this case, the first order Quadrupole Interaction:

$$\omega_{r,c}^{(1)\text{VAS}} = \nu_Q \frac{1}{2} \sqrt{6} (r^2 - c^2) \sum_{u=-2}^2 D_{u,0}^{(2)}(\omega_r t, \theta_r, \phi_r) \sum_{j=-2}^2 V_{2,j}^{\text{PAS}} D_{j,u}^{(2)}(\alpha_1, \beta_1, \phi_1) \quad (2.111)$$

Similarly, in determining the second order shift, one finds:

$$W_{2x,u}^{\text{VAS}} = \sum_{j=-x}^x W_{2x,2j}^{\text{PAS}} D_{2j,u}^{(2x)}(\alpha_1, \beta_1, \phi_1) \quad (2.112)$$

$$W_{2x,0} = \sum_{u=-2x}^2 x W_{2x,u}^{\text{VAS}} D_{u,0}^{(2x)}(\omega_r t, \theta_r, \phi_r) \quad (2.113)$$

and hence:

$$\omega_{r,c}^{(2)\text{VAS}} = -\frac{r-c}{2\omega_0} \Omega_Q^2 \sum_{x=0}^2 A^{(2x)}(I, r, c) \sum_{u=-2x}^{2x} D_{u,0}^{(2x)}(\omega_r t, \theta_r, \phi_r) \sum_{j=-x}^x B_{2x,2j}(\eta) D_{2j,u}^{(2x)}(\alpha_1, \beta_1, \phi_1) \quad (2.114)$$

Now $D_{u,0}^{(2x)}$ is proportional to $\exp(-iu\omega_r t)$ and thus spinning sidebands are observed in the frequency domain. In the high spinning speed approximation, one assumes that the only non-zero term is for $u = 0$, thus:

$$\omega_{r,c}^{(1)\text{VAS}'} = \nu_Q \frac{1}{2} \sqrt{6} (r^2 - c^2) d_{0,0}^{(2)}(\theta_r) \sum_{j=-2}^2 V_{2,j}^{\text{PAS}} D_{j,0}^{(2)}(\alpha_1, \beta_1, \phi_1) \quad (2.115)$$

$$\omega_{r,c}^{(2)\text{VAS}'} = -\frac{r-c}{2\omega_0} \Omega_Q^2 \sum_{x=0}^2 A^{(2x)}(I, r, c) d_{0,0}^{(2x)}(\theta_r) \sum_{j=-x}^x B_{2x,2j}(\eta) D_{2j,0}^{(2x)}(\alpha_1, \beta_1, \phi_1) \quad (2.116)$$

$$\begin{aligned} &= -\frac{r-c}{2\omega_0} \Omega_Q^2 \{ A^{(0)}(I, r, c) B_{0,0}(\eta) + A^{(2)}(I, r, c) d_{0,0}^{(2)}(\theta_r) [B_{2,0}(\eta) d_{0,0}^{(2)}(\beta_1) \\ &\quad + 2B_{2,2}(\eta) d_{2,0}^{(2)}(\beta_1) \cos 2\alpha_1] + A^{(4)}(I, r, c) d_{0,0}^{(4)}(\theta_r) [B_{4,0}(\eta) d_{0,0}^{(4)}(\beta_1) \\ &\quad + 2B_{4,2}(\eta) d_{2,0}^{(4)}(\beta_1) \cos 2\alpha_1 + 2B_{4,4}(\eta) d_{4,0}^{(4)}(\beta_1) \cos 4\alpha_1] \} \quad (2.117) \end{aligned}$$

Further, under the Magic Angle Spinning condition of $P_2(\cos \theta_r) = 0$, there remains for the first and second order quadrupole interactions:

$$\omega_{r,c}^{(1)\text{fast MAS}} = 0, \quad (2.118)$$

$$\begin{aligned} \omega_{r,c}^{(2)\text{fast MAS}} = \omega_{r,c}^{\text{iso}} - \frac{r-c}{2\omega_0} \Omega_Q^2 \{ & A^{(0)}(I, r, c) B_{0,0}(\eta) + A^{(4)}(I, r, c) [B_{4,0}(\eta) d_{0,0}^{(4)}(\beta) + \\ & 2B_{4,2}(\eta) d_{2,0}^{(4)}(\beta) \cos 2\alpha + 2B_{4,4}(\eta) d_{4,0}^{(4)}(\beta) \cos 4\alpha] P_4(\cos \theta_m) \}. \end{aligned} \quad (2.119)$$

where $\omega_{r,c}^{\text{iso}}$ is the isotropic chemical shift for the r, c transition. These frequency eigenvalues form the mathematical basis of lineshape simulation, developed further shortly. Simulations are of paramount importance in interpreting and understanding NMR experimental details.

2.4.2 Phase Cycling

A general NMR experiment may be considered to be a sequence of excitation, evolution, mixing and acquisition processes [70]. It has been implicitly assumed here that the Average Hamiltonian, relevant during all periods of experiments, is dominated by the quadrupolar interaction and experiments are performed using fast Magic Angle Spinning. Moreover, the Hamiltonian during RF pulses (excitation) may be considered to be a combination of the 1st order quadrupole contribution and external RF energy:

$$H_{ex} = H_{rf} + H_Q^{(1)}$$

provided pulse durations are much shorter than the rotor period. During free precession (evolution) of the spin system, the interaction Hamiltonian becomes:

$$H_{ev} = H_{CS} + H_Q^{(2)}$$

The process of mixing is one of coherence transfer, which occurs just after the evolution period. This coherence transfer is the first step toward acquisition, where (usually) a pulse applied selectively to the central transition converts multiple quantum coherence into the detectable single quantum coherence (transverse magnetization). It is assumed that sufficient time elapses between experiments for spins to completely relax with characteristic time T_{1z} . In the high temperature approximation the density operator at equilibrium is thus given by $\rho(0) = I_z$ with coherence order equal to zero. At the end of the first RF pulse the density operator is given by:

$$\rho(t_1) = \exp[-iH_a t_p] \rho(0) \exp[iH_a t_p] \quad (2.120)$$

In general, the Hamiltonian is not diagonal in the Zeeman basis but however in terms of the unitary transformation:

$$X = T^\dagger H_a T$$

one may re-write the density operator at time t_p as:

$$\rho(t_p) = T \exp(-iX t_p) T^\dagger \rho(0) T \exp(iX t_p) T^\dagger \quad (2.121)$$

The RF pulse H'_{rf} (equation 2.12) in general has arbitrary phase ϕ in the rotating frame. It is assumed that only secular Hamiltonian contributions or

those that commute with the Zeeman interaction are considered. In this case, the density operator for an x pulse and arbitrary phase are related by:

$$\rho(t_p)' = \exp(-i\phi I_z)\rho(t_p)\exp(i\phi I_z) \quad (2.122)$$

The matrix elements are therefore related by:

$$\langle r|\rho(t_p)'|c\rangle = \langle r|\exp(-i\phi I_z)\rho(t_p)\exp(i\phi I_z)|c\rangle = \langle r|\rho(t_p)|c\rangle \exp[-i(r-c)\phi] \quad (2.123)$$

The fact that the $r - c = p$ quantum coherence is dephased by an angle ϕ provides a useful technique for selection of a desired coherence during the evolution period [32, 38]. The coherence transfer pathway during a pulse sequence is largely determined by the pulse sequence variables including power, duration, pulse profile and inter-pulse spacing. However, given the existence of a coherence order change, predicated on the factors mentioned, a desired Coherence Transfer Pathway (CTP) may be selected by summing a specific number of experimental transients. In terms of the coherence order change Δp created by a pulse with phase ϕ , and receiver phase ϕ_r , one may write the relationship as:

$$\Phi_{\text{path}} = \Delta p_1\phi_1 + \Delta p_2\phi_2 + \dots + \phi_r = \text{const.} \quad (2.124)$$

Ideally, unwanted pathways have an amplitude which traverses the complex plane and whose additive value 'cycles' between some number and zero, figure 2.2. Table 2.1 is an example of a phase cycle for the split- t_1 type MQMAS experiment [19]; $(m)n$ means $n/m * 360$ degrees, $\{x\} * 12$ means repeat x degrees 12 times and $\wedge 2$ means increment by two units of degree, here $(4) = 90$ degrees. Using Equation 2.124, one may determine the cumulative sum of the complex amplitudes

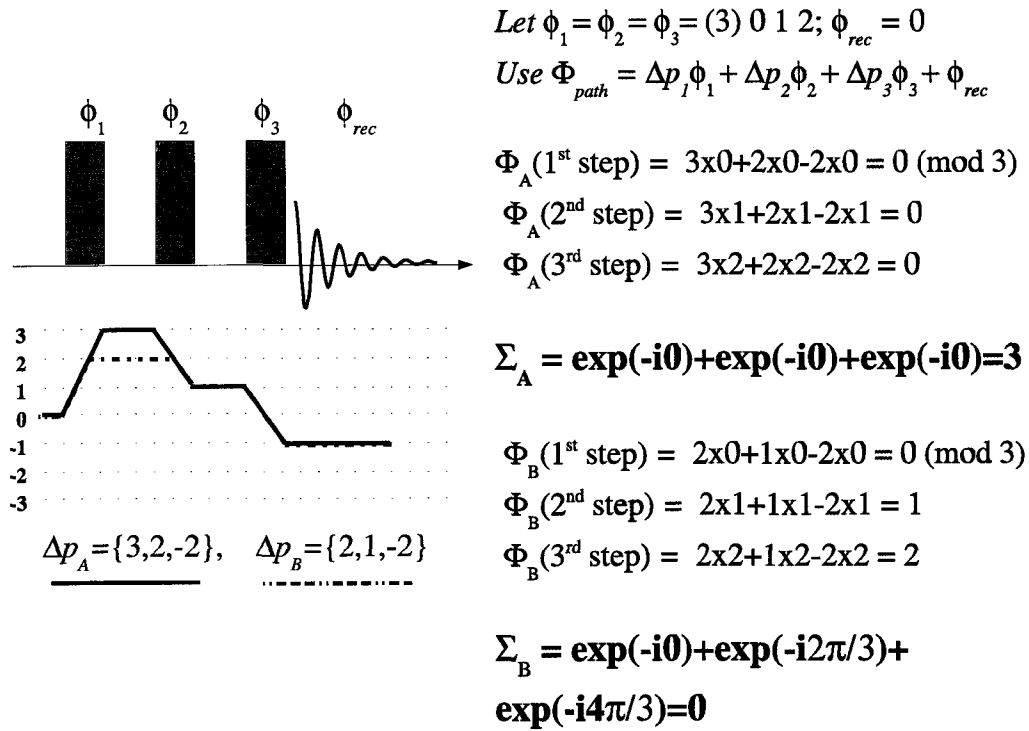


FIG. 2.2: A trivial three pulse experiment with phase cycle, showing the behavior of complex amplitude for two coherence transfer pathways.

$e^{-i\Phi_{path}}$ over the course of the complete phase cycle; several are plotted in figure 2.3.

For this case of low spin ($I=3/2$) and few pulses, all unwanted pathways are able to be removed by conventional phase cycling. For high spin this is not generally true and the time to accomplish suppression of even a modest number of pathways becomes prohibitive. The problem may be better appreciated by considering the conventional algorithm for producing nested phase cycles:

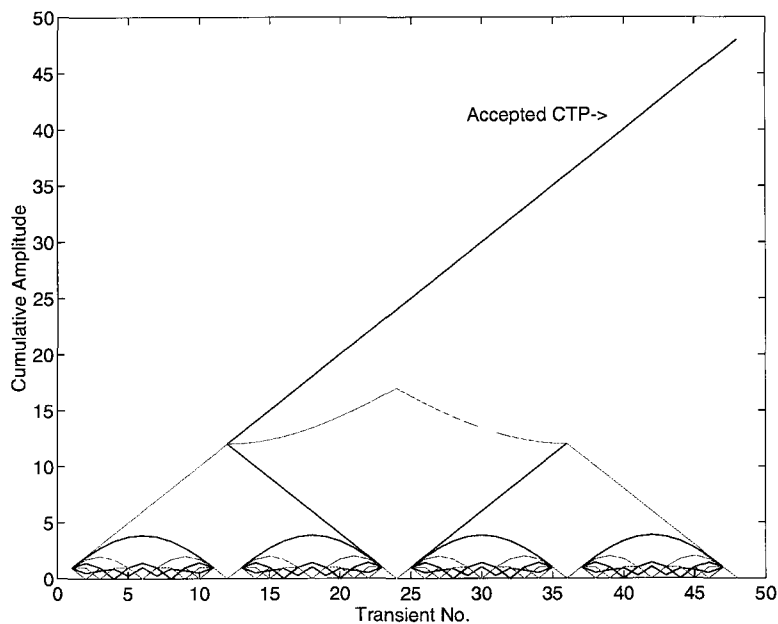


FIG. 2.3: Cumulative sums of coherence transfer pathways for split t_1 MQMAS experiment. Phase cycling successfully eliminates all but desired pathway, the unwanted pathways having different numerical periodicities.

TABLE 2.1: Phase cycle for split- t_1 (whole echo) MQMAS experiment.

$$\begin{array}{l}
 \phi_1 = (12)0\ 1\ 2\ 3\ 4\ 5\ 6\ 7\ 8\ 9\ 10\ 11 \\
 \phi_2 = 0 \\
 \phi_3 = (4)\{0\}^*12\ \{1\}^*12\ \{2\}^*12\ \{3\}^*12 \\
 \phi_r = (4)\{\{0\ 3\ 2\ 1\}^*3\}^2
 \end{array}$$

$$\begin{aligned}
\phi_1 &= \frac{2\pi}{n_1} m \\
\phi_2 &= \frac{2\pi}{n_2} \text{floor} \left(\frac{m}{n_1} \right) \\
\phi_3 &= \frac{2\pi}{n_3} \text{floor} \left(\frac{m}{n_1 n_2} \right) \\
&\vdots \\
\phi_r &= -\Delta p_1 \phi_1 - \Delta p_2 \phi_2 - \Delta p_3 \phi_3 \dots
\end{aligned} \tag{2.125}$$

Here, m is the experimental transient number, ϕ are the pulse and receiver phases, Δp is the change in coherence order produced by the pulse and n is chosen according to the number of possible coherence transfers to be eliminated per pulse. This scheme scales very poorly with increasing spin number and number of pulses and in fact often becomes prohibitive for large I . Levitt et al proposed the ‘cogwheel’ phase cycling method [55, 4] which drastically reduces the phase cycle length in a number of cases. Examining figure 2.2, it is apparent that CTP’s have different periodicities, using the conventional nested approach. Levitt recognized that pathways have different ‘winding numbers’ and proposes choosing phases according to a numerical search, guided by several conjectures [11]. The result is often much shorter phase cycles, and the period of different CTP’s becomes coincident.

2.4.3 Data Acquisition

The theory which has been discussed in detail to this point primarily concerns the existence of eigen-frequencies in the NMR system and their selection through phase cycling. The object of study is comprised of a material sample within a static magnetic field. Radio frequency energy is used to perturb the system and the subsequent frequency response is acquired using a Fourier Transform NMR spectrometer, figure 2.3. Frequency synthesis is gated by control circuitry and pulsed RF energy is applied via a tuned network to the sample within a small

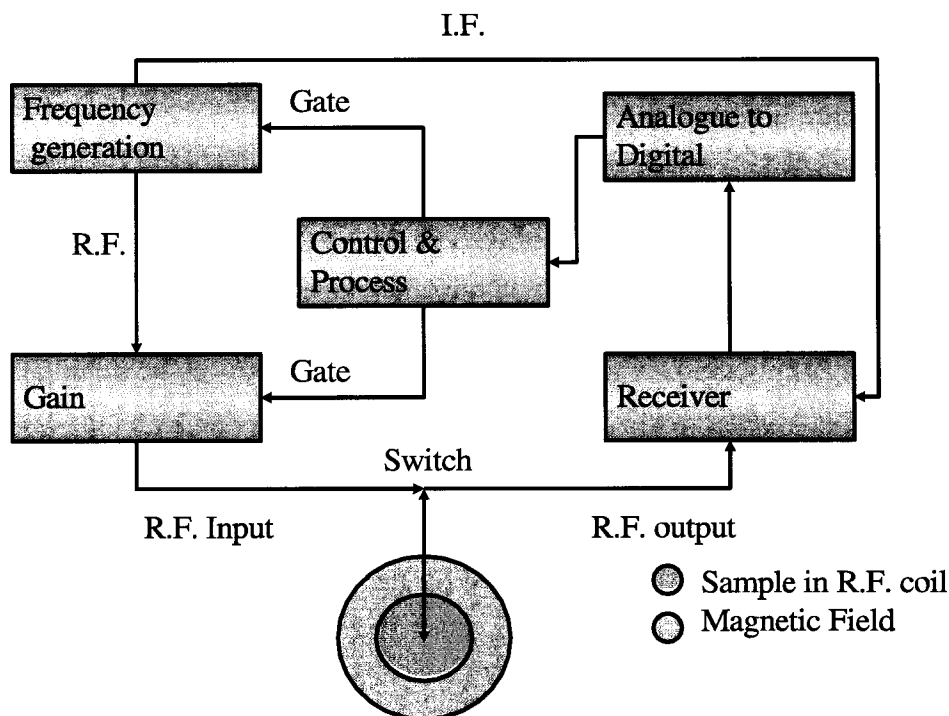


FIG. 2.4: Block schematic for a Fourier transform NMR spectrometer. Radio frequency energy is pulsed and after gain gated into the sample within RF coil (the probe). A system response is acquired by the receiver and after sufficient gain and demodulation using the Intermediate Frequency (IF), digitized and processed. Control and processing functions are carried out by a combination of software and hardware.

solenoid.

The latter configuration roughly comprises the probe, embedded in the static magnetic field. After RF excitation, an emf $h(t)$ referred to the Free Induction Decay (FID) is generated within the coil and the system response is digitized after demodulation (the carrier usually corresponds to the Larmor frequency of the probe nuclei) and Fourier transformed [72];

$$F(\omega) = \int_{-\infty}^{\infty} h(t)e^{-i\omega t} dt$$

$$h(t) = \frac{1}{2\pi} \int_{-\infty}^{\infty} H(\omega) e^{i\omega t} d\omega \quad (2.126)$$

The Bloch equations give the classical description for the evolution of the macroscopic magnetization M . They are presented here as a model of the system response in data acquisition, but also because the solutions maybe used to 'build-up' quadrupole powder patterns, to be discussed shortly. For now, we consider only the effects of a simple chemical shielding interaction σ in the PAS:

$$\frac{d\mathbf{M}}{dt} = \gamma(1 - \sigma)\mathbf{M} \times \mathbf{H} - R \cdot (\mathbf{M} - \mathbf{M}_0) \quad (2.127)$$

where R is a diagonal matrix of transverse and longitudinal relaxation rates T_2 and T_1 respectively and the equilibrium magnetization has a form similar to eq. 2.1. In terms of vector components:

$$\frac{dM_x}{dt} = \gamma(1 - \sigma)[M_y H_z - M_z H_y] - \frac{M_x}{T_2} \quad (2.128)$$

$$\frac{dM_y}{dt} = \gamma(1 - \sigma)[M_z H_x - M_x H_z] - \frac{M_y}{T_2} \quad (2.129)$$

$$\frac{dM_z}{dt} = \gamma(1 - \sigma)[M_x H_y - M_y H_x] - \frac{M_z - M_0}{T_1} \quad (2.130)$$

For times where $H_x = H_y = 0$ (free precession) and the z -component H_z is a constant H_0 , one finds:

$$\frac{d(M_x + iM_y)}{dt} = -i(M_x + iM_y)\omega_0 - \frac{M_x + iM_y}{T_2} \quad (2.131)$$

$$\frac{dM_z}{dt} = -\frac{M_z - M_0}{T_1} \quad (2.132)$$

where $\omega_0 = \gamma(1 - \sigma)H_0$ is the chemically shifted Larmor frequency. The solution

to these equations is of the Lorentzian form:

$$M_{-}(t) = M_x + iM_y = [M_x(0) - iM_y(0)] \exp(-i\omega_0 t - t/T_2) \quad (2.133)$$

$$M_z(t) = M_0 + [M_z(0) - M_0] \exp(-t/T_1) \quad (2.134)$$

Now $M_{-}(t)$ is proportional to the operator I_{-} with coherence order $\Delta m = -1$, which corresponds to the $1/2 \leftrightarrow -1/2$ central transition, and satellite transitions with the same -1 coherence order. It is this response which generates an emf in the coil and is gathered during acquisition. The real component is absorptive (figure 2.4) and imaginary dispersive (figure 2.5) in the frequency domain, respectively.

$$F(\omega) = \int_0^{\infty} M_{-}(t) \exp(i\omega t) dt = \frac{M_x(0) + iM_y(0)}{-i(\omega - \omega_0)^2 + 1/T_2^2} \quad (2.135)$$

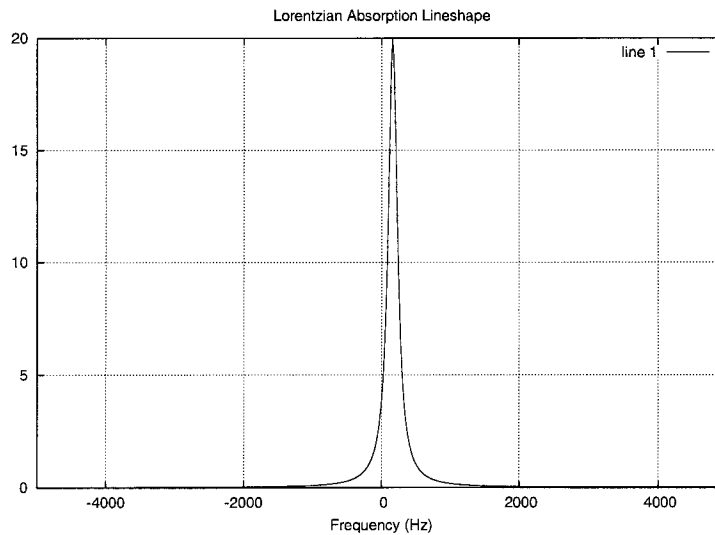


FIG. 2.5: Frequency spectrum of the absorption Lorentzian; frequency 159.15 Hz, broadening or full width at half maximum height 500 Hz

The receiver is generally of the phase sensitive or quadrature type in order

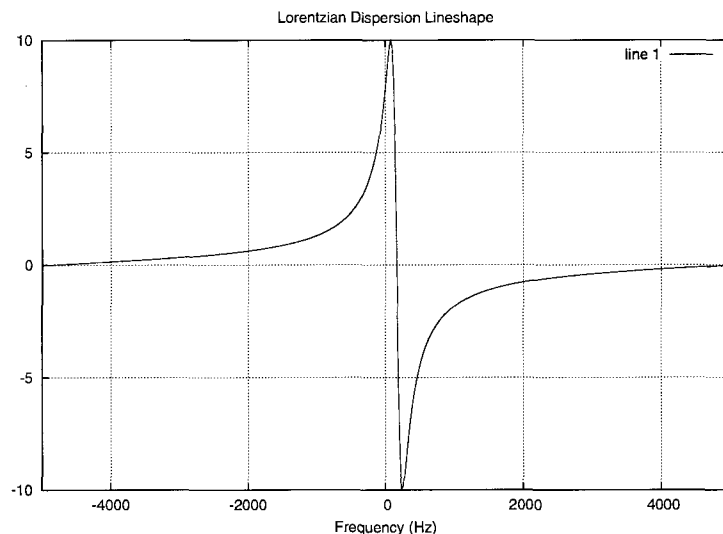


FIG. 2.6: Frequency spectrum of the dispersion Lorentzian; frequency 159.15 Hz, broadening or full width at half maximum height 500 Hz

to detect both components. A pure absorption frequency spectrum is desired for ease of interpretation, although naturally the time domain response contains the same information. Figure 2.6 is a simple schematic of the one dimensional, pulse sequence. Without more complex synthesis, the gated RF energy has a frequency spectrum which corresponds to a sinc function.

It should be emphasized again that the Bloch equations ignore the effects of the quadrupole interaction, and the associated anisotropy. In general, chemically distinct quadrupole lineshapes for even moderately large coupling constants often overlap in one dimension. A prescription for overcoming this problem involves collecting data as a function of two independent time intervals in the pulse sequence [70], figure 2.7. Fourier transformation with respect to both time intervals gives additional information and increased resolution. This is made possible by correlations between directly observable single quantum coherence transitions ($\Delta m = \pm 1$) and multiple quantum transitions ($\Delta m \neq \pm 1$) which evolve during

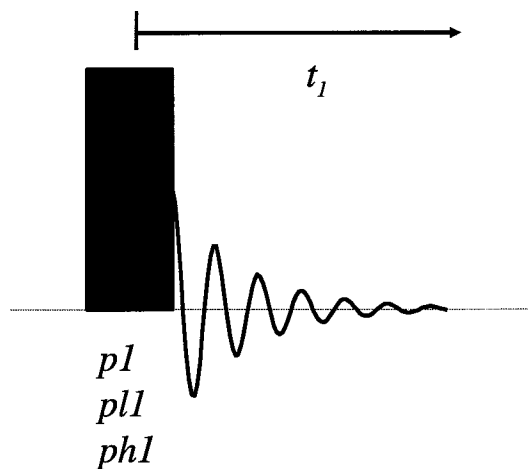


FIG. 2.7: Block schematic for single pulse experiment. Pulse duration $p1$, power level pl , phase $ph1$. Acquisition time is $t1$.

the inter-pulse delay(s). A so-called ‘shearing transformation’ [60] is applied after the Fourier transform in the direct dimension, but before the second transform. One may begin by considering the Lorentzian model for the signal:

$$S(t_1, t_2) = S_0 e^{(i\omega_m - R_1)t_1} e^{(i\omega_{-1} - R_2)t_2}, \quad (2.136)$$

where R_1, R_2 are phenomenological relaxation rates and ω_m, ω_{-1} are the multiple and single quantum coherence frequencies. The phases of the signal are functions of the broadening effects of anisotropy. The essential idea of MQMAS [6] and similar

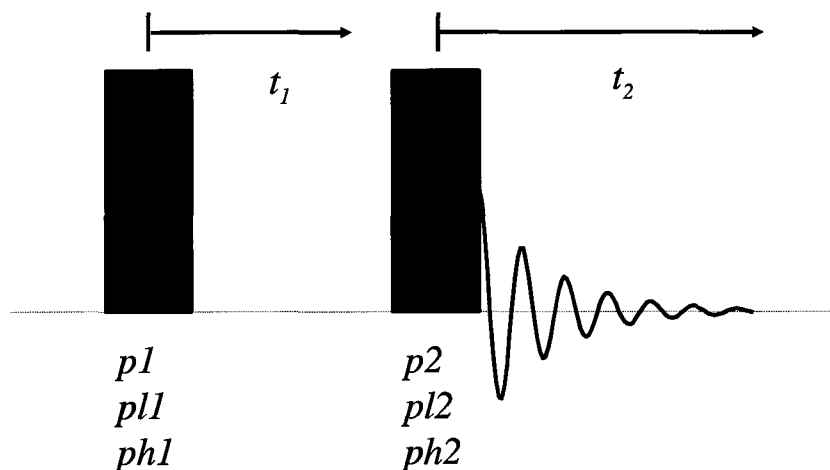


FIG. 2.8: Block schematic for two dimensional NMR experiment. Fourier transforms are performed for direct and indirect dimensions t_2 and t_1 respectively.

experiments is to remove this anisotropy, either during acquisition or processing, by a phase factor:

$$e^{-ik\omega_{-1}t_1} \quad (2.137)$$

where k is dependent on spin number and the multiple quantum transitions of the evolution period. This process creates high resolution in the indirect dimension. Since the inception of 2D experiments some forty years ago, several methods have been developed for creating phase sensitive, pure absorption two dimensional spectra. Attention here is restricted to the method of States et al [24]. The fact that special methods are required may be understood from the conventional two

dimensional transform. If the time domain signal is:

$$S(t_1, t_2) = S_r(t_1, t_2) + S_i(t_1, t_2) \quad (2.138)$$

then blindly transforming with respect to two time variables produces:

$$S(\omega_1, \omega_2) = S_0[a_1(\omega_1) + id_1(\omega_1)][a_2(\omega_2) + id_2(\omega_2)] \quad (2.139)$$

or

$$S_0\{[a_1(\omega_1)a_2(\omega_2) - d_1(\omega_1)d_2(\omega_2)] + i[a_1(\omega_1)d_2(\omega_2) + d_1(\omega_1)a_2(\omega_2)]\} \quad (2.140)$$

The absorptive $a(\omega)$ and dispersive $d(\omega)$ components cannot be considered separately. The States method essentially gathers dual CTP's, with model signal:

$$S_X(t_1, t_2) = S_0[e^{i\omega_p t_1} + e^{i\omega_{-p} t_1}]e^{-R_1 t_1}e^{(i\omega_{-1} - R_2)t_2} \quad (2.141)$$

These dual pathways, referred to as the echo and anti-echo, have different efficiencies. A z-filter [41] is employed to ensure the recombination of the pathways with equal amplitude. This step converts both pathways into zero quantum coherence populations by virtue of a pulse followed by a short delay ($\approx 10\mu s$) before a $\pi/2$ degree pulse, selective on the central transition and acquisition. Considered alone S_X has no phase sensitivity in the $t_1/F1$ dimension. The phase for the pulse before the evolution period is incremented by $\pi/2|\Delta p|$, where Δp is the change in coherence order, to produce:

$$S_Y(t_1, t_2) = S_0[e^{i\omega_p t_1} e^{i\pi/2} + e^{i\omega_{-p} t_1} e^{-i\pi/2}]e^{-R_1 t_1}e^{(i\omega_{-1} - R_2)t_2} \quad (2.142)$$

These amplitude modulated, cosine (S_X) and sin (S_Y) signals are combined to form:

$$\begin{aligned} S_+(t_1, t_2) &= S_X(t_1, t_2) + iS_Y(t_1, t_2) \\ S_-(t_1, t_2) &= S_X(t_1, t_2) - iS_Y(t_1, t_2) \end{aligned} \quad (2.143)$$

After Fourier transformation with respect to t_2 , and performing a shearing transformation, there remains:

$$S_+(t_1, \omega_2) = 2S_0 e^{i(k\omega_{-1} + \omega_p) - R_1} t_1 [a_2(\omega_2) + id(\omega_2)] \quad (2.144)$$

$$S_-(t_1, \omega_2) = 2S_0 e^{i(-k\omega_{-1} + \omega_{-p}) - R_1} t_1 [a_2(\omega_2) + id_2(\omega_2)] \quad (2.145)$$

Fourier transformation with respect to t_1 gives two expressions for the complex signal in two frequency dimensions, with opposite frequency sign. Addition of both after sign reversal in one expression leaves:

$$S(\omega_1, \omega_2) = 4S_0 \frac{R_1}{[\omega_1 - (\omega_{-p} + k\omega_2)/(1 + |k|)]^2 + R_1^2} [a_2(\omega_2) + id_2(\omega_2)] \quad (2.146)$$

whose real component is an absorption lineshape. This brief survey has given the important aspects of data acquisition, and information is subsequently extracted through lineshape simulation and analysis procedures. The preparation of raw data for these purposes is carried out via data processing, and a brief discussion of the computational aspects is given in appendix B.

2.4.4 Lineshape Simulation

Simulating experimental spectra has become a routine task in the last decade due the availability of software packages such as SIMPSON [53] and GAMMA [75].

Essentially, the time evolution of the density operator is solved using matrix manipulations. These calculations can take into account radio frequency pulse powers, durations, inter pulse spacings, expected NMR parameters among other variables and provides a system response. However in solid state NMR it is often the case that chemical environments take on a continuum of values and lineshapes are largely indistinct; density matrix calculations of powdered lineshapes then becomes impractical. To begin with, one may model the contribution of a dipole interaction broadened, unique chemical environment as either absorption Lorentzian:

$$F(\omega) = \frac{\lambda}{\lambda^2 + (\omega - \omega_0)^2}, \quad (2.147)$$

or Gaussian:

$$F(\omega) = \frac{1}{\sqrt{2\pi}\sigma} e^{\left(\frac{-(\omega-\omega_0)^2}{2\sigma^2}\right)} \quad (2.148)$$

where λ and σ are the Lorentzian and Gaussian broadening respectively. It is assumed that the equally probable crystal orientations within a powder have been equally irradiated. These ideal conditions give rise to ‘powder patterns’, distinctive NMR lineshapes which are essentially a histogram of all the orientation (specified by azimuthal and polar angles α, β) dependent frequencies. Expressed more succinctly, the spectra spectra may be considered as a sum, the powder average:

$$\bar{F}(\omega) = \frac{\sum_i^N w_i F_i(\alpha, \beta)}{\sum_i^N w_i} \quad (2.149)$$

Hodgkinson and Emsley [63] list various schemes for performing the computational task, table 2.2

In the Planar grid or Alderman-Solum-Grant scheme [22], as well as for the Spherical grid method, α and β are varied independently with N_α and N_β steps

TABLE 2.2: Powder averaging schemes

	α	β	w_j
Planar Grid	$\frac{2\pi k}{N_\alpha}$	$\frac{\pi(j+0.5)}{N_\beta}$	$\sin(\beta_j)$
Spherical Grid	$\frac{2\pi k}{N_\alpha}$	$\arccos\left(1 - \frac{2j+1}{N_\beta}\right)$	1
Planar ZCW	$\frac{2\pi(jM \bmod N)}{N}$	$\frac{(j+0.5)\pi}{N}$	$\sin(\beta_j)$
Spherical ZCW	$\frac{2\pi(jM \bmod N)}{N}$	$\arccos\left(1 - \frac{2j+1}{N}\right)$	1

and $k = 0 \dots N_\alpha - 1$, $j = 0 \dots N_\beta - 1$. For the Zaremba-Conroy-Wolfsberg method [92], N and M are chosen to satisfy $M = F(m)$ and $N = F(m + 2)$, with $F(m)$ the m th Fibonacci number. The latter method has been employed for the simulations in this thesis, and is anticipated to be optimal for fast MAS and few crystallite contributions [63]. Figure 2.11 is a simulated spectra for ^{45}Sc at 17.6T, of the three chemical sites in scandium sulfate. While the overlap is not severe, it does serve to illustrate the need for two dimensional experiments.

Depending on the nature of the experiment performed, a two dimensional spectrum can be simulated by extending the methods described briefly here. For example, using the second order perturbation theory expression for multiple quantum transition frequencies,

$$\omega_{r,c}^{(2)\text{fast MAS}} = \omega_{r,c}^{(2)\text{iso}} - \frac{r-c}{2\omega_0} \Omega_Q^2 \{A^{(0)}(I, r, c)B_{0,0}(\eta) + A^{(4)}(I, r, c)[B_{4,0}(\eta)d_{0,0}^{(4)}(\beta) + 2B_{4,2}(\eta)d_{2,0}^{(4)}(\beta) \cos 2\alpha + 2B_{4,4}(\eta)d_{4,0}^{(4)}(\beta) \cos 4\alpha]P_4(\cos \theta_m)\}, \quad (2.150)$$

one may simulate the general 2D correlation spectrum between the $r \leftrightarrow c$ quantum transition (indirect frequency dimension) and central transition (direct frequency

dimension) as:

$$F(\omega_1, \omega_2) = \frac{\lambda_1}{\lambda_1^2 + (\omega_1 - \omega_{r,c})^2} \frac{\lambda_2}{\lambda_2^2 + (\omega_2 - \omega_{1/2,-1/2})^2} \quad (2.151)$$

It should be emphasized that this assumes ideal excitation conditions and experimental lineshapes often deviate from this ideal. Also, the Gaussian lineshape often proves a more suitable candidate where spectra are devoid of characteristic Lorentzian tails. Figure 2.12 is an example of a simulated 2D spectrum for the MQMAS experiment conducted on scandium sulfate, acquired at 17.6T.

The simulation using a 2D Gaussian required 331×41 frequency grid points, and using 633 powder angles for each of the three sites, is executed in several seconds using compiled C code (listed in appendix C) on a G5 platform. The broadening (here, 30 Hz) is inversely proportional to the rate of convergence. For a lower factor, many more angles are required even in the spherical ZCW method. Using a shear factor which eliminates anisotropy in the indirect dimension, high resolution is clearly achieved for this simple crystalline material. However it is conceivable that where distributions exist in NMR parameters, overlap will still occur in the indirect dimension and thus one is led to consider means whereby single interactions may be resolved.

2.4.5 Enhanced Resolution in Disordered Systems

In the last decade quadrupolar nuclei have been made more accessible through two dimensional techniques, such as Triple Quantum Magic Angle Spinning or 3Q-MAS [6, 19, 65]. Essentially, a resolution spectrum is created in an indirect dimension by correlating the symmetric triple quantum transition frequencies with the central transition in the direct dimension. Improvements in efficiency come

in several forms [90, 91, 65], and various review articles exist in the literature for MQMAS [60].

More recently, Gan proposed Satellite Transition Magic Angle Spinning or STMAS. [37]. In this approach, coherences which have evolved over non-symmetric satellite pathways are correlated with the central transition. STMAS has better efficiency than MQMAS, but requires precise setting of the magic angle in order to eliminate effects of first order quadrupolar broadening. Also, the spectra may be obscured by the central transition (CT) and outer satellite transitions [76]. Gan suggested a means for the suppression of the CT and outer satellites using a double quantum (DQ) filter [85], based on the COSY sequence [36]. One correlates single or double quantum transitions with the CT, and diagonal peaks are removed from the spectrum. Figure 2.13 is a double quantum filtered STMAS spectrum acquired for rubidium nitrate at 17.6T. The first order quadrupole interaction is present for satellite transitions; the high resolution of the indirect dimension for this experiment relies on the magic angle being accurately set. Disordered systems such as complex perovskites offer a richness of structural detail which often precludes straight forward interpretation of MAS and MQMAS spectra [43, 78, 35, 17]. Distributions in quadrupole parameters and the chemical shift enormously complicate the tasks of spectral assignment and interpretation. The second order, perturbation theory expression for multiple quantum transition frequencies (equation 2.151) suggests the need to acquire a further frequency dimension in order to completely separate the three interactions. This original idea was communicated to the author by Donghua Zhou, June 2004. Based upon the recent success and high efficiency of the DQF-STMAS experiment, one approach would be to convert double to triple quantum coherence. A second evolution period under the symmetric triple quantum coherence provides additional frequency information. Without

loss of generality, the frequency expressions for the central transition, and multiple quantum transitions p and q may be summarized as:

$$\begin{pmatrix} a_{11} & a_{12} & a_{13} \\ a_{21} & a_{22} & a_{23} \\ a_{31} & a_{32} & a_{33} \end{pmatrix} \begin{pmatrix} \delta_{iso}^{CS} \\ \delta_{iso}^{2Q} \\ \delta_{aniso}^{2Q} \end{pmatrix} = \begin{pmatrix} \omega_{-1} \\ \omega_p \\ \omega_q \end{pmatrix} \quad (2.152)$$

Here,

$$\delta_{iso}^{CS} = -\frac{\omega_{r,c}^{(iso)}}{\omega_0}; \quad (2.153)$$

$$\delta_{iso}^{2Q} = -\frac{\Omega_Q^2}{2\omega_0^2} B_{0,0}(\eta) = -\frac{(\eta^2 + 3)}{10\omega_0^2} \left[\frac{e^2 q Q}{2I(2I-1)\hbar} \right]^2 \quad (2.154)$$

$$\delta_{aniso}^{2Q} = \frac{2\omega_Q^2}{\omega_0^2} F(\alpha, \beta) \quad (2.155)$$

with

$$\begin{aligned} F(\alpha, \beta) = & \frac{1}{11520} [(-54 - 3\eta^2 + 60\eta \cos 2\alpha - 35\eta^2 \cos 4\alpha) \\ & + (540 + 30\eta^2 - 480\eta \cos 2\alpha + 70\eta^2 \cos 4\alpha) \cos^2 \beta \\ & (-630 - 35\eta^2 + 420\eta \cos 2\alpha - 35\eta^2 \cos 4\alpha) \cos^4 \beta] \end{aligned} \quad (2.156)$$

Now $a_{11} = 1$ and $a_{21} = a_{31} = (r - c)$. The remainder of the matrix elements depend upon the Clebsch-Gordon co-efficients. Matrix equation 2.153 may be solved to yield:

$$\begin{pmatrix} \delta_{iso}^{CS} \\ \delta_{iso}^{2Q} \\ \delta_{aniso}^{2Q} \end{pmatrix} = \frac{1}{\Delta} A_{ij}^T \begin{pmatrix} \omega_{-1} \\ \omega_p \\ \omega_q \end{pmatrix} \quad (2.157)$$

where A_{ij} is the transpose of the matrix of coefficients and the determinant is

given by:

$$\Delta = a_{11}a_{22}a_{33} + a_{12}a_{23}a_{31} + a_{13}a_{21}a_{32} - a_{11}a_{23}a_{32} - a_{12}a_{21}a_{33} - a_{13}a_{22}a_{31} \quad (2.158)$$

Consider figure 2.14, a representation of a three dimensional pulse sequence. Times t_1 and t_2 for indirect dimensions $F1$ and $F2$ are incremented and acquisition occurs during t_3 . Pulse block one creates double quantum coherences, whilst pulse block two converts double to triple quantum coherence. In hyper-complex detection, pulse five and delay 1 comprise the z-filter step, with detection after pulse six. In addition, phases corresponding pulses before the evolution periods are incremented by $\pi/|2\Delta p|$ to create the cosine and sine amplitude modulated components for phase sensitivity in the indirect dimension(s). The coherence transfer pathway is $\pm 2 \rightarrow \pm 1 \rightarrow \mp 3 \rightarrow 0 \rightarrow -1$. The system responses in the time domain are:

$$S_{xx}(t_1, t_2, t_3) = S_0[e^{i\omega_{-p}t_1} + e^{i\omega_p t_1}]e^{-R_1 t_1}[e^{i\omega_{-q}t_2} + e^{i\omega_q t_2}]e^{-R_2 t_2}e^{(i\omega_{-1}-R_3)t_3} \quad (2.159)$$

$$S_{yx}(t_1, t_2, t_3) = S_0[e^{i(\omega_{-p}t_1+\pi/2)} + e^{i(\omega_p t_1-\pi/2)}]e^{-R_1 t_1}[e^{i\omega_{-q}t_2} + e^{i\omega_q t_2}]e^{-R_2 t_2}e^{(i\omega_{-1}-R_3)t_3} \quad (2.160)$$

$$S_{xy}(t_1, t_2, t_3) = S_0[e^{i\omega_{-p}t_1} + e^{i\omega_p t_1}]e^{-R_1 t_1}[e^{i(\omega_{-q}t_2+\pi/2)} + e^{i(\omega_q t_2-\pi/2)}]e^{-R_2 t_2}e^{(i\omega_{-1}-R_3)t_3} \quad (2.161)$$

$$S_{yy}(t_1, t_2, t_3) = S_0[e^{i(\omega_{-p}t_1+\pi/2)} + e^{i(\omega_p t_1-\pi/2)}]e^{-R_1 t_1}[e^{i(\omega_{-q}t_2+\pi/2)} + e^{i(\omega_q t_2+\pi/2)}]e^{-R_2 t_2} \\ \times e^{(i\omega_{-1}-R_3)t_3} \quad (2.162)$$

where R_1, R_2 and R_3 are the phenomenological relaxation rates. One may con-

struct echo and anti-echo signals in the usual manner, with respect to t_2 :

$$S_{x+} = S_{xx} + iS_{xy} = 2S_0[e^{i\omega_{-p}t_1} + e^{i\omega_p t_1}]e^{-R_1 t_1} e^{i\omega_q t_2 - R_2 t_2} e^{(i\omega_{-1} - R_3)t_3} \quad (2.163)$$

$$S_{y+} = S_{yx} + iS_{yy} = 2S_0[e^{i(\omega_{-p}t_1 + \pi/2)} + e^{i(\omega_p t_1 - \pi/2)}]e^{-R_1 t_1} e^{i\omega_q t_2 - R_2 t_2} e^{(i\omega_{-1} - R_3)t_3} \quad (2.164)$$

$$S_{x-} = S_{xx} - iS_{xy} = 2S_0[e^{i\omega_{-p}t_1} + e^{i\omega_p t_1}]e^{-R_1 t_1} e^{i\omega_{-q} t_2 - R_2 t_2} e^{(i\omega_{-1} - R_3)t_3} \quad (2.165)$$

$$S_{y-} = S_{yx} - iS_{yy} = 2S_0[e^{i(\omega_{-p}t_1 + \pi/2)} + e^{i(\omega_p t_1 - \pi/2)}]e^{-R_1 t_1} e^{i\omega_{-q} t_2 - R_2 t_2} e^{(i\omega_{-1} - R_3)t_3} \quad (2.166)$$

After Fourier transformation with respect to t_3 , a shearing transformation is introduced to remove anisotropy in the indirect dimension. We leave the exact form of the transformation ambiguous at this stage, and simply refer to the shearing factor in dimension F_2 as k_2 :

$$S_{x+} = 2S_0[e^{i\omega_{-p}t_1} + e^{i\omega_p t_1}]e^{-R_1 t_1} e^{[i(\omega_q + k_2\omega_{-1}) - R_2]t_2} [a(\omega_{-1}) + id(\omega_{-1})] \quad (2.167)$$

$$S_{y+} = 2S_0[e^{i(\omega_{-p}t_1 + \pi/2)} + e^{i(\omega_p t_1 - \pi/2)}]e^{-R_1 t_1} e^{[i(\omega_q + k_2\omega_{-1}) - R_2]t_2} [a(\omega_{-1}) + id(\omega_{-1})] \quad (2.168)$$

$$S_{x-} = 2S_0[e^{i\omega_{-p}t_1} + e^{i\omega_p t_1}]e^{-R_1 t_1} e^{[i(\omega_{-q} - k_2\omega_{-1}) - R_2]t_2} [a(\omega_{-1}) + id(\omega_{-1})] \quad (2.169)$$

$$S_{y-} = 2S_0[e^{i(\omega_{-p}t_1 + \pi/2)} + e^{i(\omega_p t_1 - \pi/2)}]e^{-R_1 t_1} e^{[i(\omega_{-q} - k_2\omega_{-1}) - R_2]t_2} [a(\omega_{-1}) + id(\omega_{-1})] \quad (2.170)$$

where $a(\omega)$ and $d(\omega)$ are the absorption and dispersion Lorentzian lines in F_3 . A Fourier transform is then performed with respect to t_2 , the sign for ω_2 is reversed

and the echo and anti-echo pathways are then co-added:

$$S_x(t_1, \omega_2, \omega_{-1}) = 4S_0 [e^{i\omega_{-p}t_1} + e^{i\omega_p t_1}] e^{-R_1 t_1} \frac{R_2}{[\omega_2 - (\omega_{-p} - k_2 \omega_{-1})]^2 + R_2^2} \times [a(\omega_{-1}) + d(\omega_{-1})] \quad (2.171)$$

$$S_y(t_1, \omega_2, \omega_{-1}) = 4S_0 [e^{i(\omega_{-p}t_1 + \pi/2)} + e^{i(\omega_p t_1 + \pi/2)}] e^{-R_1 t_1} \frac{R_2}{[\omega_2 - (\omega_{-p} - k_2 \omega_{-1})]^2 + R_2^2} \times [a(\omega_{-1}) + d(\omega_{-1})] \quad (2.172)$$

Proceeding as before, echo and anti-echo pathways are reconstructed and a shearing transformation is applied along $F1$, with factor k_1 ;

$$S_+(t_1, \omega_2, \omega_{-1}) = 4S_0 e^{[i(\omega_p + k_1(\omega_p + k_2 \omega_{-1})) - R_1]t_1} \frac{R_2}{[\omega_2 - (\omega_{-q} - k_2 \omega_{-1})]^2 + R_2^2} \times [a(\omega_{-1}) + id(\omega_{-1})] \quad (2.173)$$

$$S_-(t_1, \omega_2, \omega_{-1}) = 4S_0 e^{[i(\omega_{-p} - k_1(\omega_p + k_2 \omega_{-1})) - R_1]t_1} \frac{R_2}{[\omega_2 - (\omega_{-q} - k_2 \omega_{-1})]^2 + R_2^2} \times [a(\omega_{-1}) + id(\omega_{-1})] \quad (2.174)$$

Finally, after Fourier transformation, sign-reversal of ω_1 and co-adding pathways;

$$S(\omega_1, \omega_2, \omega_{-1}) = 8S_0 \frac{R_1}{[\omega_1 - (\omega_{-p} - k_1(\omega_p + k_2 \omega_{-1}))]^2 + R_1^2} \times \frac{R_2}{[\omega_2 - (\omega_{-q} - k_2 \omega_{-1})]^2 + R_2^2} [a(\omega_{-1}) + id(\omega_{-1})] \quad (2.175)$$

By comparison with equation 2.158, one anticipates that the calculated choice of shearing factors may allow the isolation of different interactions along $F1$. The coefficient matrices for the central transition (first row), double (second row,

$-3/2 \leftrightarrow 1/2$) and triple (third row, $-3/2 \leftrightarrow 3/2$) quantum coherences are:

$$I = 3/2; \begin{pmatrix} 1 & -1 & 54 \\ \mp 2 & \mp 3 & \mp 6 \\ \mp 3 & \mp 9 & \pm 42 \end{pmatrix} \quad (2.176)$$

$$I = 5/2; \begin{pmatrix} 1 & -8 & 144 \\ \mp 2 & \pm 7 & \mp 186 \\ \mp 3 & \pm 6 & \mp 228 \end{pmatrix} \quad (2.177)$$

$$I = 7/2; \begin{pmatrix} 1 & -15 & 270 \\ \mp 2 & \pm 21 & \mp 438 \\ \mp 3 & \mp 27 & \pm 606 \end{pmatrix} \quad (2.178)$$

$$I = 9/2; \begin{pmatrix} 1 & -24 & 432 \\ \mp 2 & \pm 39 & \mp 762 \\ \mp 3 & \pm 54 & \mp 1092 \end{pmatrix} \quad (2.179)$$

However, the determinant in all cases is zero, therefore multiple quantum frequencies are not linearly independent. There is no number of dimensions or shearing transformations which will allow for the isolation of a single interaction, under these assumptions. It is anticipated that the reintroduction of (for instance) second rank tensor terms, or where applicable third order quadrupole effects, may lift the degeneracy and allow for complete resolution of frequency expressions. This experiment does represent a likely next step in the evolution of NMR technique as applied to the solid state. Most germane to disordered materials (studied in this work), higher resolution will bring significant gains in the understanding of local microscopic properties.

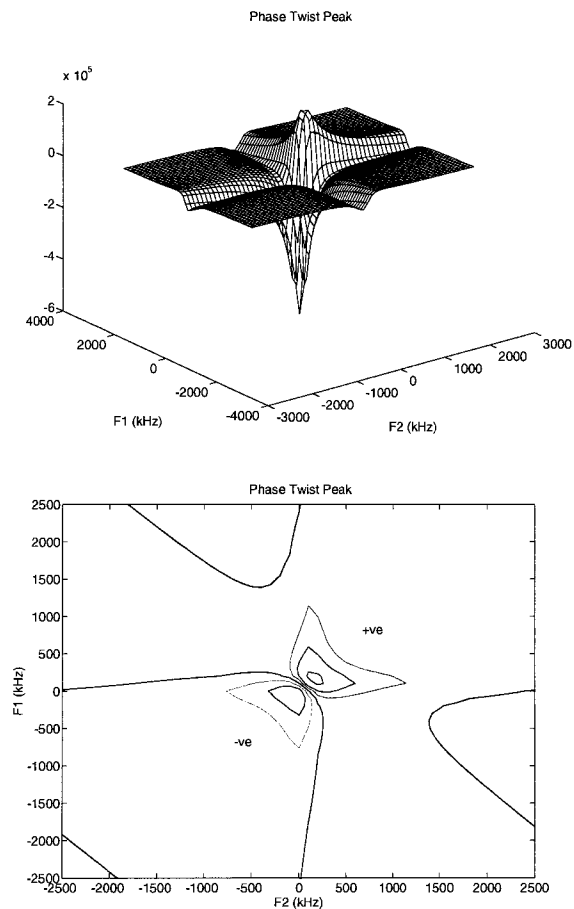


FIG. 2.9: Phase twist peaks in the real component of the 2D FFT of the Lorentzian $\exp(-0.6 + i)x \exp(-0.6 + i)y$; x and y are two independent time variables and it is assumed that the dwell time was 0.2 ms i.e., a frequency sweep-width of ± 2500 Hz

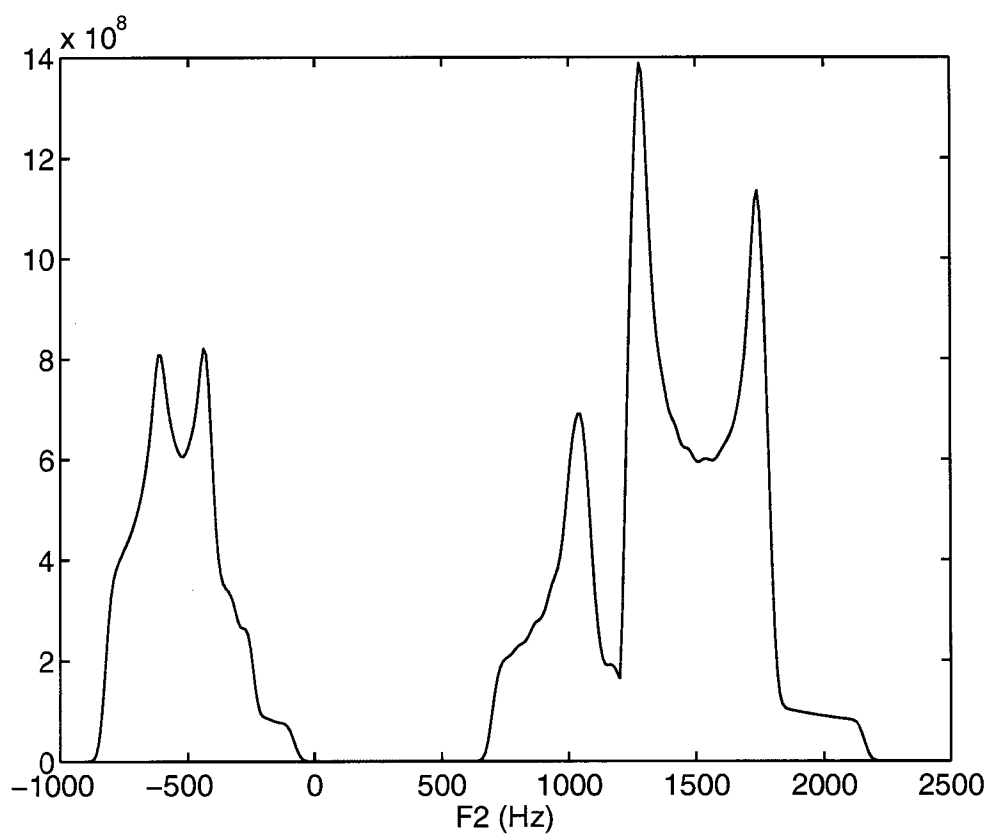


FIG. 2.10: Simulated powder pattern for the three distinct chemical sites in scandium sulfate, for ^{45}Sc MAS at 17.6T

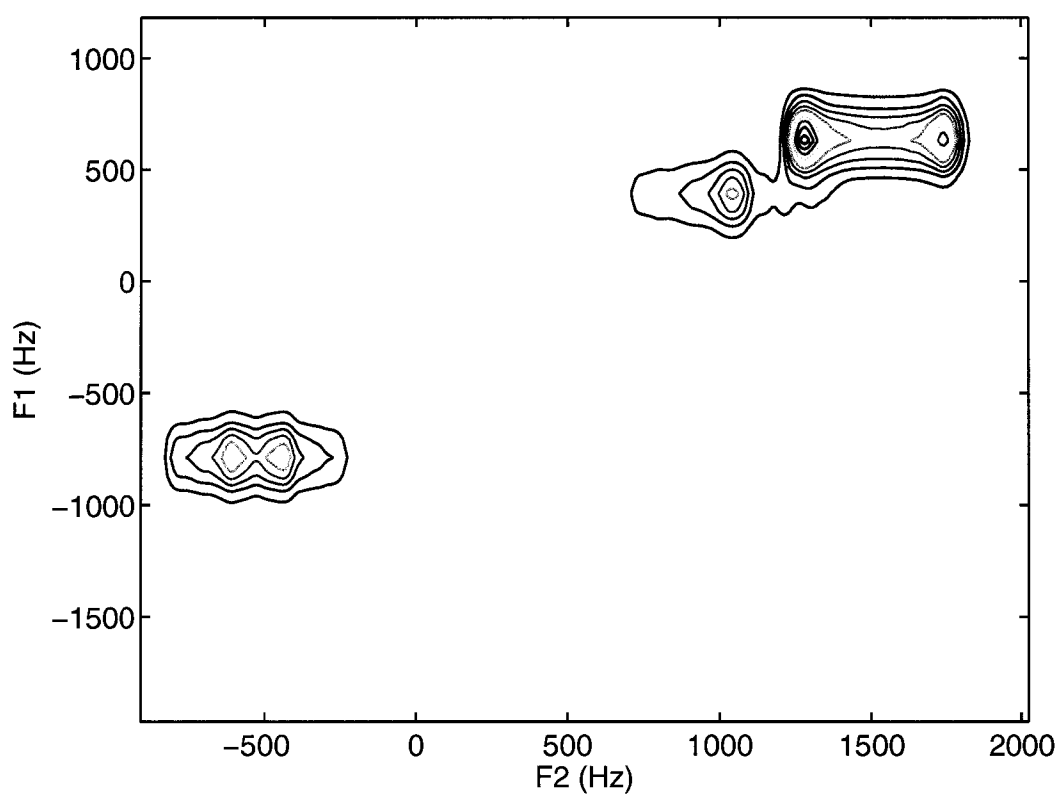


FIG. 2.11: Simulated spectrum for scandium sulfate, ^{45}Sc 3QMAS at 17.6T. The number of frequency grid points is 331×41 ($F2 \times F1$), 633 powder increments for each site, 30 Hz line broadening. Left to right, site parameters for chemical shift are -6.1, 2.4 and 4.5 ppm, with respect to Scandium Chloride reference. Quadrupole coupling constants C_Q are 4.6, 4.2 and 5.5 MHz, and asymmetry parameter η 0.5, 0.9, 0.1

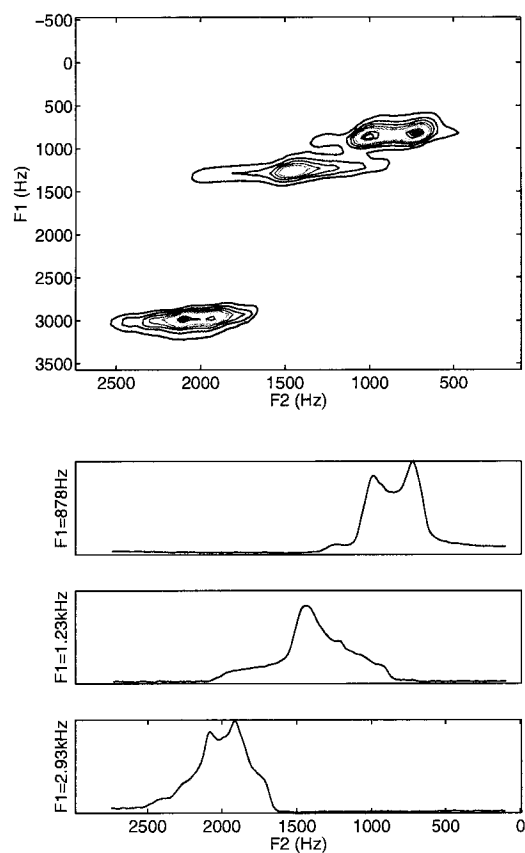


FIG. 2.12: (Top) ^{87}Rb Double Quantum Filtered STMAS at 17.6T and 15 kHz spinning speed. (Bottom) 1D Slices, parallel to F2, taken through frequencies as indicated in F1, corresponding to distinct chemical sites.

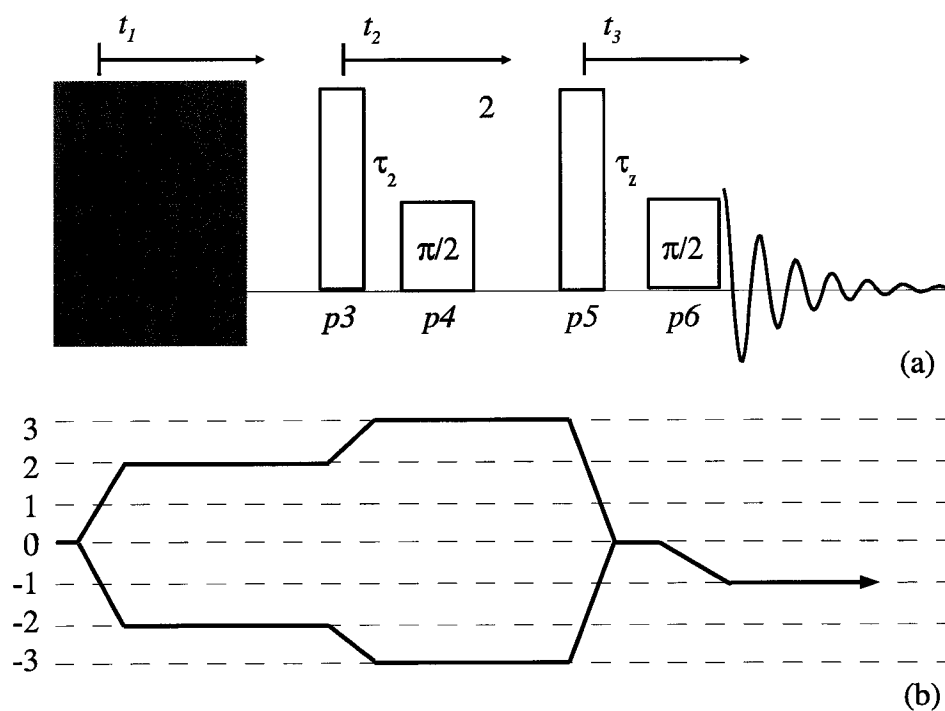


FIG. 2.13: (a) Proposed three dimensional multiple quantum MAS experiment. Pulse block 1 represents a double quantum filter and pulse block 2 a triple quantum filter. Pulse five and delay τ_z comprise the z-filter, with a selective 90 degree pulse for detection. (b) Coherence transfer pathway for 3D-MQMAS

Chapter 3

Ferroelectric Materials

3.1 Crystal Chemistry

The materials studied in this thesis belong to the larger class of ferroelectrics and have the perovskite structure, named after CaTiO_3 . In the complex or doubled perovskites, we focus consideration to substitution on the A or B sites in compounds with general formula:



where the chemical composition of either A, B or both sites is variable; these materials are referred to as solid solutions. Local strains induced by differences in size and charge between existing and substituted atoms give rise to interesting and valuable properties. In the elastic model of the solid solution [1], the static strain is given by

$$\overline{u_{st}^2} = \gamma c \Delta R^2 \tag{3.2}$$

where c is the concentration of the substituted atom, ΔR the difference between atomic radii and γ is a factor which is lattice dependent. In addition, the thermal motion induces a dynamic shift which for a monotonic crystal is given by:

$$\overline{u_d^2} = \frac{3\hbar^2 T}{mk\theta^2} \left[\Phi(x) + \frac{x}{4} \right] \quad (3.3)$$

where m is the atomic mass, T the absolute temperature, θ the Debye characteristic temperature and $x = \frac{\theta}{T}\Phi(x)$ is the Debye function. In solid solutions of simple chemical composition, the arrangement of atoms among substitutional sites follows either statistical order or disorder. In the former, atoms are arranged in regularly alternating planes in some ratio, exhibiting sharp x-ray diffraction peaks. In the latter, atomic positions are occupied randomly, the probability of occupation dependent on concentration and overall charge neutrality. In the simple body centered cubic (BCC) structure there exists position A at the corners and B at the centers of the unit cell. In the complex perovskites studied here, substitution occurs on the B site. The species present at the site and type of ordering is dictated by the composition and the method of preparation. In the Random Site model [82] for ordering, applied successfully to a number of relaxor ferroelectric systems, one ordered site β'' is assumed to be occupied by a single species. A second site β' contains a stoichiometric mixture of atoms. The planes arising from this distribution occur in a 1:1 or 2:1 ratio, with ordering direction along [1,1,1], preserving charge neutrality.

The nature of the chemical bond in the solid solutions under study varies from largely ionic (for example B-O) to partially covalent (particularly A-O), a measure given by the differences in electronegativity. In the simplest cases, consideration of ionic size, oxidation state and overall stoichiometry can be sufficient to predict sim-

ple structures. The program Structure Prediction Software (SpuDS [56]) provides insight into the local structure of perovskites and basic solid solutions. However in general one must consider the forces of interaction between atoms, which is task carried out in Molecular Dynamics (MD) simulations. In the simplest approximation, the potential energy is considered to be the sums of all inter-particle interaction energies, or:

$$U = \frac{1}{2} \sum_{i=1}^N \sum_{k=1}^N u(r_{ik}) \quad (3.4)$$

A general form of $u(r_{ik})$ is given by:

$$u(r_{ik}) = -\frac{a}{r^m} + \frac{b}{r^n} \quad (3.5)$$

where a, b are empirically or otherwise determined. A popular example includes the Lennard-Jones or “6-12” potential for which $n = 6$ and $m = 12$. For ionic crystals, the interaction is often given by:

$$u(r) = \frac{z_1 z_2 e^2}{r} + \frac{b}{r^n} \quad (3.6)$$

The first term is the usual point charge electrostatic interaction, and the second arises from the repulsion of inner electron shells. A summation carried out over the lattice is slowly convergent, particularly for sums proportional to $1/r$. Methods are used to produce converged values (eg., Ewald [48] or Bertaut [47] Summation) and the coefficient so produced from the first term in equation 3.6 is referred to as the Madelung constant. It gives an indication of the structural type, for instance, Rock Salt (NaCl) type materials have a Madelung constant of 1.75.

Ab-initio methods are the most fundamental and rigorous of calculations, usually concerned with electronic structure. Solutions are sought for Schrodinger’s

equation based on assumptions of the form of the potential energy and solutions. Two original approximations, Orthogonal Plane Waves (OPW) and Augmented Plane Waves (APW) [57] form the basis of modern Density Functional Theory (DFT) [87] and the Projector Augmented-Wave (PAW) [9] method. However, since Slater's work in the 1930's and 40's, the range and applicability of first-principle calculations have extended well beyond band structure. As a byproduct of these calculations, electric field gradients [54, 66] and chemical shifts [45, 44] are readily available for systems which are well ordered and involve small to medium sized atoms.

3.2 Ferroelectrics

Ferroelectrics are compounds with large, reversible polarizations. This hysteresis effect has both electronic and ionic origins. Within these systems there exist microscopic regions of uniform polarization which are referred to as domains [30, 14].

The effect of polarization on elastic, thermal and optical properties is quite significant [30]. Ferroelectrics are used in (for example) transducers where an environmental variable such as pressure is converted into a voltage signal. This exploits the often associated property of piezoelectricity; the existence of an electric field due to a physical stress on the crystal and vice versa. Different crystalline structures are observed in separate temperature regions delimited by transition points. Around a transition, there is an anomaly in the dielectric constant. Above a specific temperature (Curie), macroscopic polarization ceases to exist due to the thermal motion of ions, sufficient to disorder or displace domains. Ferroelectrics may be classified according to;

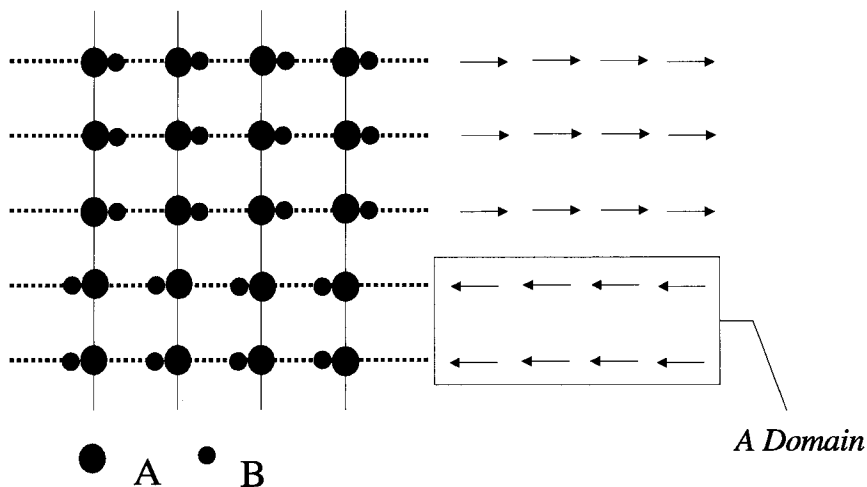


FIG. 3.1: Simple model of microscopic domains in two dimensions, through displaced A anions and B cations.

1. Chemical nature, eg., hydrogen-bonded crystals or double oxides.
2. Number of directions for spontaneous Polarization, either single or multiple.
3. Lack or existence of center of symmetry in the non-polar phase, which implies the presence or absence of piezoelectricity
4. Nature of phase change at the Curie Point, which may be of the displacive or order/disorder variety.

A large group of ferroelectrics have the doubled Perovskite structure mentioned previously; they are centro-symmetric above Curie Point. Within this group

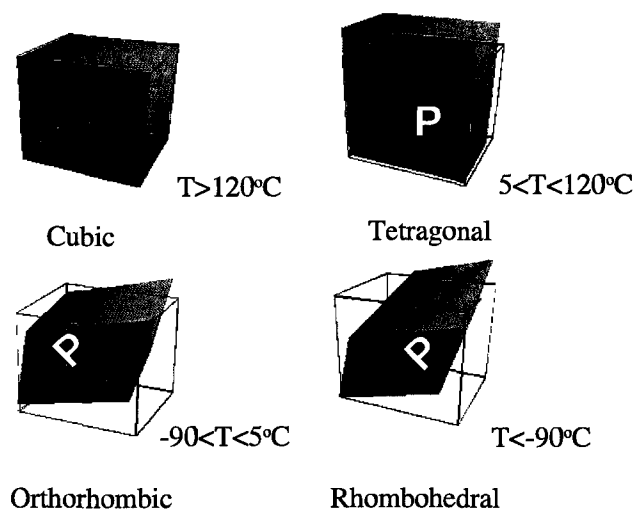


FIG. 3.2: The four phases of ferroelectric Barium Titanate. The phase transitions occur over narrow temperature ranges, in distinction to the relaxor ferroelectrics. All ferroelectrics are distinguished by the absence of polarization above the Curie temperature.

are the relaxors which display large dielectric susceptibility and a very broad Curie transition region [15, 14]. Macroscopic properties such as dielectric and magnetic behavior are typically contingent on B site cation order [82, 52] where electrostatic interactions between different B site atoms are important. Lead Scandium Tantalate $\text{Pb}_2\text{Sc}_{1/2}\text{Ta}_{1/2}\text{O}_3$ (PST) [86] is a doubled perovskite which may display both normal and relaxor ferroelectric behavior. Owing to the charge (Sc^{3+} , Ta^{5+}) of the B sites, neutrality is preserved by assuming a 1:1 order of Sc/Ta. When chemically ordered, this material does not display relaxor behavior, but does oth-

erwise. [86, 62, 28] Besides the influence of B site order, there is evidence also to suggest that the covalency between A site and oxygen ions is a significant factor in determining long range order [50, 39], and thus the existence or absence of relaxor behavior. The direction and magnitude of the A site displacement also largely determines the polarization. [30]. For lead A site ions in particular, lone pair electrons outside a closed d shell promote this displacement and tend to shorten Pb-O bonds. Lead is a popular candidate for materials, although growing concern over environmental impact is motivating the search for substitutes [25]. The tungstate Relaxor ferroelectric $\text{Pb}(\text{Sc}_{2/3}\text{W}_{1/3})\text{O}_3$ (PSW) has the doubled-perovskite structure with layers of pure Scandium (Sc^{3+}) interleaved between layers containing a random mixture (hence ‘random sites’) of Sc^{3+} and Tungsten (W^{6+}) [64]. The layers for the Pb based mixed-metal structures are distributed throughout the crystal matrix in a 1:1 ratio. Overall the material has a 2:1 B site cation stoichiometry. The ordering within similar materials is well explained in terms of simple electrostatics [51] and ab-initio methods provide confirmation [58]. It is observed that in forming solid solutions of such compounds, small changes in the random site chemistry produce significant change in overall macroscopic behavior. Iniguez et al [42] performed first-principle studies of solid solution $(\text{BiSc}_3)_{(1-x)}-(\text{PbTi})\text{O}_3)_3$ or BS-PT and found large structural distortions and polarizations at the morphotropic phase boundary.

In addition, hybridization between the A site atoms and oxygen are considered directly related the piezoelectric and ferroelectric properties. The attractive features of solid solutions motivates the present study of $(1-x)\text{Pb}(\text{Sc}_{2/3}\text{W}_{1/3})\text{O}_3 - (x)\text{PbTiO}_3$ (PSW-PT) and $(1-x)\text{Pb}(\text{Sc}_{2/3}\text{W}_{1/3})\text{O}_3 - (x)\text{PbZrO}_3$ (PSW-PZ). These were prepared via the columbite route at the University of Pennsylvania where they were also characterized using x-ray, electron diffraction as well as Transmis-

sion Electron Microscopy [64]. PSW-PT shows a higher degree of ordering. That is, planes of pure and mixed cations persist throughout the crystal matrix in the 1:1 ratio for concentrations as high as $x \approx 0.35$. This is in contrast with PSW-PZ where order persists until $x \approx 0.2$. One of the ordered positions (β'') is assumed to be occupied exclusively by Sc^{3+} . Substitution of Ti^{4+} or Zr^{4+} occurs on the random site position (β') which for all concentrations has a mixture of cations. Given these assumptions and the overall requirement of charge neutrality, one has for the stoichiometry for $0 \leq x \leq 0.25$; where M^{4+} may be either Ti^{4+} or Zr^{4+} . Depletion of Sc at $x = 0.25$ leads to substitution on both ordered sites after this point and the stoichiometry for $0.25 < x \leq 1.0$; The real component of the permittivity as a function of both frequency and temperature shows a marked increase with concentration x , particularly for PSW-PZ. The Curie transition point is more disperse for the Zr containing solutions also and increases in an almost linear fashion, in distinction to the Ti based solutions. It is anticipated that both solid solutions will contain significant distributions of all NMR parameters. In order to interpret experimental spectra, it is necessary to understand the relationship between local ionic ordering, resulting NMR parameter distributions and NMR lineshapes.

Chapter 4

Calculations

4.1 Simulating the ionic lattice

As mentioned previously first-principles calculations, while accurate and growing in the range of applicability, have difficulty in taking into account the effects of disorder. One reason is the often underlying assumption of periodic boundary conditions in order to model the potential and thus solve a modified form of Schrodinger's equation. The intention here is to develop simple methods based upon a point charge approximation, which permit the relationship to be established between local chemical and structural order, and NMR lineshapes. While electric field gradient calculations based on this assumption are well established [13, 47], an attempt will also be made to model the effects of disorder on manifolds of isotropic chemical shifts. To begin with, it is necessary to establish the nature of realistic distortions within perovskites. The program SPuDS (Structure Prediction Diagnostic Software) [56] provides useful insight into the distortions within simple perovskites and their solid solutions. The program takes into account oxidation

states, ionic size, bond valences and minimizes a global instability index (GII) for the space group structure specified, by tilting oxygen octahedra. Octahedra maintain individual symmetry (there are no local bond distortions apart from B-site off centering) and permitted tilts are largely dictated by the space group symmetry and ionic size. [89, 12]

TABLE 4.1: Summary of results at room temperature for SPuDS calculations.

Property	PbTiO₃	PbZrO₃	[4]PST(o)	PST(d)
Group/Tilt	Imma/ $a^0b^-b^-$	Imma/ $a^0b^-b^-$	R-3/ $a^-a^-a^-$	R-3/ $a^-a^-a^-$
Tilt (deg.)	0	12.06	-8.74	-15.74
GII	0.13	0.006	0.00001	0.15
Cell Vol./Z A ³	242.8	274.6	133.77	415.0
Pb-O (Å)	2.78	2.9 ± 0.3	2.87 ± 0.2	2.9 ± 0.4
B-O (Å)	1.96	2.07	Sc:2.1,Ta:1.9	2.1
B-O-B (deg.)	180	166 ± 10	180	165

Table 4.1 gives a summary of results at room temperature for PbZrO₃ (PZ), PbTiO₃ (PT) and ordered (o) and disordered (d) PST. The tilt mechanism and systems will be explained in detail shortly, but important to note are the increase in bond dispersions and cell volumes between ordered and disordered versions of PST. Also, the magnitude of the tilting distortion in PZ is more significant than PT, reflected in a larger tilt angle and lower B-O-B angle. These elements are from the same period and have very similar electronegativities, so the difference in physical characteristics may be largely attributed to a difference in ionic size. It again should be noted that this is also implicit in the calculation and may only be serving to illustrate its limitations. The intention to use similar distortions to predict the characteristics of electric field gradient and chemical shift distributions in the PSW-PT and PSW-PZ solid solutions. To begin with, using the expressions given in section 3.2 for stoichiometry, one may generate the coordinates of the undistorted lattice ions using a simple prescription:

- Create coordinates for the perovskite Bravais lattice, with desired symmetry (in this case cubic).
- Associate ions with coordinates for pure layers.
- Distribute B-sites by incrementing y , then x followed by z implying that every second ion lies on the random layer for ordering of planes along $[1,1,1]$.
- Use stoichiometry of the random site layer in conjunction with random number generator to assign charges to ions.

If the number of cells per dimension in the super cell is l , then there are $(l - 1)^3$ B- site atoms, $3l(l - 1)^2$ oxygen atoms and $(l + 1)^3$ A- site (here, Pb) atoms. Table 4.2 lists structural parameters for undistorted PSW. These have been generated by this procedure, from the perspective of a central scandium ion with cubic lattice parameter a . Column one corresponds to the number of atoms per shell as radii (column 2) increases, from central B atom. Column three corresponds to the average charge per shell. Mixed and pure shells alternate; every pure shell corresponds to atoms from the β'' ordered position and mixed shells to atoms from the β' ordered position. Using the method described to assign ions, the 6 nearest B site neighbors for a scandium labeled in the sequence by i , for a lattice of dimension l^3 are given by:

$$(i - 1), (i + 1), (i - l), (i + l), (i - l^2), (i + l^2) \quad (4.1)$$

Lattice distortions for individual ions are directly related to the useful macroscopic properties and may be introduced by simple transformation of co-ordinates. The least trivial of these are the various rotations available to the oxygen octahedra. Glazer [5] gives notation whereby one may distinguish the magnitude

TABLE 4.2: Structural parameters for undistorted PSW

No. of Atoms	Shell Radii/a	Average charge (e)
6.00000	0.50000	-2.00000 (O)
8.00000	0.86603	2.00000 (Pb)
6.00000	1.00000	4.00000 (Sc/W)
24.00000	1.11803	-2.00000 (O)
12.00000	1.41421	3.00000 (Sc)
30.00000	1.50000	-2.00000 (O)
24.00000	1.65831	2.00000 (Pb)
8.00000	1.73205	5.62500 (Sc/W)
24.00000	1.80278	-2.00000 (O)
6.00000	2.00000	3.00000 (Sc)
48.00000	2.06155	-2.00000 (O)
24.00000	2.17945	2.00000 (Pb)
24.00000	2.23607	5.12500 (Sc/W)
48.00000	2.29129	-2.00000 (O)
24.00000	2.44949	3.00000 (Sc)
30.00000	2.50000	-2.00000 (O)
32.00000	2.59808	2.00000 (Pb)
72.00000	2.69258	-2.00000 (O)
12.00000	2.82843	3.00000 (Sc)

and direction of the Euler rotations about x, y and z . For instance the symbols $a^+a^+a^+$ indicate rotations of the same magnitude about each axis (symbol a) and the positive sign indicates that rotations along each axis are in phase. Figure 4.1 demonstrates the tilt system $a^0b^-b^-$ for space group symmetry $Imma$. In other words, rotations of the same magnitude occur about the y and z axes, out of phase between respective octahedra along either axis. No rotation takes place about the x axis. There is some disagreement as to the number of rotation systems which preserve the corner sharing connectivity of the oxygen without distortion. [88]

In order to introduce the effects of rotation to the simulated lattice, the ions at the vertices of the oxygen octahedra are distributed long orthogonal directions, and then adjusted according to the rotations, i.e., if the rotation matrix is represented

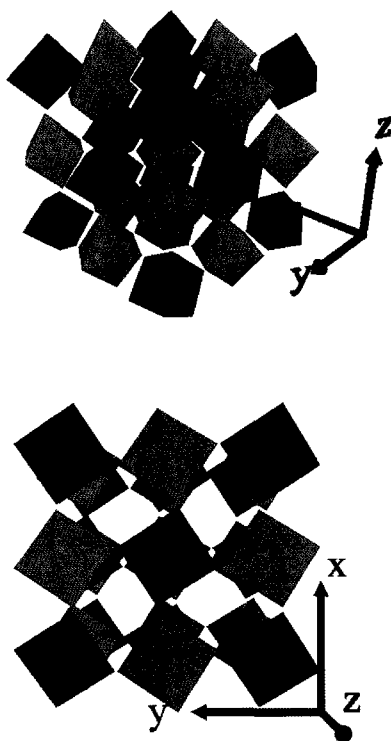


FIG. 4.1: Space group $Im\bar{m}a$, with tilt system $a^0b^-b^-$ and 1:1 order along $[1,1,1]$. Red and green octahedra illustrate the different species on the B-site.

as general 3×3 :

$$\begin{pmatrix} b_{11} & b_{12} & b_{13} \\ b_{21} & b_{22} & b_{23} \\ b_{31} & b_{32} & b_{33} \end{pmatrix} \quad (4.2)$$

then the adjustment to the orthogonal directions are:

$$\begin{aligned} \pm x' &= \pm b_{11} a/2 \\ [\pm 1, 0, 0]; \quad \pm y' &= \pm b_{21} a/2 \\ \pm z' &= \pm b_{31} a/2 \end{aligned} \quad (4.3)$$

$$\begin{aligned}
& \pm x' = \pm b_{12}a/2 \\
[0, \pm 1, 0]; & \pm y' = \pm b_{22}a/2 \\
& \pm z' = \pm b_{32}a/2
\end{aligned} \tag{4.4}$$

$$\begin{aligned}
& \pm x' = \pm b_{13}a/2 \\
[0, 0, \pm 1]; & \pm y' = \pm b_{23}a/2 \\
& \pm z' = \pm b_{33}a/2
\end{aligned} \tag{4.5}$$

For the “ x, y, z ” or pitch-roll-yaw convention, the x -rotation (yaw) is ψ , the y -rotation (pitch) is θ , z -rotation (roll) is ϕ and the matrix elements are given by:

$$\begin{aligned}
b_{11} &= \cos \theta \cos \phi \\
b_{12} &= \cos \theta \sin \phi \\
b_{13} &= -\sin \theta \\
b_{21} &= \sin \psi \sin \theta \cos \phi - \cos \psi \sin \phi \\
b_{22} &= \sin \psi \sin \theta \sin \phi + \cos \psi \cos \phi \\
b_{23} &= \cos \theta \sin \psi \\
b_{31} &= \cos \psi \cos \phi - \sin \psi \sin \phi \\
b_{32} &= \cos \psi \sin \theta \sin \phi - \sin \psi \cos \phi \\
b_{33} &= \cos \theta \cos \psi
\end{aligned} \tag{4.6}$$

The relaxors contain ions which are significantly different in size, and the effects are introduced as local expansions and contractions of bond lengths. If the changes are germane to a single layer, then the oxygen atoms around every second atom may be displaced as desired. If the distortion is to be applied to the smaller B site ion j , then the indices for the oxygen, in the three orthogonal directions are:

$$\begin{aligned}
[\pm 1, 0, 0] \quad i &= (j + l * \text{floor}(j/l^2)), (j + l + l * \text{floor}(j/l^2)) \\
[0, \pm 1, 0] \quad i &= (j + \text{floor}(j/l)), (j + 1 + \text{floor}(j/l)) \\
[0, 0, \pm 1] \quad i &= j, (j + l^2)
\end{aligned} \tag{4.7}$$

In any case, bond distortions are relatively easy to introduce. Parameters are sought for scandium, and the calculations consist of searching the data matrix constructed for the lattice coordinates for scandium and calculating the appropriate number at the scandium sites, based on a lattice sum.

4.2 Electric Field Gradient

The electric field gradient is of great importance, since Scandium is a quadrupolar nuclei and thus couples with the electric field gradient. Scandium apparently forms largely ionic bonds with oxygen in these materials based on consideration of electronegativity difference. In the absence of charge densities related to covalent bonds, expressions for the electric field gradient tensor components in a rectangular co-ordinate system are:

$$\begin{aligned}
V_{xx} &= \frac{3}{4\pi\epsilon_0} \sum_k \frac{q_k(x-x_k)^2}{r^5} - \frac{1}{4\pi\epsilon_0} \sum_k \frac{q_k}{r^3} \\
V_{yy} &= \frac{3}{4\pi\epsilon_0} \sum_k \frac{q_k(y-y_k)^2}{r^5} - \frac{1}{4\pi\epsilon_0} \sum_k \frac{q_k}{r^3} \\
V_{zz} &= \frac{3}{4\pi\epsilon_0} \sum_k \frac{q_k(z-z_k)^2}{r^5} - \frac{1}{4\pi\epsilon_0} \sum_k \frac{q_k}{r^3} \\
V_{xy} = V_{yx} &= \frac{3}{4\pi\epsilon_0} \sum_k \frac{q_k(y-y_k)(x-x_k)}{r^5} \\
V_{yz} = V_{zy} &= \frac{3}{4\pi\epsilon_0} \sum_k \frac{q_k(y-y_k)(z-z_k)}{r^5}
\end{aligned}$$

$$V_{zx} = V_{xz} = \frac{3}{4\pi\epsilon_0} \sum_k \frac{q_k(x - x_k)(z - z_k)}{r^5} \quad (4.8)$$

The quadrupole coupling constant C_Q and asymmetry parameter η are given by:

$$C_Q = \frac{e^2 q Q}{h}, \eta = \frac{V_{xx} - V_{yy}}{V_{zz}} \quad (4.9)$$

where $eq = V_{zz}$, Q is the nuclear quadrupole moment and h Planck's constant. These are expressed in terms of tensor components in the Principal Axis System (PAS) for which:

$$V_{xz} = V_{yz} = V_{xy} = 0 \text{ and } |V_{zz}| \geq |V_{xx}| \geq |V_{yy}| \quad (4.10)$$

The PAS and an arbitrary system are related via a unitary transformation, and thus the tensor values for the PAS system are given by the eigenvalues for the EFG. Proceeding in the usual manner, one solves the determinantal equation:

$$\begin{vmatrix} V_{xx} - \lambda & V_{xy} & V_{xz} \\ V_{yx} & V_{yy} - \lambda & V_{yz} \\ V_{zx} & V_{zy} & V_{zz} - \lambda \end{vmatrix} = 0 \quad (4.11)$$

Using Laplace's equation and the symmetric tensor properties, one finds:

$$\begin{aligned} & -\lambda^3 + (V_{xy}^2 + V_{xz}^2 + V_{xx}V_{zz} + V_{zz}^2 + V_{xx}^2 + V_{yz}^2)\lambda - \\ & V_{xy}^2V_{zz} + V_{xy}V_{yz}V_{xz} + V_{xz}V_{xy}V_{yz} + V_{xz}^2V_{xy} + V_{xz}^2V_{zz} - V_{xx}^2V_{zz} - V_{xx}V_{zz}^2 - V_{xx}V_{yz}^2 = 0 \end{aligned} \quad (4.12)$$

This third order characteristic equation is conveniently solved using the method of Cardan for the solution of the cubic, to yield the PAS tensor values and thus C_Q

and η . Appendix C contains a listing of the C code, `efg_pc.c` and matlab script `stat_pc.m` used to calculate these quantities and examine the output. Figures 4.2 are examples of the output for quadrupole coupling constant and asymmetry parameter distributions for PSW. The lattice size was $17 \times 17 \times 17$, with 0.15 radians tilting in the Imma system. Random site (β') unit cells were 1.18 times as large as β' unit cells, lead are displaced 0.1 Angstroms along $[-1,0,0]$ and B site atoms are displaced randomly along the major axis of octahedra, up to 0.1 Angstroms. Figure 4.3 is a plot of the convergence of the electric field gradient as a function of atomic radius. Since the sum is proportional to the inverse cubed power, it converges quickly and recourse to methods such as Ewald summation is not necessary.

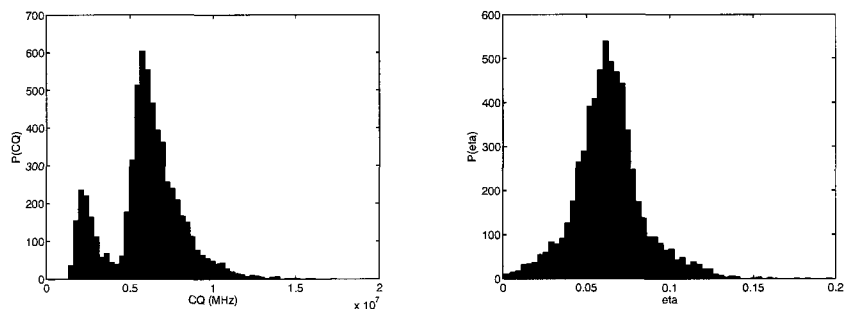


FIG. 4.2: (Left) quadrupole coupling constant and (right) asymmetry parameter distributions for PSW. The lattice size was $17 \times 17 \times 17$, with 0.15 radians tilting in the Imma system. Random site (β') unit cells were 1.18 times as large as β' unit cells, lead are displaced 0.1 Angstroms along $[-1,0,0]$ and B site atoms are displaced randomly along the major axis of octahedra, up to 0.1 Angstroms.

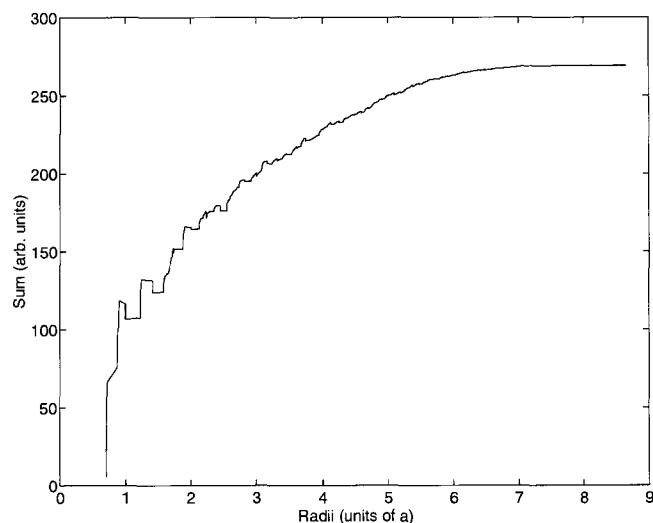


FIG. 4.3: Convergence of electric field gradient calculation, proportional to $1/r^3$, versus radius from central scandium ion in RS model for ordering in PSW.

4.3 Chemical Shift

The chemical shift is one of the most fundamental interactions of NMR and it is also the most demanding to calculate. As discussed earlier, even without anisotropy, calculation of the isotropic contribution requires knowledge of both ground and excited electronic states. The diamagnetic contribution relies largely on knowledge of the ground states and is generally the larger contribution, and an attempt will be made to calculate the effect of the surrounding ionic lattice on a valence electron of the scandium ion. This neglects contributions from covalency, exchange, and the distorted core. However, it is worthwhile to consider a single isolated $3p$ electron in order to understand trends in chemical shift, and produce correlations with charge coordination and other bonding attributes. One begins by considering the multipole expansion for the potential experienced by the electron,

due to the surrounding point charge distribution:

$$V = e\phi(r) = \frac{e}{4\pi\epsilon_0} \sum_{l=0}^{\infty} \frac{1}{r^{l+1}} \left[\sum_{i=1}^N q_i r_i^l P_l \cos(\gamma_i) \right] \quad (4.13)$$

where the Legendre polynomial is given in terms of the multipole expansion:

$$P_l(\cos \gamma) = \frac{4\pi}{2l+1} \sum_{m=-l}^l Y_{lm}^*(\theta', \phi') Y_{l,m}(\theta, \phi) \quad (4.14)$$

To second order, the interaction energy is:

$$V = e\phi(r) = e \frac{\sum q_i}{4\pi\epsilon_0 r} + \frac{e \sum_i q_i r_i P_{1i}}{4\pi\epsilon_0 r^2} + \frac{e \sum_i q_i r_i^2 P_{2i}}{4\pi\epsilon_0 r^3} \quad (4.15)$$

One may minimize the total energy using the Rayleigh Ritz variational approach and using the approximate wave function so obtained, calculate expectation values of the diamagnetic chemical shift. The following is used as a trial wave function for a $3p$ -like electron:

$$\psi = \alpha r e^{-\delta r} \sin \theta e^{-i\phi} \quad (4.16)$$

Expanding the interaction energy, one finds for the zeroth order:

$$P_0(\cos \gamma) = \frac{e \sum q_i}{4\pi\epsilon_0 r} \quad (4.17)$$

To first order:

$$P_1(\cos \gamma) = \frac{4\pi}{3} Y_{1,-1}^*(\theta', \phi') Y_{1,1}(\theta, \phi) + \frac{4\pi}{3} Y_{1,0}^*(\theta', \phi') Y_{1,0}(\theta, \phi) + \frac{4\pi}{3} Y_{1,1}^*(\theta', \phi') Y_{1,1}(\theta, \phi) \quad (4.18)$$

Using the following relations for spherical harmonics,

$$\begin{aligned}
 Y_{l,-m} &= (-1)^m Y_{lm}^* \\
 Y_{1,1} &= -\sqrt{\frac{3}{8\pi}} \sin \theta \exp i\phi \\
 Y_{1,0} &= \sqrt{\frac{3}{4\pi}} \cos \theta \\
 Y_{1,-1} &= \sqrt{\frac{3}{8\pi}} \sin \theta \exp -i\phi,
 \end{aligned} \tag{4.19}$$

one may show that:

$$\begin{aligned}
 P_1(\cos \gamma) &= \\
 \cos \theta \cos \theta' + \sin \theta \sin \theta' \cos(\phi - \phi')
 \end{aligned} \tag{4.20}$$

Similarly,

$$\begin{aligned}
 P_2(\cos \gamma) &= \\
 \frac{3}{4} \sin^2 \theta \sin^2 \theta' \cos^2(\phi - \phi') + \frac{1}{4} (3 \cos^2 \theta' - 1)(3 \cos^2 \theta - 1) + \\
 \sin \theta' \cos \theta' \sin \theta \cos \theta \cos(\phi - \phi')
 \end{aligned} \tag{4.21}$$

The total energy Hamiltonian H contains the interaction energy term and in quantum mechanics the relationship between energy and the wave function ψ is given by Schrodinger's equation:

$$H\psi = -\frac{\hbar^2}{2m} \nabla^2 \psi + V(r, \theta, \phi) \psi = E\psi \tag{4.22}$$

Based on the symmetry of the trial wave function, a spherical co-ordinate system

is used, in which the Laplacian operator is given by:

$$\nabla^2\psi = \frac{1}{r^2} \frac{\partial}{\partial r} \left(r^2 \frac{\partial\psi}{\partial r} \right) + \frac{1}{r^2 \sin\theta} \frac{\partial}{\partial\theta} \left(\sin\theta \frac{\partial\psi}{\partial\theta} \right) + \frac{1}{r^2 \sin^2\theta} \frac{\partial^2\psi}{\partial\phi^2} \quad (4.23)$$

Therefore, for the various terms, one finds:

$$\frac{1}{r^2} \frac{\partial}{\partial r} \left(r^2 \frac{\partial\psi}{\partial r} \right) = \left[-\frac{\delta\alpha}{r^2} + (2\alpha + \delta^2\alpha) \frac{1}{r} - 3\delta\alpha \right] \sin\theta e^{-\delta r} e^{-\phi} \quad (4.24)$$

$$\frac{1}{r^2 \sin^2\theta} \frac{\partial}{\partial\theta} \left(\sin\theta \frac{\partial\psi}{\partial\theta} \right) = \frac{\alpha}{r \sin\theta} \cos 2\theta e^{-\delta r} e^{-i\phi} \quad (4.25)$$

$$\frac{1}{r^2 \sin^2\theta} \frac{\partial^2\psi}{\partial\phi^2} = -\frac{\alpha}{r \sin\theta} e^{-\delta r} e^{-i\phi} \quad (4.26)$$

In order to ascertain the form of the trial wave function, the total energy,

$$I = \langle \psi | H | \psi \rangle \quad (4.27)$$

is minimized. The Hamiltonian and volume element are given by,

$$H = \frac{\hbar^2}{2m} \nabla^2 + V(r, \theta, \phi) \quad (4.28)$$

$$d\tau = r^2 \sin\theta d\theta d\phi dr \quad (4.29)$$

giving:

$$I = -\frac{\hbar^2}{2m} \int \psi^* \nabla^2 \psi d\tau + \int \psi^* V \psi d\tau \quad (4.30)$$

Using relations such as:

$$\int_0^\pi \sin^n \theta d\theta = \frac{(n-1)(n-3)(n-5)\dots}{n(n-2)(n-4)\dots} \times \begin{cases} \pi & n=\text{even} \\ 2 & n=\text{odd} \end{cases}$$

$$\Gamma(n) = \int_0^\infty e^{-x} x^{n-1} dx$$

$$\Gamma(n) = (n-1)\Gamma(n-1)$$

$$\Gamma(1) = 1$$

$$\Gamma(1/2) = \sqrt{\pi} \quad (4.31)$$

one may show that:

$$I = \frac{\pi\alpha^2}{\delta^3} - \frac{\pi^2\alpha^2}{2\delta^2} + \frac{e \sum q_i \alpha^2}{4\epsilon_0 \delta^4} + \frac{e}{15\epsilon_0} \sum_i q_i r_i^2 (1 - 3 \cos^2 \theta_i) \left(\frac{1}{\delta^3} \right) \quad (4.32)$$

This expression is subsequently minimized with respect to the variables to be determined. As one would expect, normalization constant α has no bearing, and the derivative with respect to δ alone is relevant. Figure 4.4 is a plot of the convergence of the summation contained in the expression for I . The sum is divergent and before this general approach to calculating the chemical shift may be reliable, a better approximation is required. Including further terms in the trial wave function or expanding the interaction into higher orders may prove useful. However increasing the level of complexity beyond a certain point defeats the purpose, the original motivation being a simple means to appreciate the chemical shift distribution. The rapidly developing ab-initio methods for chemical shift calculation appear to be the best approach but are outside the scope of this work.

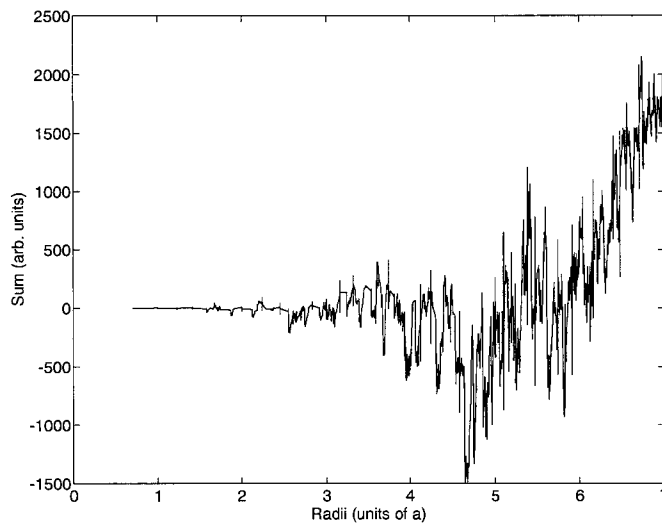


FIG. 4.4: Divergence of sum in chemical shift calculation, versus radii from central scandium ion in RS model for ordering in PSW.

4.3.1 Distribution Models and Lineshape Simulation

Using the procedures of this section one may develop a quantitative and qualitative picture of the quadrupole coupling and asymmetry parameter distributions. With the initial assumption of only statistical disorder among the β' ordered sites, and using the values of table 4.2, the distribution of figure 4.5 results for the quadrupole coupling constant of scandium. This clearly has a Gaussian profile, with normal mean μ and standard deviation σ . The limit of a normal distribution as $\sigma \rightarrow 0$ is a delta function and this situation corresponds to high symmetry and periodicity among crystal lattice positions. In this case, distinct quadrupole lineshapes would result. Once assumptions of charge displacements are introduced, quite different manifolds of parameters arise. For instance, as mentioned earlier, oxygen atoms for the calculation of figure 4.4 undergo rotations about the z -axis, with O-B-O bond lengths compressed for smaller B site atoms. The mean and

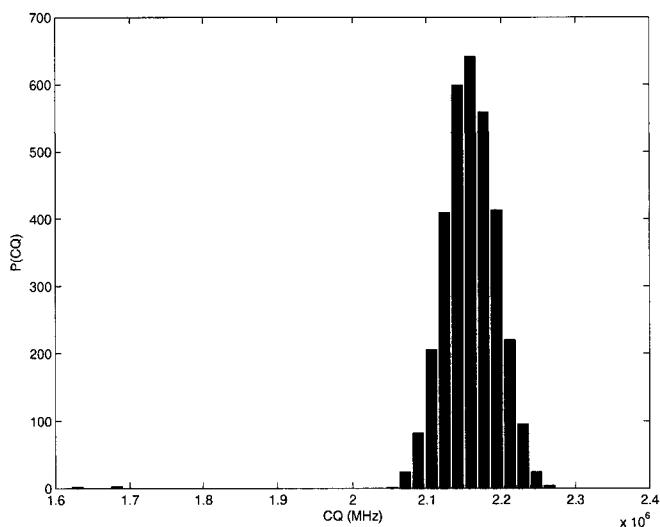


FIG. 4.5: Distribution of quadrupole coupling constant in PSW, using RS model for ordering with no structural distortions.

mode of the distribution no longer correspond. This general effect on the distribution of parameters is quite germane to disordered materials. Czjcek [33, 16] has given empirical relationships between probability distributions and parameter such as the asymmetry and quadrupole coupling constant, for amorphous solids. This model has been applied with success when sampling distributions for NMR simulations, to various systems [8]. However the Czjcek distribution is derived under the assumptions of identical (monatomic) ions, and is bivariate in asymmetry parameter and the z component of the electric field gradient.

The general progression from delta function to normal distribution and finally an asymmetric distribution can be appreciated more clearly by considering the distance between atoms and their chemical nature as the variates. Atoms which experience a purely isotropic environment give single relevant NMR parameters, or a delta function type distribution. Where substitution of atoms occurs in the form of vacancies or different species, atomic occupation takes on certain probabilities;

the distance between atoms may remain fairly regular and is a normal variate. The mean of the normal distribution of parameters which results corresponds to the most probable environment. Finally, as structural disorder is included or displacements with degrees of randomness, the variate distance takes a Poissonian character. The gamma distribution,

$$P(x) = \frac{(x - b)^{a-1} e^{-(x-b)/\lambda}}{\Gamma(a)\lambda^a} \quad (4.33)$$

displays the necessary qualities and thus serves as a useful model for ionic materials which exhibit both structural and chemical disorder. It is characterized by mean μ and variance σ^2 given by:

$$\mu = b + a\lambda$$

$$\sigma^2 = a\lambda^2 \quad (4.34)$$

Figure 4.6 displays the distribution function for various values of a .

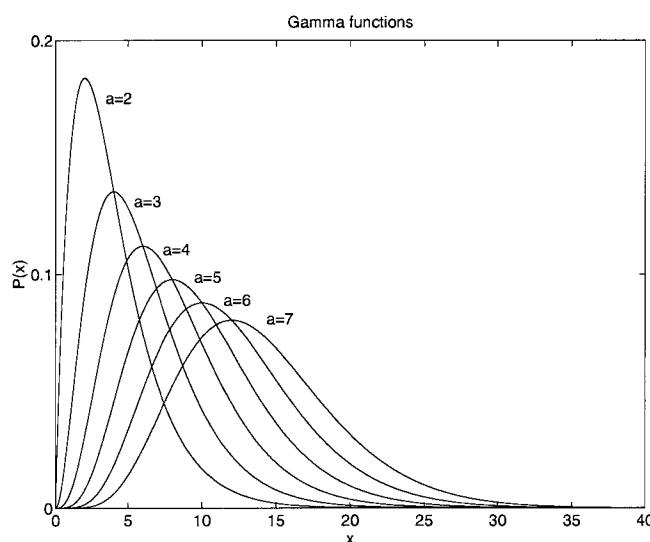


FIG. 4.6: Gamma distribution for various values of a .

Given that the asymmetry parameter appears to be almost single valued, a single variate gamma distribution is used for the quadrupole coupling constant only. The correlation with chemical shift and the nature of this distribution remain to be seen, and at this stage a normal distribution is used to model chemical shift. Using the methods developed here to calculate distributions, as well as predict probabilities for nearest B site neighbor probabilities and model distributions, one is equipped to interpret NMR spectra for disordered materials. An illustrative first test of this approach as well as the simulations detailed in section 2, is the well-ordered sample PST.

Chapter 5

Experiment

5.1 Lead Scandium Tantalate (PST) 3QMAS

Well ordered Lead Scandium Tantalate $\text{Pb}_2\text{Sc}_{1/2}\text{Ta}_{1/2}\text{O}_3$ (PST) is ferroelectric and will provide a good contrast to the solid solutions based on PSW, which are predominantly relaxor-ferroelectric. Chu et al [27] discuss the difference between relaxor and normal ferroelectric PST and largely attribute the difference to the presence of lead deficient A sites in the relaxor. PST in both disordered and ordered versions has been studied via Raman Spectroscopy [84] where the nature of the phase transition is attributed directly to lead static and dynamic displacements. A sample of PST was obtained from the University of Pennsylvania and experiments performed at various fields. This particular sample has been subjected to extensive thermal annealing and has been characterized by neutron diffraction. Pure layers of Scandium are interleaved with pure layers of Tantalum in a 1:1 ratio along [1,1,1]. The ordered form of the material displays a normal, distinct ferroelectric to paraelectric phase transition [86].

5.1.1 Results

The MAS experiment at 17.6T was performed at 20kHz spinning speed, spectral bandwidth 1MHz, 100ms recycle delay, using ScCl_3 as the frequency reference. The resulting spectrum is presented in figure 5.1.

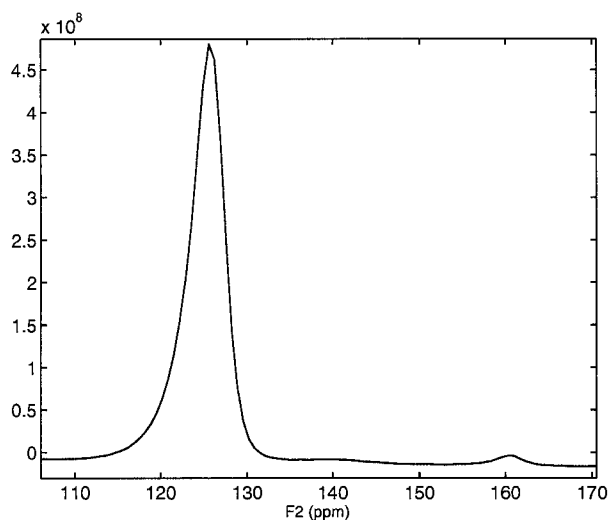


FIG. 5.1: ^{45}Sc MAS spectra of PST at 17.6 T and 20kHz spinning speed. Clearly visible are peaks at 125.4ppm and 159.9ppm, with respect to ScCl_3 reference. The smaller peak most likely corresponds to small amounts of Scandium in the pure Tantalum layer.

The spectrum is composed of two peaks, and the larger is attributed to single ordered position of Scandium, surrounded by six nearest B-site neighbor (nBn) Tantalum. A second, smaller peak may indicate low concentrations of Scandium on the pure Tantalum layers, surrounded by six Scandium nBn's. To determine the relative contributions of chemical shift and the quadrupole coupling to the line shape, an MQMAS experiment was conducted. The particular data presented in figure 5.2 was taken during May of 2003 at 19.6T, at the National High Magnetic Field Laboratory. In order to simulate the significant scandium site, it was necessary to model the distribution in quadrupole coupling constants as a gamma

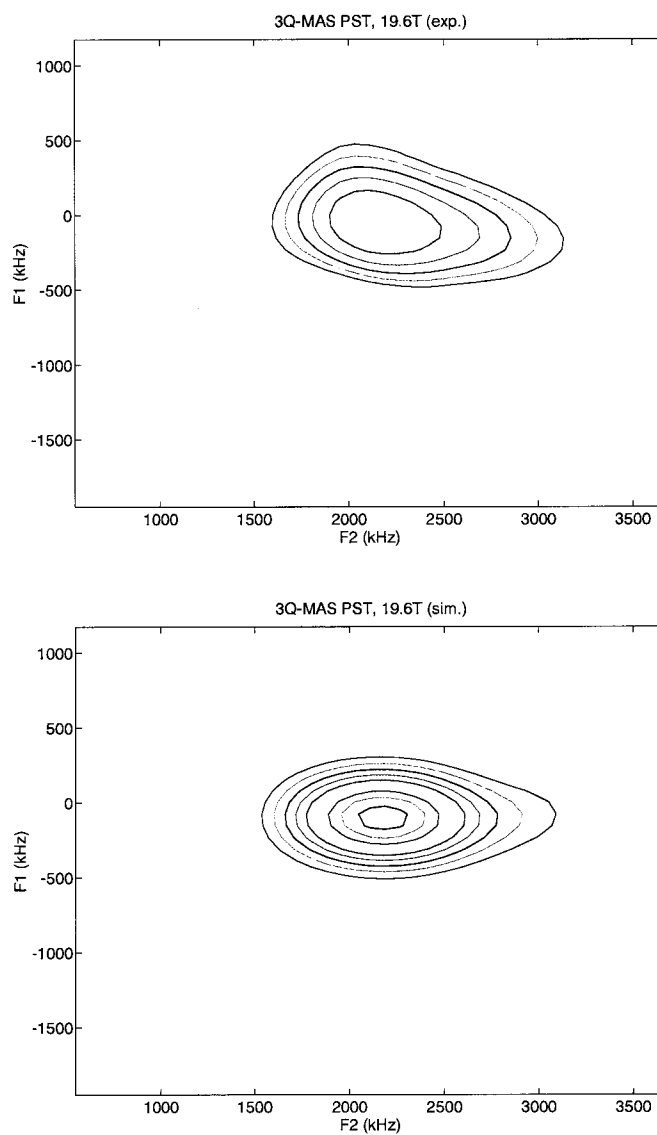


FIG. 5.2: Experimental spectra (top) for PST, 3QMAS at 19.6T, with simulation (bottom)

function. The chemical shift distribution was modeled as a narrow Gaussian. As mentioned previously, a gamma function will account for a more disordered arrangement of atoms. Given it's application here, this would seem to indicate that PST displays some local disorder, the nature of which remains to be determined. Given that only one significant peak is observed, there appears to be no second, chemically disordered β' layer and hence the asymmetric distribution must arise from structural displacements. The best fit values for the quadrupole coupling constant and asymmetry parameter are 3.8 ± 0.4 MHz and 0.9 respectively. The former is based on a gamma function distribution of second order, and without optimization these values are estimated to be accurate to within 10%. To provide confirmation, a second measurement was taken at 7T.

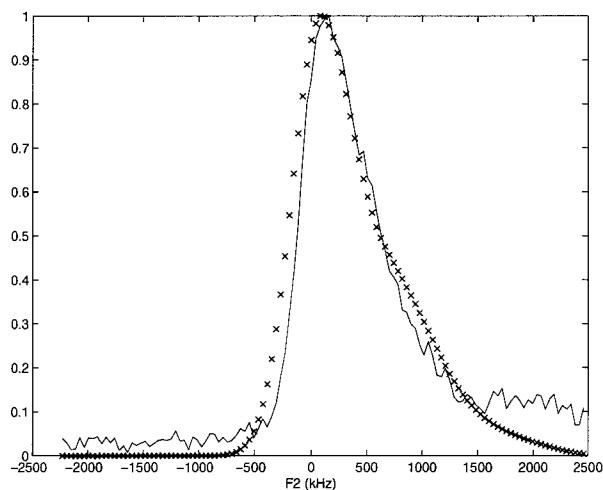


FIG. 5.3: Experimental and simulated (broken line) 3QMAS F2 projection for PST, 7T

An example spectra, showing skyline projections for the experimental and simulated direct dimension are shown in figure 5.3, again at ambient temperature. In order to interpret the results for PST, calculations using the methods described

in chapter four were conducted.

5.1.2 Calculations

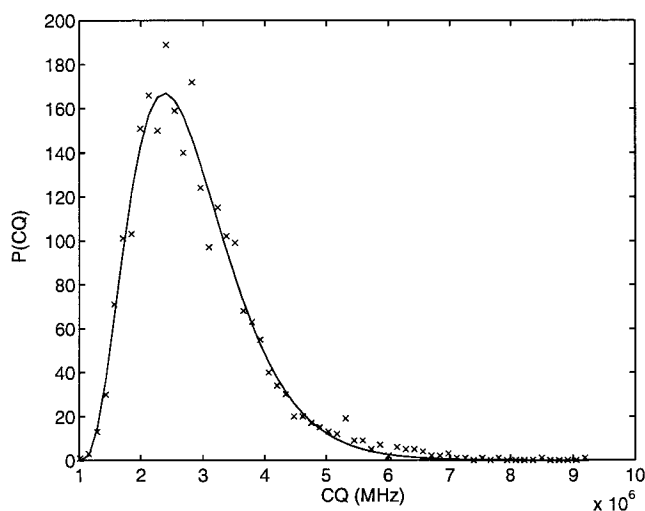


FIG. 5.4: Calculated C_Q distribution with least squares fit. Mean and standard deviation are 2.8 and 0.9 MHz, respectively. These are slightly lower than experimental values, perhaps due to the presence of covalency.

Using predicted stoichiometry, and introducing a tilt angle to oxygen octahedra of 0.05 radians in the Imma system, lattice coordinates were generated for PST. For each scandium ion, quadrupole coupling constants were calculated. Lead anions were given small random displacements up to 0.1 Angstroms and B cations up to 0.12 Angstroms, in order to reproduce the the distribution of figures 5.4. The B site displacement would imply that charge overlap or covalent bonding may take place between some B atoms and the oxygen, given their ionic radii. In order to determine realistic displacements for the lead atoms, the point charge interaction energy between a central lead atom and the first two shells composed of twelve oxygen and six B atoms respectively was calculated. While the value for energy

is proportional to $1/r$ and will not converge over this length scale, a direction for displacement may be determined. Referring to figure 5.5, the almost equal values for the energy minima would indicate no preferential displacement for lead. Figure 5.5 is a plot of interaction energy versus x and y coordinates with the oxygen polyhedra surrounding the lead (bottom). This general lack of preference for lead atoms was common to all investigated, although it was observed that with more significant tilting a slight preference could be established. These displacements are heavily correlated with the oxygen rotations and in turn rotations are necessary in perovskites due to steric differences between oxygen and B site atoms. Since it is the lead positions which largely determine the overall polarization, this feature is significant.

The absolute value of these energy minima should differ from the relaxors where polarization is much more pronounced and the phase transition more disperse. These results will be compared with those of the relaxor ferroelectrics (1-x)PSW-xPT and (1-x)PSW-xPZ in order to understand the fundamental origins of the relaxor behavior. However in order to first correlate chemical shifts and quadrupole coupling constants with specific distortions such as bond lengths and angles, a survey will be made of simple crystalline scandium compounds.

5.2 Model Compounds

The study of simple crystalline materials can provide insight into more complex materials. By virtue of their periodicity and well ordered nature, model compounds often have well established structural information, characterized by x-ray diffraction. Structural details such as bond lengths and angles may be correlated with NMR parameters such as chemical shifts and quadrupole coupling

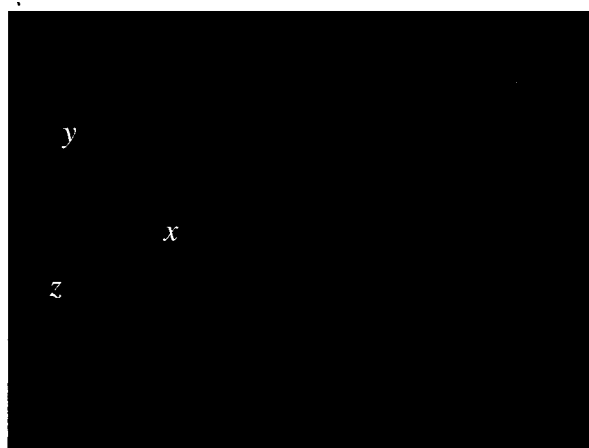
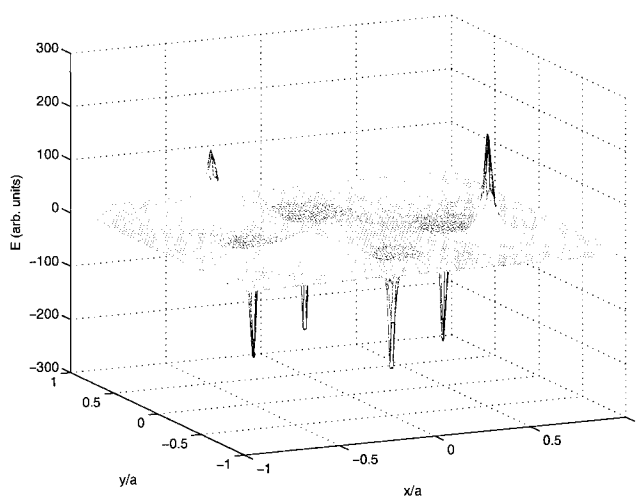


FIG. 5.5: (Top) Plot of interaction energy versus x and y coordinates for lead in an undistorted perovskite lattice. Interaction energy is calculated in a point charge model between lead, first shell (12 Oxygen) and second shell (8 B sites), for cubic symmetry and no oxygen distortions. Out of four possible directions for displacement, none are more likely. (Bottom) Rendering of 3D oxygen polyhedra around lead for the same assumptions.

constants. These correlations may be applied to disordered materials in order to provide quantitative structural information. Fayon et al [29] developed a correlation between the ^{207}Pb chemical shift and both the lead-oxygen bond distance and co-ordination number, for crystalline ionic materials. Vermillion et al [49] perform point-charge and ab-initio calculations to determine the relationship between ^{17}O quadrupolar coupling parameters and the local structure around the bridging oxygen in the case of alkali silicates. Clark et al [83] combine ab-initio calculations with NMR experiment to determine a dependency of the ^{17}O quadrupole coupling parameters on both the Si-O-Si angle and Si-O bond distance. The quadrupole coupling constant in particular is dependent on both the bonding angle and distance. The intention here is similar, namely to develop correlations between the quadrupole coupling constant and scandium-oxygen bond distances and angles, in order to quantify local structure in the more complex relaxors.

Several scandium compounds were obtained from Alpha Aesar and used without further purification. Single pulse Magic Angle Spinning experiments were performed for speeds 15kHz and 30kHz, although 15kHz was sufficient in most cases. The 90 degree pulse was selective on the central transition with duration $p_1 = 4.1\mu\text{s}$ and power $pl_1 = 22.00$, recycle delay from $200\text{ms} - 2\text{s}$ depending on the material. The carrier frequency of 72.907223 MHz was set to the Larmor frequency of reference compound ScCl_3 . DMFIT [20] was used to simulate second order lineshapes for the nine spectra obtained; several spectra are illustrated in figure 5.7. Where unambiguous assignment could be made at 7T, parameters are contained in table 5.1. Scandium chloride and fluoride did not have distinctive lineshapes, an indication that fast motional averaging may take place. However, reducing the temperature to -60°C in scandium fluoride produced little or no change. Scandium oxide and sulfate have multiple, overlapping sites at 7T. The

existence of structural information for both these compounds prompted further experiments at higher fields, in order to improve resolution.

TABLE 5.1: Deconvolutions for ^{45}Sc MAS at 7T, of several model scandium compounds.

Compound	Site	C_Q (MHz)	η	I(%)	Position(ppm)	Lor. brd.(Hz)
Sc Acetate	1	4.3	0	1	-5.9	106
Sc Oxalate	1	12.6	0.2	1	25.4	73
Sc Carbonate	1	2.5	1	70	26.4	1108
	2	5.8	0.7	30	26.3	323
Sc Nitrate	1	4.3	0	5	-17.9	120
	2	5.9	0.75	58	-19.2	120
	3	6.4	1	37	30.5	140

TABLE 5.2: Deconvolutions for ^{45}Sc 3QMAS, 17.6T of scandium oxide and sulfate.

Compound	Site	C_Q (MHz)	η	I(%)	δ_{iso} (ppm)	Lor. brd.(Hz)
Sc Oxide	1	22.9	0	33.3	56.2	200
	2	15.1	0.65	66.6	34.8	200
Sc Sulfate	1	5.5	0.1	20	4.5	120
	2	4.2	0.9	30	2.3	120
	3	4.6	0.5	50	-6.2	120

Figures 5.8-5.10 display both experimental and simulated spectra, with the parameters obtained from the simulation procedure given in table 5.2. Structural information including Wyckoff sites is listed for scandium oxide in table 5.3. Referring to the frequency spectrum for scandium sulfate (fig 5.9), x-ray data gives two scandium sites, surrounded by eight oxygen, however three distinct sites are observed. The two sites with similar chemical shift most likely correspond to a splitting of some kind, but without further information assignment is ambiguous. In the case of scandium oxide, the assignment is much more obvious, the integrated intensities occurring roughly in the proportion (1:3) given in table 5.3. This result

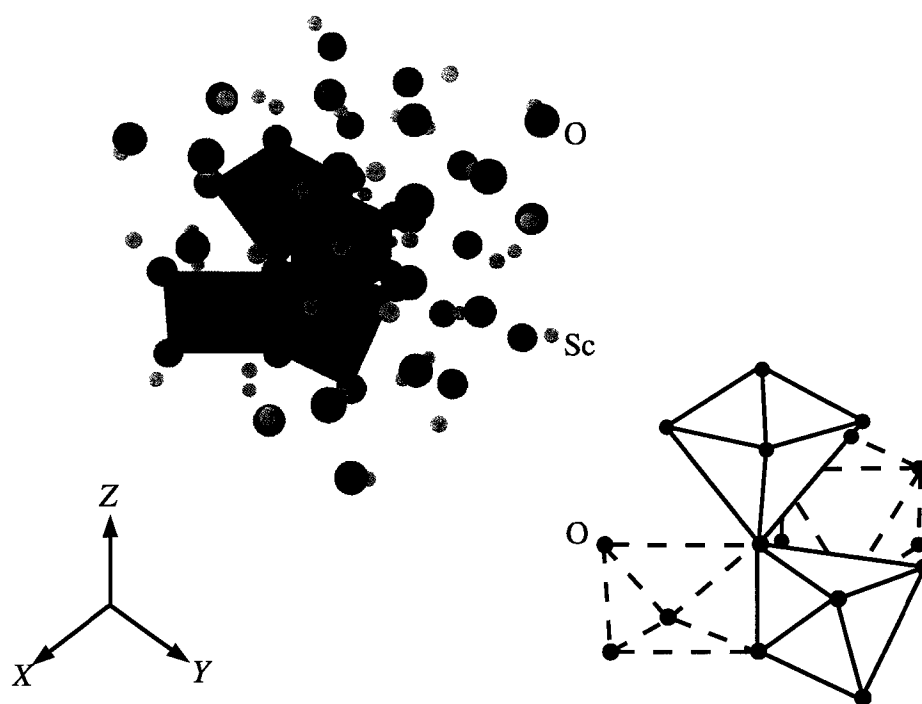


FIG. 5.6: Structure of scandium oxide, revealing distorted and undistorted (dashed) oxygen octahedra

is highly useful, since the structure of scandium oxide is analogous to the doubled perovskite, devoid of the A lattice, figure 5.6. Scandium in the least populated site are surrounded by an octahedral coordinations of oxygen, with an average O-Sc-O angle of 113.9° . There is some discernible tilting taking place between these structures, but this feature is restricted to this single scandium site. The second scandium is also octahedrally coordinated, but with a lower O-Sc-O angle of 99.5° . Somewhat counter-intuitively, this lower symmetry site has a smaller quadrupole coupling constant (14.5 MHz) but correspondingly larger asymmetry parameter (0.5). Until further information is obtained, a reliable correlation cannot be drawn between isotropic shifts and bonding information, however, scandium oxide will provide a useful reference to the Relaxor ferroelectrics PSW-PT and PSW-PZ.

TABLE 5.3: Scandium Oxide unit cell (Ia-3) parameters

Atom	No.	OX	SITE	x	y	z
Sc	1	+3	24 d	-0.03545(5)	0	0.25
Sc	2	+3	8 b	0.25	0.25	0.25
O	1	-2	48 e	0.3893(3)	0.1530(2)	0.3849(4)

5.3 (1-x)PSW-xPT/PZ Magic Angle Spinning

The present materials under consideration were synthesized and characterized by dielectric, X-ray and Neutron diffraction at the University of Pennsylvania [64]. The tungstate relaxor ferroelectric perovskite $\text{Pb}(\text{Sc}_{2/3}\text{W}_{1/3})\text{O}_3$ PSW has 1:1 random site structure along the [1,1,1] direction; layers of pure Sc are interleaved with mixed layers containing 2:1 ratio of Sc/W. It was determined [64] that introduction of Zr (PSW-PZ) destabilizes the RS order, whilst Ti (PSW-PT) maintains order up until $x \approx 0.25$. Beyond the Morphotropic Phase Boundary (MPB) at $x = 0.25$ all

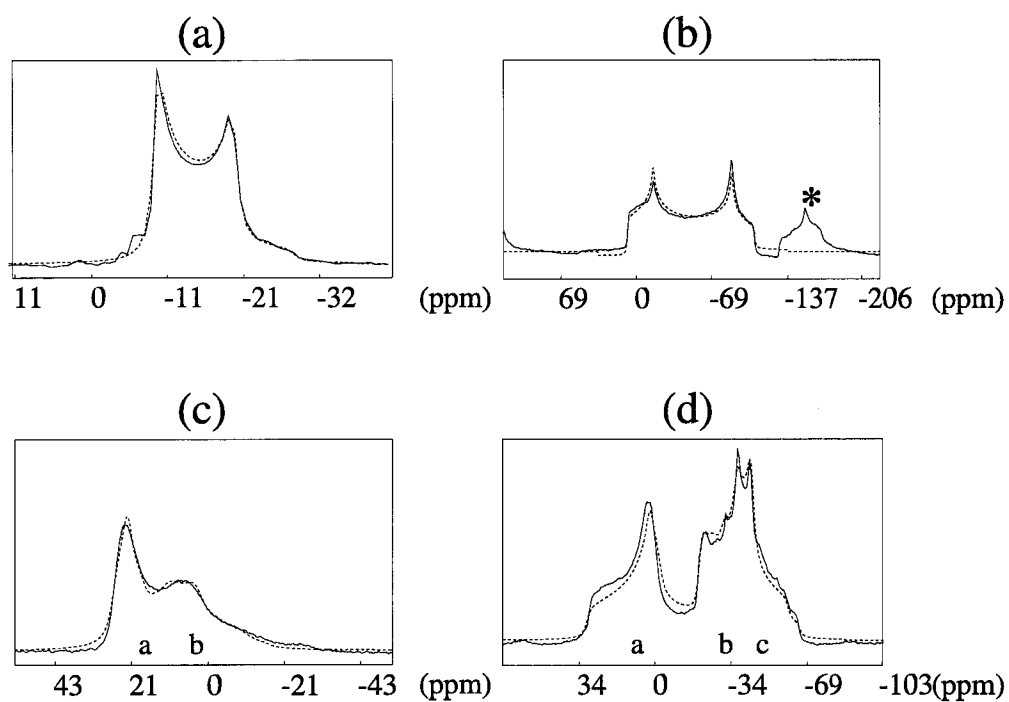


FIG. 5.7: ^{45}Sc MAS experiment and simulation (broken line) at 7T, 20kHz spinning speed, for: (a) scandium acetate, (b) scandium oxalate, (c) scandium carbonate and (d) scandium nitrate. (a) and (b) have single sites, whilst (c) and (d) have two and three respectively, indicated by letters. A spinning side band (*) is visible in (b).

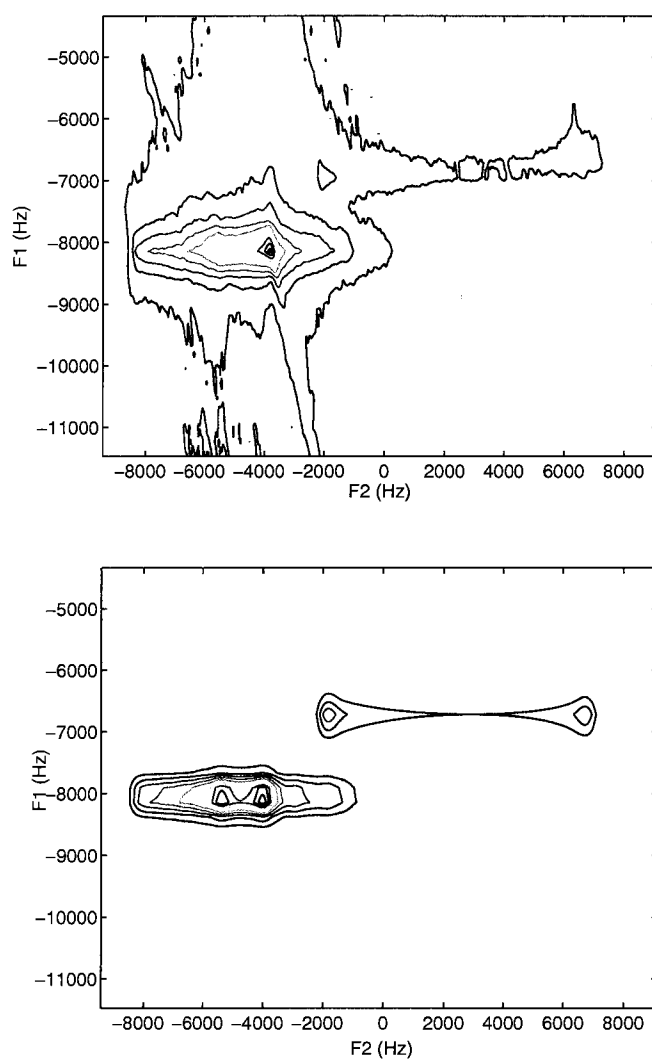


FIG. 5.8: Experimental spectra (top) for scandium oxide, ^{45}Sc 3QMAS at 17.6T and 15 kHz spinning speed, with simulation (bottom).

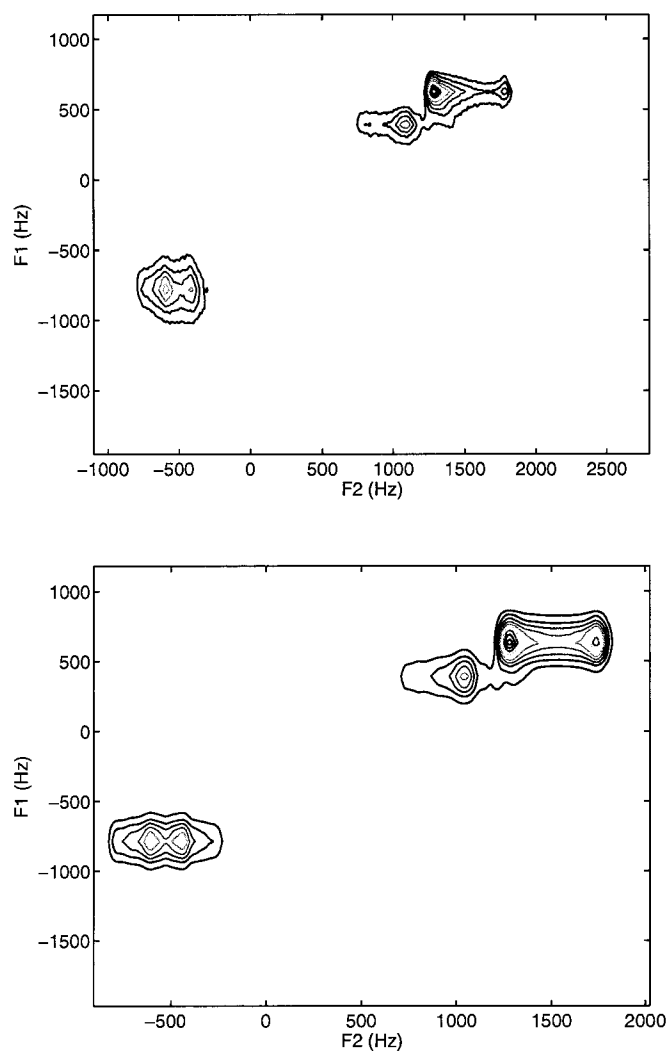


FIG. 5.9: Experimental spectra (top) for scandium sulfate, ^{45}Sc 3QMAS at 17.6T and 15 kHz spinning speed, with simulation (bottom)

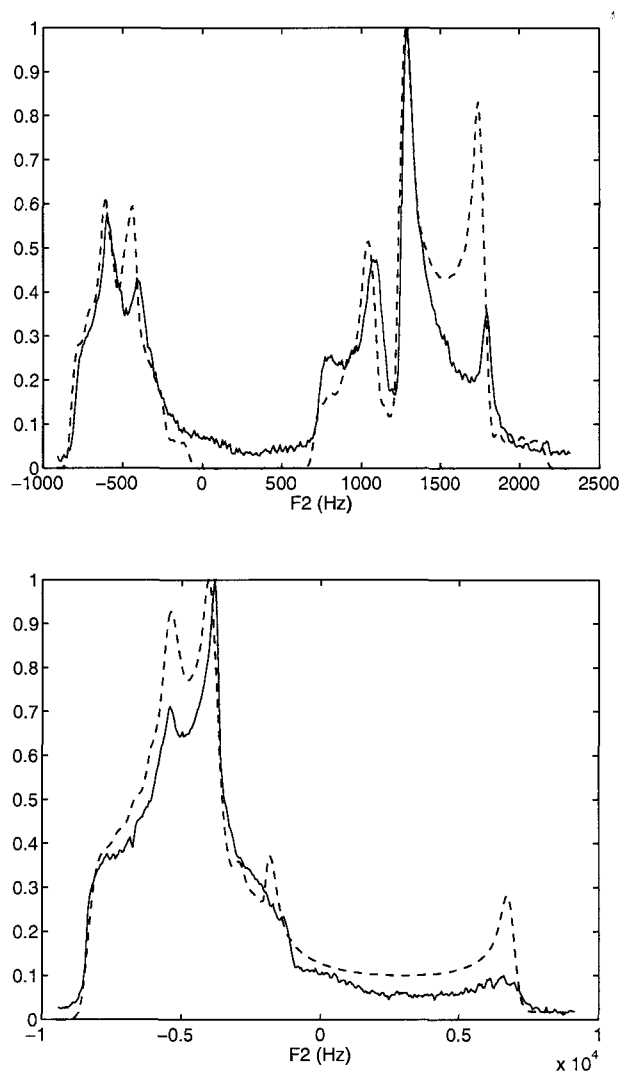
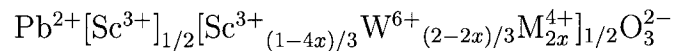


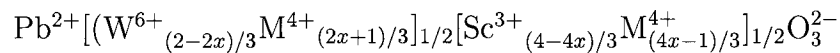
FIG. 5.10: Experimental and simulated (broken line) direct dimensions for 3QMAS experiments; scandium sulfate (top) and scandium oxide (bottom)

materials display marked relaxor behavior. Therefore, the materials to be studied have structural characteristics which lie between fully ordered perovskite ferroelectrics and disordered, relaxor ferroelectrics. Both ferroelectrics and disordered materials have been studied via NMR since at least the 1950's [3, 71, 10, 34]. More recently Blinc et al [67] applied ^{93}Nb NMR to a single crystal of the relaxor PMN. A temperature dependence for the Edwards-Anderson order parameter is established as well as a local polarization distribution function. The so-called 'spherical random bond-random field' (SRBRF) model for relaxor ferroelectrics is also proposed. In later work [69], $\text{Pb}(\text{Sc}_{1/2}\text{Nb}_{1/2})\text{O}_3$ is studied via ^{207}Pb , ^{45}Sc , ^{93}Nb NMR, above and below T_c in attempts to give both validity to the SRBRF model ascertain the percentage(s) of the crystal occupied by ordered and disordered regions. Prasad et al [77] studied PMN via ^{93}Nb MAS NMR and find wide variance in the value of the quadrupole coupling constant for the three discernible chemical sites for niobium, ranging from less than 1.2 MHz to above 62 MHz. Further work [43, 78] used MQMAS to more accurately obtain quadrupolar products and isotropic chemical shifts for these sites. In addition to these studies of B site atoms, there exists several published NMR investigations of ^{207}Pb on the A site [18, 68]. The most abundant oxygen isotope has zero spin which precludes its observation. However, the phase transition behavior in the ferroelectric BaTiO_3 is studied via ^{17}O NMR [21], inviting the study of oxygen sites in ^{17}O enriched relaxors. The most sensitive nuclei in the present materials is ^{45}Sc and accordingly ^{45}Sc MAS Experiments were performed on the solid solution series (1-x)PSW-xPT and (1-x)PSW-xPZ at the National High Magnetic Field Laboratory in Florida. Attempts made to use probe nuclei in addition to scandium (including Tungsten, Tantalum) proved fruitless owing to instrumental and sensitivity limitations. In all cases, experiments were performed with 10kHz spinning speed, spectral bandwidth 1MHz,

1024 scans, 100ms recycle delay, with the carrier frequency set to a ScCl_3 reference of 202.94 MHz. Deconvolutions were made using the DMFIT [20] software, using simple combinations of Lorentzian and Gaussian lineshapes. Spinning sidebands are visible and indicated by an asterisk. Best fit parameters for isotropic shift (δ), full width at half maximum height (Δ) and integrated intensity (I) are reported in tables 5.5,5.6 and the spectra are displayed in figures 5.11,5.12. DMFIT gives an error estimate of 5% for these values. One of the ordered positions for the B site cations (β'') is assumed to be occupied exclusively by Sc^{3+} . Substitution of Ti^{4+} or Zr^{4+} occurs on the random site position (β') which for all concentrations has a mixture of cations. Given these assumptions and the overall requirement of charge neutrality, one has for the stoichiometry [64] for $0 \leq x \leq 0.25$;



where M^{4+} may be either Ti^{4+} or Zr^{4+} . Depletion of Sc at $x = 0.25$ leads to substitution on both ordered sites after this point and the stoichiometry for $0.25 < x \leq 1.0$;



Given the predicted stoichiometry's and the existence of the random layer, one may from the nominal distribution calculate the nearest B site neighbor (nBn) probabilities, reproduced in figure 5.14.

Since the integrated intensities of NMR lineshapes are proportional to the number of spins in a particular environment, one may make assignments on this basis. Comparing the entries from the figure 5.14 with tables 5.5 and 5.6, the

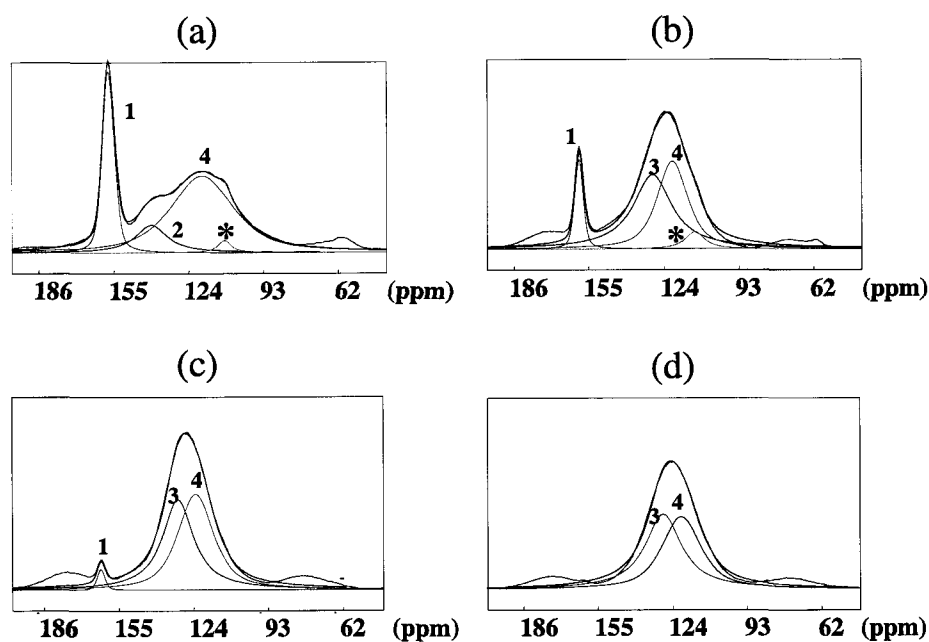


FIG. 5.11: ^{45}Sc MAS experiments for $(1-x)\text{PSW}-x\text{PT}$, conducted at 19.6T and 10 kHz spinning speed; (a) $x=0$, (b) $x=0.15$, (c) $x=0.25$ and (d) $x=0.35$. In (a), (b) and (c) narrow peak one arises from scandium on mixed β' sites, surrounded by six nBn scandium. In all, broad peaks correspond to scandium on pure β'' sites surrounded by mixed nBn shells, comprised of varying quantities of scandium, titanium and tungsten atoms.

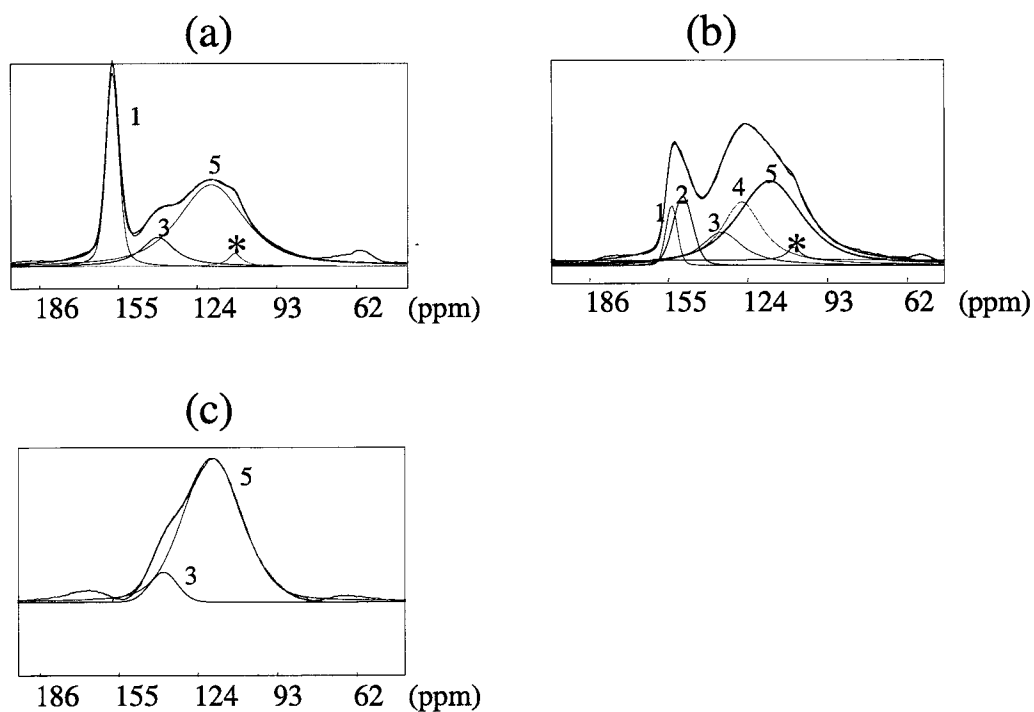


FIG. 5.12: ^{45}Sc MAS experiments for $(1-x)\text{PSW}-x\text{PZ}$, conducted at 19.6T and 10 kHz spinning speed; (a) $x=0$, (b) $x=0.15$ and (c) $x=0.35$. In (a), (b) and (c) narrow peak one arises from scandium on mixed β' sites, surrounded by six nBn scandium. In all, broad peaks correspond to scandium on pure β'' sites surrounded by mixed nBn shells, comprised of varying quantities of scandium, zirconium and tungsten atoms.

TABLE 5.4: MAS deconvolutions for (1-x)PSW-xPT, ^{45}Sc , 19.6T, $\nu_r = 10\text{kHz}$

x	Line. No.	$\delta(\text{ppm})$	$\Delta(\text{ppm})$	$I(\%)$
0	1	157.3	5.82	24.7
	2	139.5	15.8	12.5
	4	118.5	30.8	60.6
	5*	109.2	6.4	2.2
0.15	1	159.1	4.3	10.1
	3	128.8	19.1	46.5
	4	120.6	14.9	38.1
	5*	111.3	9.4	5.3
0.25	1	160.3	4	2.2
	3	128	15.7	47.3
	4	120.6	17.8	50.5
0.35	3	128	18.2	52.3
	4	120.6	19.2	47.3

TABLE 5.5: MAS deconvolutions for (1-x)PSW-xPZ, ^{45}Sc , 19.6T, $\nu_r = 10\text{kHz}$

x	Compt. No.	$\delta(\text{ppm})$	$\Delta(\text{ppm})$	$I(\%)$
0.15	1	157.3	5.4	4.8
	2	152.9	9.3	9.5
	3	137.5	19.6	13.4
	4	129.6	19	24.7
	5	118.5	30	45.9
	6*	109.2	6.4	1.7
0.35	3	146.3	13.2	8.2
	5	126.6	27.9	91.8

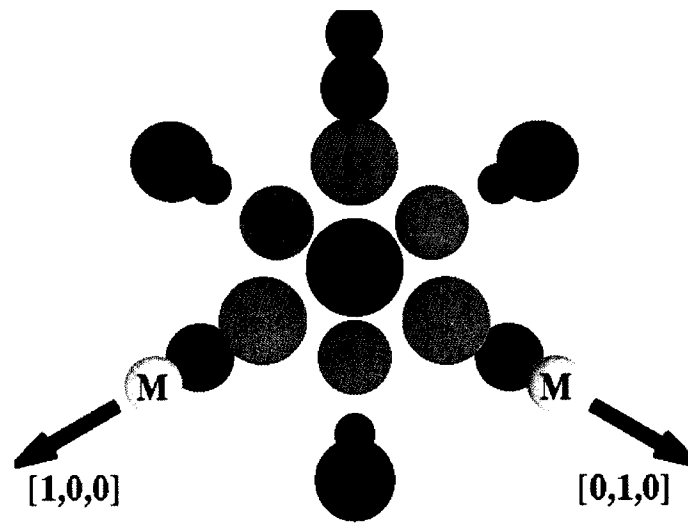


FIG. 5.13: Broad MAS peaks correspond to scandium on β'' ordered sites, surrounded by mixed charges in 1:1 RS model. The B cation on β' sites (labeled M) may be Ti/W/Zr/Sc.

$x = 0$		$x = 0.15$							
		0M							
25.1	6Sc	11.8	1M						
1.23	5Sc	0.01	0	2M					
6.27	4Sc	0.13	0.14	0.03	3M				
16.46	3Sc	0.76	1.21	0.64	0.11	4M			
24.69	2Sc	2.43	5.13	4.08	1.44	0.19	5M		
19.75	1Sc	4.12	10.92	11.56	6.12	1.62	0.17	6M	
6.58	0Sc	2.92	9.28	12.28	8.67	3.44	0.73	0.06	
			6W	5W	4W	3W	2W	1W	0W
		0.66	5.19	16.98	29.61	29.04	15.19	3.31	$x \geq 0.25$

FIG. 5.14: Nearest B-site Neighbor (nBn) configuration probabilities for scandium in $(1-x)$ PSW- x PT/PZ; M may be either titanium or zirconium. The number of tungsten cations is constant along diagonals, scandium along rows and M along columns.

integrated intensity of peak one for the PSW-PT series follows the predictions of the RS model as a function of x . The peak is also present above $x = 0.25$ where scandium is fully depleted, indicating a residual presence of scandium on the β' plane. The other prominent feature(s) of all spectra are the broad contributions which are assigned to β'' scandium, surrounded by predominantly mixed nBn shells, figure 5.13. These broad spectra are likely composed of large distributions of relevant NMR parameters. The PSW-PZ series shows slightly different behavior as a function of x . It appears that lines are broader and in addition there appears to be some splitting of specific lines. While tungsten and titanium are similar in size (≈ 0.6 Å radii) they have different electronegativity, valence charge and belong to different periods. On the other hand, scandium and zirconium are almost identical in size. At this stage, it appears that steric effects are driving the predominant features, and give rise to the differences between equivalent concentrations of PSW-PT and PSW-PZ. However, beyond the task of simple assignment, MAS experiments are insufficient to determine NMR parameters which may give structural information. This is in large part due to the lack of resolution, in distinction to earlier work [35]. Low resolution in quadrupolar solid state NMR may be alleviated in certain instances by using Multiple Quantum MAS (MQMAS) techniques [6, 36].

5.4 (1-x)PSW-xPT/PZ 3QMAS experiments

Triple Quantum Magic Angle Spinning Experiments were performed on the solid solution series (1-x)PSW-xPT and (1-x)PSW-xPZ at the National High Magnetic Field Laboratory in Florida. In all cases, experiments were performed at 19.6T with 10kHz spinning speed, spectral bandwidth 1MHz in F2, 10kHz in F1,

1024 scans, 100ms recycle delay, with the carrier frequency set to a ScCl reference at 202.94 MHz. Spectra are displayed in figures 5.15 and 5.16.

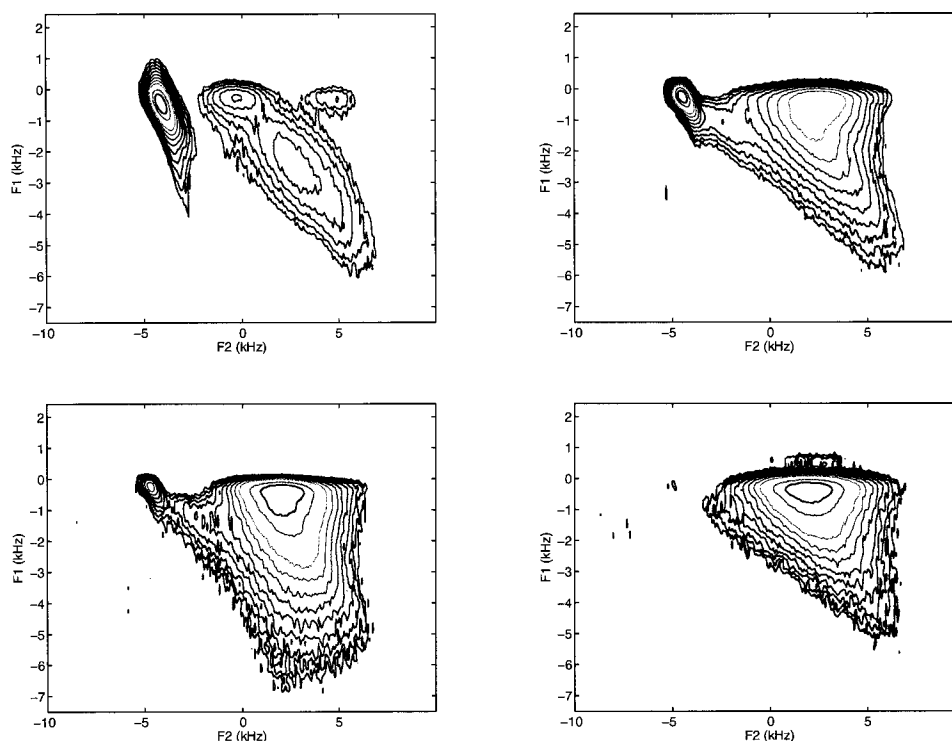


FIG. 5.15: $(1-x)$ PSW- x PT 3QMAS, 19.6T. Clockwise from top left: $x=0$, $x=0.15$, $x=0.35$, $x=0.25$

The particular presentation of the 2D spectra corresponds to a shearing factor of 3, which eliminates the chemical shift interaction in the indirect dimension for all quadrupolar spins. This shearing transformation gives a measure of the electric field gradient or quadrupole coupling constant maximum, from the bary center of the lineshape in F1. Applying this elementary analysis to PSW, the scandium β' site has a dispersion of quadrupole coupling constants, with mean $C_Q \approx 4$ MHz and small dispersion in chemical shifts. This stands in distinction to the β'' site which

appears to have two regions, one with small C_Q and another with distributions in both chemical shift and C_Q . The mean of the latter appears to be between 10 and 15 MHz. 0.85PSW-0.15PT has lower resolution than PSW. As scandium concentration on the β' site has dropped, the integrated intensity drops also for the corresponding peak. By comparison with the MAS spectra, peaks three and four correspond to regions of small (mean ≤ 4 MHz) and large (mean ≥ 10 MHz) C_Q distributions.

As concentration x increases in the PSW-PT series, the trend continues. The β' peak disappears, while the lower C_Q region increases in intensity and fills out to form an angular spectrum. The PSW-PZ series shows similar trending, although there appears to be a splitting of some peaks, alluded to earlier with regard to MAS spectra. The distributions in quadrupole coupling constant were modeled using gamma functions, and the chemical shift was modeled using Gaussian functions. Using a gamma function model for the Electric field gradient is justified on the basis of the distance between ions having a Poissonian character, a direct result of local disorder. For most concentrations, at least 1000 samples were required for each distribution, in order to provide converged spectra. Simulations for several solutions are displayed in figure 5.17, 5.18 and the values obtained in simulations displayed in table 5.6, for those concentrations where reasonable agreement between simulation and experiment could be obtained. The simulations are not exact, but do provide confirmation of underlying Poissonian nature of ionic displacements. Several F2 projections of experimental and simulated spectra are given in figure 5.18. It appears as if the early onset of disorder in 0.85PSW-0.15PZ is manifest as a splitting in quadrupole coupling constant distributions for both ordered positions, as compared to 0.85PSW-0.15PT. To further explain the derived quantities, studies of model compounds were undertaken.

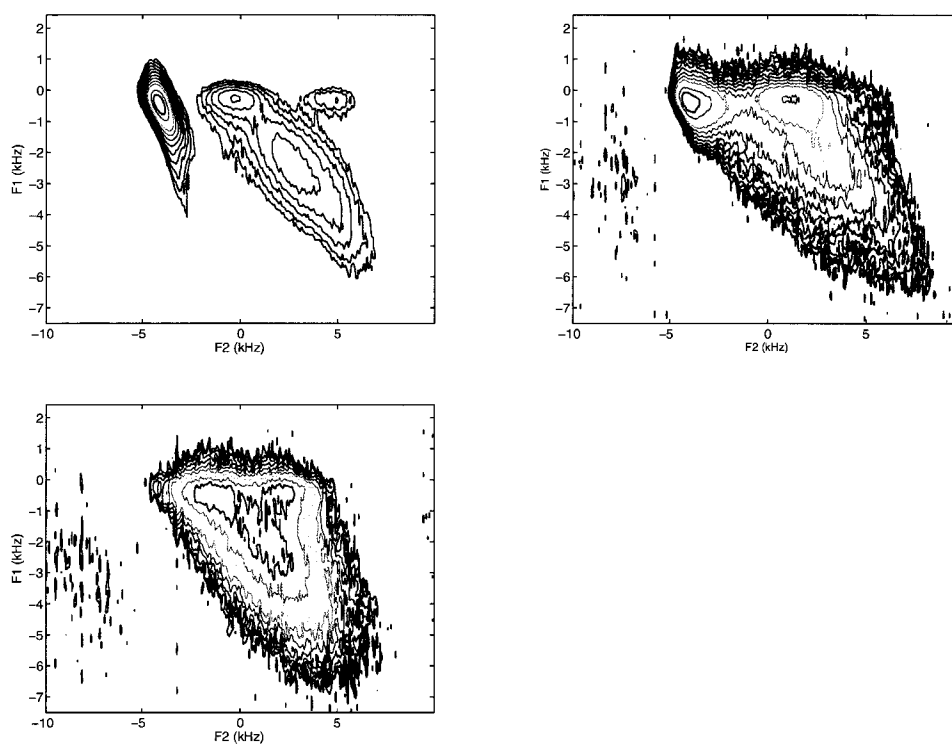


FIG. 5.16: $(1-x)$ PSW- x PZ 3QMAS, 19.6T. (Clockwise from top left): $x=0$, $x=0.15$, $x=0.35$

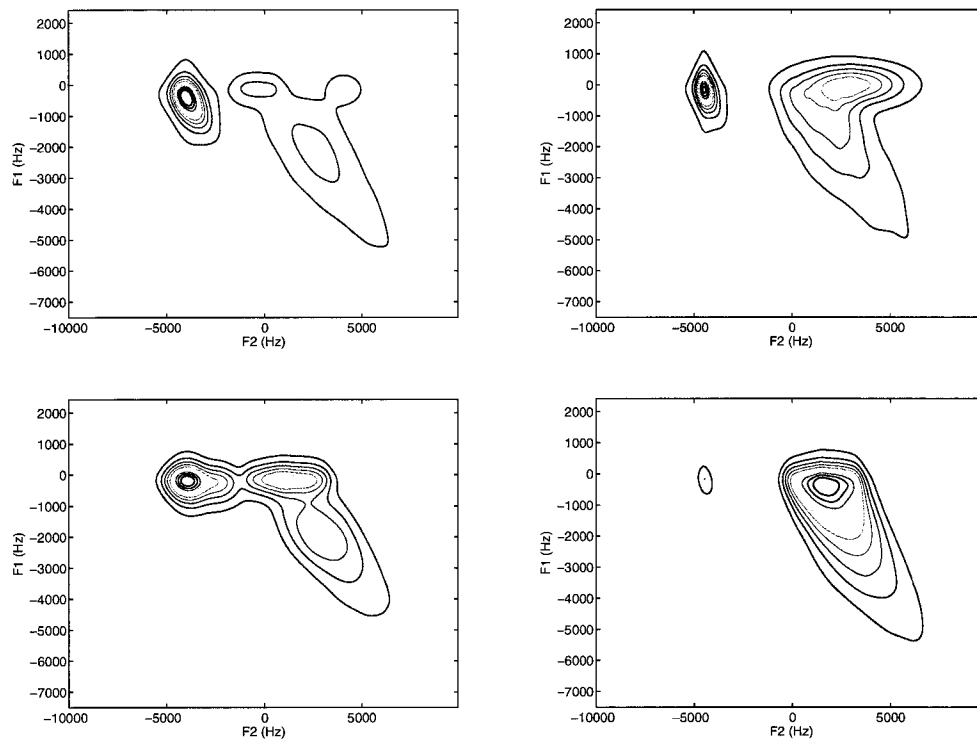


FIG. 5.17: Simulation of $(1-x)$ PSW- x PZ 3QMAS spectra, 19.6T. Grid size was 256×128 points, based on 1k samples for each distribution. Clockwise from top left, $x=0$, $x=0.15$ (PT), $x=0.25$ (PT), $x=0.15$ (PZ)

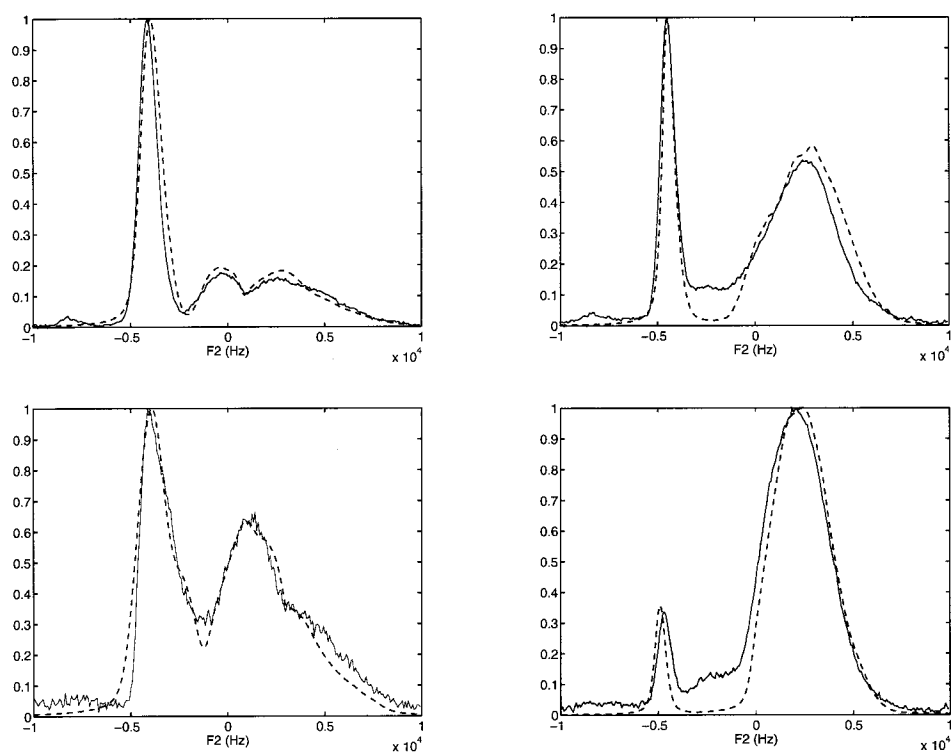


FIG. 5.18: Experimental spectra with simulations (dashed) of $(1-x)\text{PSW}-x\text{PZ}$ 3QMAS spectra, 19.6T, F2 projections. Grid size was 256×128 points, based on 1k samples for each distribution. Clockwise from top left, $x=0$, $x=0.15$ (PT), $x=0.25$ (PT), $x=0.15$ (PZ)

TABLE 5.6: Parameter distributions for solid solutions $(1-x)$ PSW- x PZ/PT

Compound	Site No.	C_Q (MHz)	η	ω_{iso} (Hz)	Line brd. (Hz)
PSW	1	4.4 ± 3	0.9	-4800 ± 500	350
	2	3.6 ± 2.3	0.1	-500 ± 1200	"
	4	12.4 ± 4.2	0.1	1000 ± 1800	"
0.85PSW-0.15PT	1	5.6 ± 3.2	0.9	-4800 ± 500	"
	2	4.2 ± 1.1	0.1	1100 ± 2000	"
	4	12.6 ± 4.7	0.1	900 ± 2000	"
0.75PSW-0.25PT	1	3.7 ± 2	0.1	-5000 ± 140	"
	2	4.2 ± 1.1	0.1	1100 ± 2000	"
	3	12.6 ± 4.7	0.1	900 ± 2000	"
0.85PSW-0.15PZ	1	6.0 ± 3.1	0.9	-4000 ± 700	"
	2	6.7 ± 3.3	0.9	-3700 ± 600	"
	3/4	4 ± 3	0	1000 ± 1800	"
	5	17 ± 6	0	1600 ± 1800	"

5.4.1 Calculations

The electronegativity differences between constituent ions supports a point charge approximation based on largely ionic bonding, with the exception of Pb-O bonds. MATLAB/OCTAVE scripts were written to produce bravais lattice points for arbitrary solid solution concentrations and models for ordering along [1,1,1]. Using the values for stoichiometry, and an average value of 2.0 Angstroms for the O-Sc bond length with assumed overall cubic symmetry, initial lattice coordinates were generated for the PSW solid solution series. Oxygen octahedra were then rotated 0.2 radians in the $a^0b^-b^-$ Glazer system (figure 5.19). In other words, rotations of the same magnitude occur about the y and z axes, out of phase between respective octahedra along either axis. No rotation takes place about the x axis.

For each solution (PT/PZ) B atoms were diffused up to 0.1 Angstroms along the major oxygen octahedra axis in 0.85PSW-0.15PT, and diffused randomly in

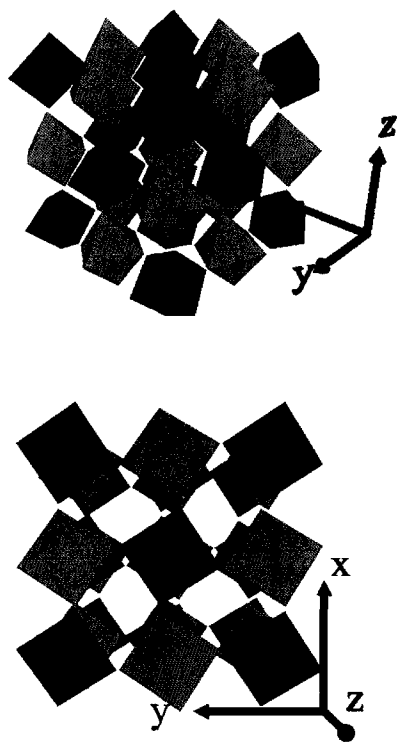


FIG. 5.19: Space group $Im\bar{m}a$, with tilt system $a^0b^-b^-$ and 1:1 order along $[1,1,1]$. Red and green octahedra illustrate the different species on the B-site.

direction within 0.85PSW-0.15PZ, with the same magnitude. For each scandium ion, quadrupole coupling constants were calculated. Distributions for these solutions are presented in figure 5.20. As can be appreciated from the distribution for 0.85PSW-0.15PT, the ranges for C_Q obey a Gamma function but are fairly smooth. This is reflected in almost singular values for the β' and β'' ordered site quadrupole coupling constants extracted via simulation. However, the distribution in C_Q for 0.85PSW-0.15PZ becomes bi-modal for both sites, again reflected in the experimental values. Random site unit cells (β') were given B-O bond lengths which were on average 1.18 times the length of β'' B-O bond lengths. The value was slightly higher for PSW-PZ (1.2) and slightly less for PSW-PT (1.15) than pure PSW (1.18), again chosen to reflect the experimental distributions. While not quantitative, the distribution profiles reveal the importance of the steric effects on the random site. This difference between β'' and β' site atom cells has a marked effect also on lead displacement. The point charge interaction energy between a central lead atom and the first two shells composed of twelve oxygen and six B atoms respectively, was calculated. Referring figure 5.21, there is now a distinction between the two energy minima signifying the specific displacement along $[-1, 0, 0]$. Figure 13 also displays a plot of interaction energy versus x and y coordinates for lead in a distorted PSW perovskite lattice, using rotation system $a^0b^-b^-$ and ratio of 1:1.18 for $\beta'' : \beta'$ site B-O bond lengths, for pure PSW. For all lead atoms investigated, the energy difference between $[1, 0, 0]$ and $[-1, 0, 0]$ is often as much as 20%. It should be stressed that this calculation is not converged or quantitative, but clearly demonstrates the relationship between steric effects on the random site and the macroscopic polarization. As before these displacements are heavily correlated with the oxygen rotations and in turn rotations are necessary in perovskites due to steric differences between oxygen and B site

atoms. Ultimately, confirmation of these results will be supported either by more exacting ab-initio calculations for these disordered materials, or more quantitative NMR. It is anticipated that correlations may in time be developed between NMR parameters and structural information from simple crystalline compounds, for scandium. However, the ultimate limitation remains the lack of resolution and we revisit finally the enticing possibility of a three dimensional experiment, to hopefully provide a method for extracting independent parameter distributions.

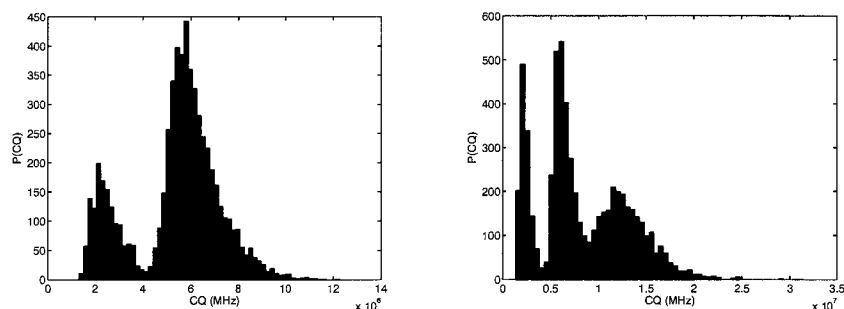


FIG. 5.20: Calculated C_Q distribution for 0.85PSW-0.15PT (left), and 0.85PSW-0.15PZ (right)

5.5 Three Dimensional, Multiple Quantum MAS

Referring to figure 5.23 reproduced from section 2, a practical implementation of the pulse sequence must sufficiently filter both double and triple quantum transitions. Pulse block 1 consists of an hard excitation pulse, followed by a π pulse selective on the central transition. The π pulse inverts the central transition, as well as converting coherences $1 \rightarrow 2$. Block 2 comprises the double to triple quantum conversion step, using a hard pulse followed by a $\pi/2$ pulse selective on

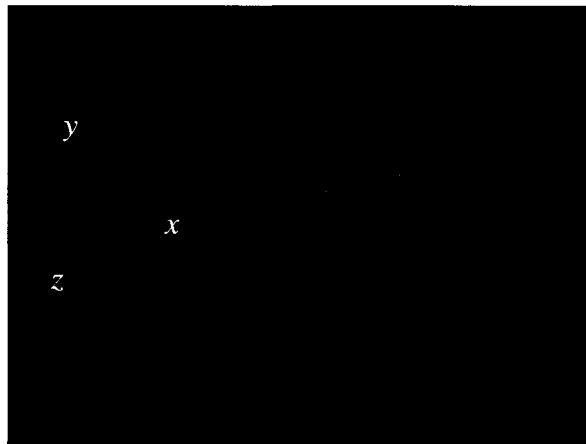
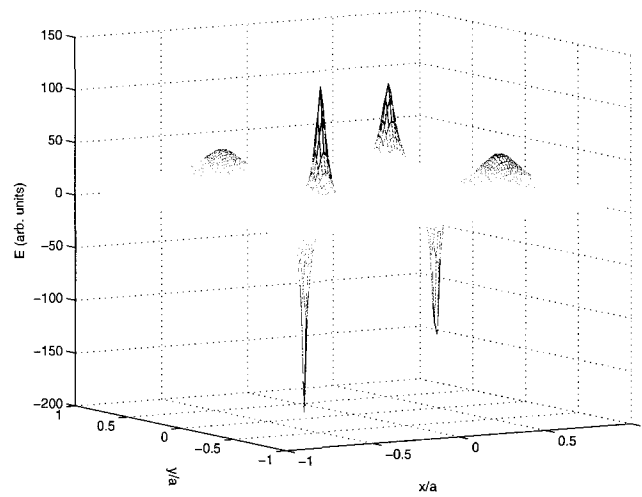


FIG. 5.21: (Top) Plot of interaction energy versus x and y coordinates for lead in a distorted PSW perovskite lattice, using rotation system $a^0b^-b^-$ and ratio of 1:1.2 for $\beta'' : \beta'$ site B-O bond lengths in the RS model. For a variety of Pb sites surveyed, a displacement along $[-1,0,0]$ appears preferable and the minima for the energy is deeper than a more ferroelectric counterpart such as PST, without random sites. (Bottom) Rendering of the distorted 3D oxygen polyhedra around lead for the same assumptions.

the central transition. Owing to typical degeneracies in the nested-phase cycle approach, diagonal cross peaks cannot be removed on the basis of conventional phase cycling alone. The soft pulse as before helps remove unwanted contributions by manipulating the central transition and low quantum coherence orders. Table 5.8 gives a phase cycle for cosine and sine acquisition for reconstruction of pure phase absorption spectra in the hyper-complex scheme. Figure 5.22 is a representation of the acquired signal(s) for all four quadrants, S_{xx} , S_{xy} , S_{yx} and S_{yy} .

TABLE 5.7: Phase cycle for 3D-MQMAS experiment

p1/p2	$\phi_1 =$	(8) 0 2 4 6
p3/p4	$\phi_2 =$	{0}*4 {2}*4
p5	$\phi_3 =$	(6) {0}*8 {1}*8 {2}*8 {3}*8 {4}*8 {5}*8
p6	$\phi_4 =$	0
	$\phi_r =$	$-2 * \phi_1 - \phi_2 + 3 * \phi_3$

RbNO₃ was obtained from Alpha Aesar and used without further purification. Experiments were performed on a Bruker Avance 750, with MAS spinning speed 8 kHz. The $\pi/2$ pulse was found to be 11.5 μ s at 24dB and the following values were used after some experimental optimization: $p1 = 4.4\mu$ s, $p2 = 23\mu$ s, $p3 = 5.4\mu$ s, $p4 = 11.5\mu$ s, $p5 = 3.4\mu$ s, $p6 = 11.5\mu$ s. The hard pulse power level was 6dB and the z-filter (τ_z) and recycle delay 10 μ s 200 ms respectively. Other delays (τ) were 2 μ s. The spectral bandwidth was 8 kHz in each dimension, with initial inter-pulse delays also rotor synchronized. Figure 5.24 displays an isosurfaces of the data in three dimensions, after data processing using MATLAB scripts and functions (Appendix C). Shearing factors of $k_1 = 0$ and $k_2 = -7/9$ were used, and data points were scaled to produce $64 \times 64 \times 64$ in $F1$, $F2$ and $F3$ dimensions. Figure 5.25 is a high resolution projection of the $F1/F2$ dimensions, devoid of anisotropy. This spectrum is the first of it's kind, however frequencies in both

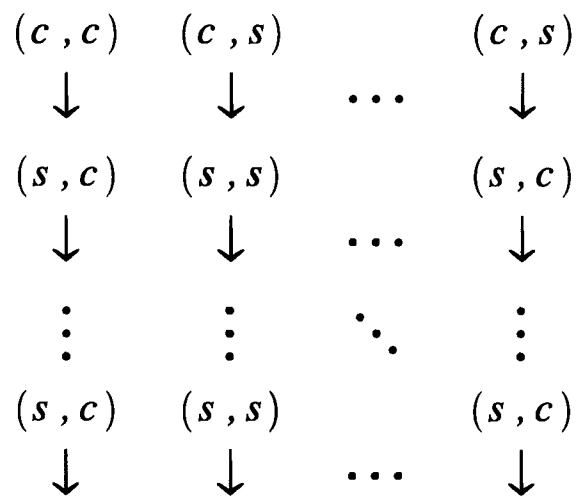


FIG. 5.22: Model for acquisition and separation of all four quadrants, $S_{xx} = (c, c)$, $S_{xy} = (c, s)$, $S_{yx} = (s, c)$ and $S_{yy} = (ss)$. Arrows correspond to fid's; there are t_1/n increments along columns of length n and t_2/m increments along rows of length m . Fourier transform of all matrix 'elements' produces F3 and combination of columns or rows in the States method reproduces phase signals for t_2 and t_1 respectively.

isotropic dimensions are linearly dependent. Each frequency is a function of two variables, and therefore in this form interactions may not be treated independently. Unfortunately, the re-introduction of tensor terms eliminated by MAS does not lift this degeneracy. It may be though that for large C_Q , third order effects are sufficient to create linear independence. Alternatively, if the effects of second order quadrupole broadening could be removed whilst reintroducing the first order contribution on the satellite transition, then this also has the potential for producing a linearly independent set. This may be achieved in practice by off-angle Dynamic Angle Spinning (DAS), although remains to be verified experimentally.

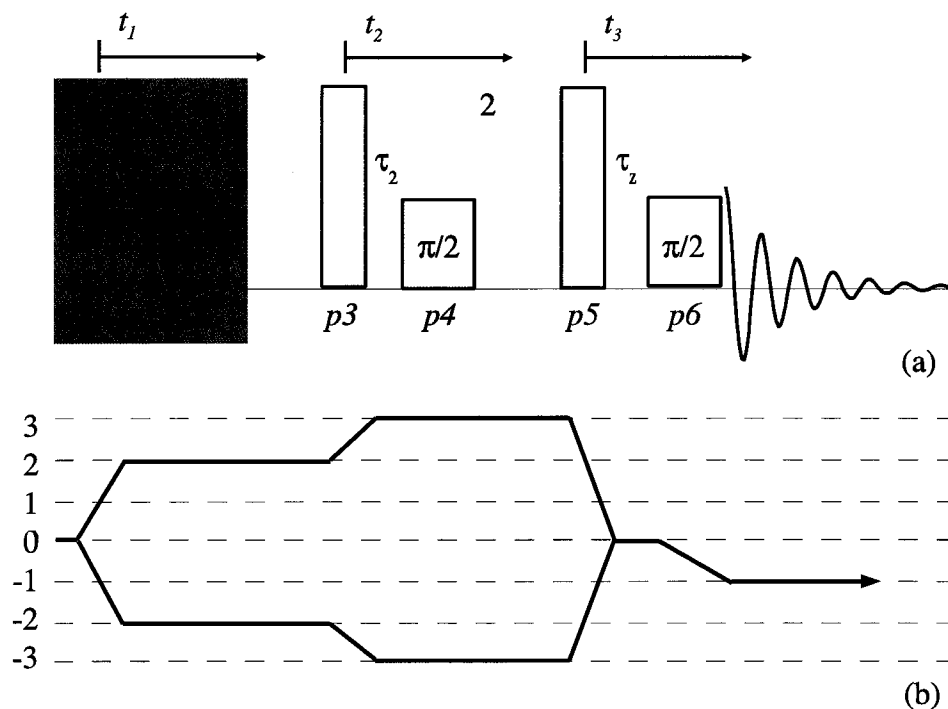


FIG. 5.23: (a) Three dimensional multiple quantum MAS experiment, based on the scheme suggested by Donghua Zhou. Pulse block 1 represents a double quantum filter and pulse block 2 a triple quantum filter. Pulse five and delay τ_z comprise the z-filter, with a selective 90 degree pulse for detection. (b) Coherence transfer pathway for 3D-MQMAS

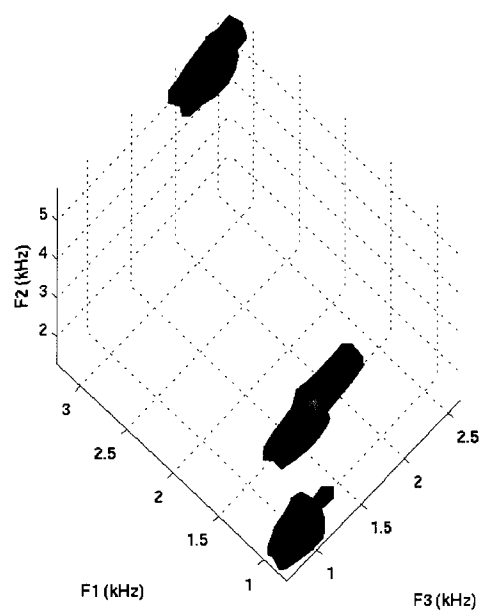


FIG. 5.24: Three dimensional MQMAS of Rubidium Nitrate, displaying the three chemically distinct sites. Single, double and triple quantum frequencies are F3, F1 and F2 respectively and isosurface is drawn at 40% of maximum value.

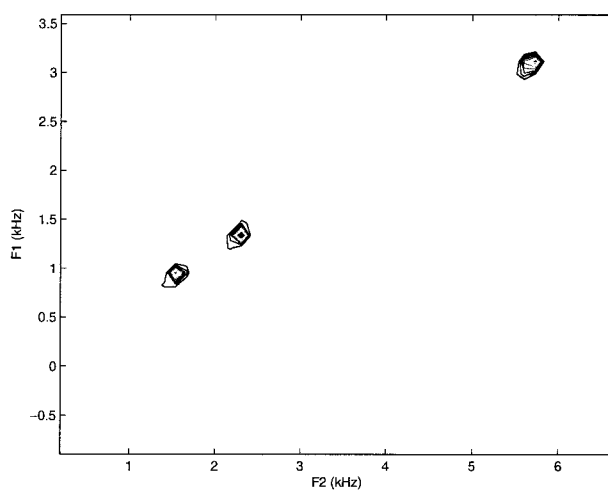


FIG. 5.25: High resolution contour plot of double (F1) and triple (F2) quantum frequency dimensions, devoid of anisotropy. Ten contours are drawn in linear increments from 20 to 95 %.

Chapter 6

Conclusions

Solid solutions perovskites $(1-x)\text{PSW}-(x)\text{PT}$, $(1-x)\text{PSW}-(x)\text{PZ}$ and PST have been studied via ^{45}Sc NMR experiments. Order in the PSW solid solutions series are known to obey the Random Site model. Pure layers of Scandium are interleaved with layers containing mixtures of the remaining ions, along $[1,1,1]$ in a 1:1 ratio. Ordered PST contrasts to the PSW series; having been subjected to high temperature annealing, it consists of ordered Sc,Ta planes and does not display the relaxor behavior of the PSW based solutions. It was noted during initial MAS experiments on the PSW series that NMR lineshapes lacked resolution. In order to interpret these and 3QMAS results, particularly for the relaxors, approximate methods were devised to calculate NMR parameters. The electronegativity differences between constituent ions supports a point charge approximation based on largely ionic bonding, with the exception of Pb-O bonds. MATLAB/OCTAVE scripts were written to produce bravais lattice points for arbitrary solid solution concentrations and models for ordering along $[1,1,1]$. In addition, static distortions including oxygen octahedra rotations were introduced, as well as B and A

site displacements and statistics for nearest B-site neighbors are readily available. Distributions of the Quadrupole coupling constant C_Q and asymmetry parameter η are made available by calculating the five independent EFG tensor components at each Scandium ion, and converting to the principle axis system by finding the eigenvalues for the EFG. The method of Cardan provides an elegant means to find the three real roots of the determinantal equation. It was observed that the distribution in asymmetry was very narrow and a single value was sufficient for the purposes of simulation. The quadrupole coupling constant displayed a gamma like distribution and this may be easily understood on the basis of the distance variate taking on a Poissonian character due to structural disorder. In this case, the electric field gradient and associated quantities may be modeled as gamma function distributions.

An approximate means for generating isotropic chemical shift distributions was devised. The Rayleigh Ritz principle was used to minimize the interaction energy between a p type valence electron of scandium and the surrounding charge distribution. In a one-electron approximation (ignoring correlation, exchange, core effects etc) the resulting wave function was used to estimate the diamagnetic chemical shift. Using large cells convergence is reached easily for EFG calculations, without the need for Ewald summation. The chemical shift distribution calculation is divergent; at this stage an exact model for the distribution is still unknown as well as the form of the correlation between it and the quadrupole coupling constant distribution.

Nonetheless, the quadrupole coupling constant distributions and their moments display a pleasing sensitivity to structural distortions and chemical disorder. It has been determined that the narrow peak in a 1:1 ordered material corresponds to scandium on a random plane, whose nBn shell for low concentration x are all

Sc. The broad overlapping peak(s) correspond to scandium on pure planes, for low x , where the nBn shell is randomly composed. For $x > 0.25$, both planes are randomly composed. Assuming a space group symmetry of $Imma$, pure PSW appears to have a large tilt angle (≈ 15 degs) versus PST (≈ 5 degs). In addition, the random site B atom appears to have a B-O bonding distance which is on average 1.18 times larger than the B-O bond length in the pure layer. Introduction of titanium (via PT) which has similar radius to tungsten, preserves order up until the morphotropic phase boundary at $x \approx 0.25$. Beyond this point, the random site B atom has on average a B-O bond length which is approximately 1.2 times as large. Introduction of zirconium (via PZ) which has similar radius to scandium immediately contributes to significant disorder. For concentrations as low as $x=0.15$, the random site B-O bond length is at least 1.2 times as large as the B-O bond length in the pure layer. While the degree of relaxor behavior is also a function of the degree of thermal annealing, the size mismatch on the RS appears the most prosaic. It is observed that the dielectric constant maxima versus temperature increase linearly with x for PSW-PZ, but is negative in slope until $x=0.25$ for PSW-PT, after which point it has positive slope. Direction specific lead displacement is evident in the Relaxors, where B-O bond length difference, as well as significant B-site off-centering along $[1,1,1]$ create this environment. Calculations also suggest that the broad relaxor phase transition is associated with a significant tilting distortion, which is promoted with concentration x in PSW-PZ. It is assumed that this is closely tied to the similarity in local symmetry in the PSW and PZ subsystems where the dominant B site ions have the same size. In contrast, PSW-PT is composed of a larger degree of ionic mismatch (lower temperature is required to produce comparable tilting) up until the morphotropic phase boundary. After this point, the overall symmetry is assumed to be (dis-

ordered) PST-like, and the permittivity temperature maximum increases linearly with x . There is also sufficient evidence to support the idea that smaller B- atoms such as niobium and tungsten occupy several off site positions with the oxygen octahedra. In fact, prior ^{93}Nb studies of the PMN-PSN solid solutions reveal several distinct chemical sites, whose chemical shift vary linearly with the number of larger magnesium in the surrounding nearest B-site configurations.

Inferences made based on these calculations are supported via NMR lineshape simulation; novel programs were devised to incorporate the Gamma function model for the C_Q distribution. Convergence is difficult using standard random number generators, but the simulated spectra do agree within reason to experimental spectra. The presence of significant parameter distributions in the relaxors motivates the need for an experiment where the various interactions and subsequent parameter distributions may be treated independently. To introduce this degree of objectivity requires further information than available from standard high-resolution two dimensional experiments. In June 2004, Donghua Zhou suggested a three dimensional MQMAS experiment which seeks to distribute the three principle shifts for quadrupolar nuclei along three dimensions. It has the potential to reveal all the desired tensor parameters, since three equations are available for three unknowns. An experiment was devised which has the necessary properties, and software written for the intensive data analysis. Considerable time is required for a 3D experiment, and in the best cases this has translated to 24-48 hours. Time has been spent devising pulse programs with phase cycles which select the appropriate Coherence transfer pathways. It appears that the inherent degeneracy between frequencies may be lifted using a modified form of the Dynamic Angle Spinning technique, although this remains to be experimentally verified.

Appendix A

Elementary Group Theory

In the last century, group theory has been applied with much success to problems concerning eigenstates of the Hamiltonian operator H . A seemingly intractable problem can be reduced in some cases to that which is easily assimilated and solved. This usually involves a consideration of the symmetry of H and subsequent application of group theory. The idea of symmetry and group theoretic principles applied to atomic structure allows an ambiguous assignment of atoms using a modicum of symbols.

An abstract group \mathcal{G} is considered to be that set of elements A, B, \dots such that group multiplication is defined, so as to associate a third element with any ordered pair. More concisely, an abstract group is composed of elements which satisfy:

1. The product of any two elements is in the set; i.e., the set is closed under multiplication.
2. Association holds; $A(BC) = (AB)C$.
3. There exists a unit element E ; $AE = EA = A$.

4. An inverse exists for each element; $AA^{-1} = A^{-1}A = E$

The multiplicative relationship between group elements may be represented by a multiplication table. Within that table each row and column contains each element only once. For example the covering operations of the square, group D_4 .

For any group element X one may form the period of X , or cyclic subgroup of

	<i>E</i>	<i>A</i>	<i>B</i>	<i>C</i>	<i>D</i>	<i>F</i>	<i>G</i>	<i>H</i>
<i>E</i>	<i>E</i>	<i>A</i>	<i>B</i>	<i>C</i>	<i>D</i>	<i>F</i>	<i>G</i>	<i>H</i>
<i>A</i>	<i>A</i>	<i>E</i>	<i>G</i>	<i>H</i>	<i>F</i>	<i>D</i>	<i>B</i>	<i>C</i>
<i>B</i>	<i>B</i>	<i>G</i>	<i>E</i>	<i>F</i>	<i>H</i>	<i>C</i>	<i>A</i>	<i>D</i>
<i>C</i>	<i>C</i>	<i>F</i>	<i>H</i>	<i>E</i>	<i>G</i>	<i>A</i>	<i>D</i>	<i>B</i>
<i>D</i>	<i>D</i>	<i>H</i>	<i>F</i>	<i>G</i>	<i>E</i>	<i>B</i>	<i>C</i>	<i>A</i>
<i>F</i>	<i>F</i>	<i>C</i>	<i>D</i>	<i>B</i>	<i>A</i>	<i>G</i>	<i>H</i>	<i>E</i>
<i>G</i>	<i>G</i>	<i>B</i>	<i>A</i>	<i>D</i>	<i>C</i>	<i>H</i>	<i>E</i>	<i>F</i>
<i>H</i>	<i>H</i>	<i>D</i>	<i>C</i>	<i>A</i>	<i>B</i>	<i>E</i>	<i>F</i>	<i>G</i>

TABLE A.1: Proper covering operations of the group D_4 .

order n , defined as:

$$X, X^2, X^3, \dots, X^n = E \tag{A.1}$$

where n is the order of the element X . Groups \mathcal{G} of order h may consist of subgroups $\mathcal{S} = E, S_2, \dots, S_g$ of lower order g , where the order is the number of elements. The set of elements EX, S_2X, \dots, S_GX is a right co set $\mathcal{S}X$ if X is not in \mathcal{S} . A left co set may be similarly defined. Co-sets don't constitute subgroups since the identity is absent. Further, one may show that left and right co sets of a subgroup are either identical or have no elements in common.

Elements are said to be conjugate if for instance:

$$B = XAX^{-1} \text{ or } A = X^{-1}BX \tag{A.2}$$

where X is a member of the group. The arrangement of mutually conjugate elements constitutes a class, \mathcal{C} . For example D_4 has classes

$$\{A, B\}, \{C, D\}, \{F, H\}, \{G\}, \{E\}$$

. Physically speaking, class elements may be rotations of the same angle(s) performed about different axes, related by a group operation. If a subgroup consists entirely of classes, then it is referred to as an invariant subgroup or normal divisor. For instance, within D_4 there exists the following subgroups which are also normal divisors:

$$\{A, B, G, E\}; \{C, D, G, E\}; \{F, G, H, E\} \quad (\text{A.3})$$

In general one is more concerned with *representations* Γ of group elements, isomorphic to the original group. This simply means that (for instance) one selects a group of square matrices whose multiplication properties are identical to the original abstract group. The dimensionality of a representation refers to the number of rows/columns, and if the representation is larger in dimension than needed to illicit the same properties, it is said to be *reducible*. Any representation by matrices with non-vanishing determinants is equivalent via a similarity transformation to a representation by unitary matrices. Schur's lemma gives a test of reducibility; if a (non-constant) commuting matrix exists for a any representation, then it is reducible. Stated another way, only a constant matrix commutes with an irreducible representation. Further, given two irreducible representations of the same group $\Gamma^{(1)}(A_i)$ and $\Gamma^{(2)}(A_i)$ of dimensionality l_1 and l_2 and if a rectangular matrix M exists such that

$$M\Gamma^{(1)}(A_i) = \Gamma^{(2)}(A_i)M \quad i = 1, 2, \dots, h \quad (\text{A.4})$$

then either:

1. $l_1 \neq l_2$ and $M = 0$, or
2. $l_1 = l_2$ and $M = 0$, or at least $|M| \neq 0$, in which case M has an inverse and the representations are identical.

The previous results for matrices, representations are implicit to the great orthogonality theorem, which for all the inequivalent, irreducible, unitary representations of a group states that:

$$\sum_R \Gamma^{(i)}(R)_{\mu\nu}^* \Gamma^{(j)}(R)_{\alpha\beta} = \frac{h}{l_i} \delta_{ij} \delta_{\mu\alpha} \delta_{\nu\beta} \quad (\text{A.5})$$

where R covers all group elements and l_i is the dimensionality of $\Gamma^{(i)}$. This result may be used to give the dimensionality theorem:

$$\sum_i l_i^2 = h \quad (\text{A.6})$$

Simply put, the sum of the squares of the irreducible representation's dimensions is equal to the order h of the group.

Since all matrices related to one another through unitary transformations are equivalent, an invariant to said transformation is often used, hence the *character* χ of a representation. The invariant quantity is the trace of a matrix; the character of the j th representation is the set of h numbers $\chi^{(j)}(E), \chi^{(j)}(A_2), \dots, \chi^{(j)}(A_h)$, where

$$\chi^{(j)}(R) = \text{Tr} \Gamma^{(j)}(R) = \sum_{\mu=1}^{l_j} \Gamma^{(j)}(R)_{\mu\mu} \quad (\text{A.7})$$

Naturally, all class members have the same character,

A.0.1 Angular Momentum

The addition of angular momentum may be in the simplest case simply the addition of spin and orbital angular momentum, or more typically the combination of one or more spins. Consider to begin with the addition of two angular momenta j_1 and j_2 with eigenfunctions $\psi_{j_1 m_1}$ and $\psi_{j_2 m_2}$. Then

$$\begin{aligned} J_1^2 \psi_{j_1 m_1} &= j_1(j_1 + 1) \psi_{j_1 m_1}; & J_2^2 \psi_{j_2 m_2} &= j_2(j_2 + 1) \psi_{j_2 m_2} \\ J_{1z} \psi_{j_1 m_1} &= m_1 \psi_{j_1 m_1}; & J_{2z} \psi_{j_2 m_2} &= m_2 \psi_{j_2 m_2} \end{aligned} \quad (\text{A.8})$$

The direct product $\psi_{j_1 m_1} \psi_{j_2 m_2}$ is referred to as the uncoupled representation, in which $J_1^2, J_{1z}, J_2^2, J_{2z}$ are diagonal. The total angular momentum operator J is defined by

$$J = J_1 + J_2 \quad (\text{A.9})$$

We seek the coupled representation where J^2, J_z, J_1^2 and J_2^2 are diagonal with eigenvalues $j(j + 1)$ and m respectively. The two representations are connected by a unitary transformation through:

$$\psi_{jm} = \sum_{m_1 m_2} C(j_1 j_2 j; m_1 m_2 m) \psi_{j_1 m_1} \psi_{j_2 m_2} \quad (\text{A.10})$$

The elements $C(\dots)$ comprise the Clebsch-Gordon coefficients. A simple manipulation shows:

$$(m - m_1 - m_2) C(j_1 j_2 j; m_1 m_2 m) = 0 \quad (\text{A.11})$$

Which implies that $m = m_1 + m_2$ or else $C(j_1 j_2 j; m_1 m_2 m) = 0$; further

$$|j_1 - j_2| \leq j \leq |j_1 + j_2| \quad (\text{A.12})$$

again, else $C(j_1 j_2 j_3; m_1, m - m_1) = 0$. The $C.C.$ coefficients obey various symmetry relations, including:

$$\begin{aligned}
C(j_1 j_2 j_3; m_1 m_2 m_3) &= (-1)^{j_1 + j_2 - j_3} C(j_1 j_2 j_3; -m_1, -m_2, -m_3) \\
&= (-1)^{j_1 + j_2 - j_3} C(j_2 j_1 j_3; m_2 m_1 m_3) \\
&= (-1)^{j_1 - m_1} \left(\frac{2j_3 + 1}{2j_2 + 1} \right)^{\frac{1}{2}} C(j_1 j_3 j_2; m_1, -m_3, m_2) \quad (A.13)
\end{aligned}$$

with $j_3 = j$; $m_3 = m$. There exists various expressions for the co-efficients, Racah's the most popular:

$$\begin{aligned}
C(j_1 j_2 j_3; m_1 m_2 m_3) &= \delta_{m_3, m_1 + m_2} \\
&\times \left[(2j_3 + 1) \frac{(j_1 + j_2 - j_3)! (j_3 + j_1 - j_2)! (j_3 + j_2 - j_1)!}{(j_1 + j_2 + j_3 + 1)!} \right. \\
&\times (j_1 + m_1)! (j_1 - m_1)! (j_2 + m_2)! (j_2 - m_2)! (j_3 + m_3)! (j_3 - m_3)! \left. \right]^{\frac{1}{2}} \\
&\times \sum_{\nu} \frac{(-1)^{\nu}}{\nu!} [(j_1 + j_2 - j_3 - \nu)! (j_1 - m_1 - \nu)! (j_2 + m_2 - \nu)! \\
&\times (j_3 - j_2 + m_1 + \nu)! (j_3 - j_1 - m_2 + \nu)!]^{-1} \quad (A.14)
\end{aligned}$$

Recurrence relation:

Central to the quantum processes taking place at the heart of NMR is the rotation of some quantization axis. Under these conditions, simple considerations show that the square of the angular momentum operator remains unchanged. The eigenfunctions ψ_{jm} which diagonalize both J^2 and J_z transform as

$$R\psi_{jm} = e^{-i\theta(\mathbf{n}\cdot\mathbf{J})}\psi_{jm} \quad (A.15)$$

In the simplest case a rotation takes place around the transformation axis such

that $\mathbf{n} \cdot \mathbf{J} = J_z$, hence

$$\langle jm' | e^{-\theta(\mathbf{n} \cdot \mathbf{J})} | jm \rangle = \delta_{m'm} e^{-im\theta} \quad (\text{A.16})$$

hence there is a change of phase between one function and another:

$$R\psi_{jm} = e^{-im\theta}\psi_{jm} \quad (\text{A.17})$$

In the quest for the matrix elements of the rotation matrix, one is inclined to consider the most general specification for a rotation, cast in terms of the *Euler Angles*, α, β, γ , specified as follows (after Rose):

1. A rotation is made about the z -axis through an angle α ; the new coordinate axes are x', y', z' .
2. A rotation is made about the y' -axis through an angle β ; the new coordinate axes are x'', y'', z''
3. A rotation is made about the z'' -axis through an angle γ ; the new coordinate axes are x''', y''', z'''

Expressed in terms of the original coordinate system, this is:

$$R = e^{-i\alpha J_z} e^{-i\beta J_{y'}} e^{-i\gamma J_{z''}} \quad (\text{A.18})$$

The matrix elements for R :

$$\begin{aligned} D_{m'm}^j(\alpha, \beta, \gamma) &= \langle jm' | e^{-i\alpha J_z} e^{-i\beta J_{y'}} e^{-i\gamma J_{z''}} | jm \rangle \\ &= e^{-im'\alpha} \langle jm' | e^{-i\beta J_{y'}} | jm \rangle e^{-im\gamma} \end{aligned} \quad (\text{A.19})$$

There remains one matrix to be determined, since $\exp(-i\beta J_y)$ is not diagonal in this representation; an expression due to Wigner:

$$\begin{aligned}
 d_{m'm}^j(\beta) &= \langle jm' | e^{-i\beta J_y} | jm \rangle \\
 &= [(j+m)!(j-m)!(j+m')!(j-m')!]^{\frac{1}{2}} \\
 &\times \sum_{\nu} \frac{(-1)^{\nu}}{(j-m'-\nu)!(j+m-\nu)!(\nu+m'-m)!\nu!} \\
 &\times \left(\cos \frac{\beta}{2} \right)^{2j+m-m'-2\nu} \left(-\sin \frac{\beta}{2} \right)^{m'-m+2\nu}
 \end{aligned} \tag{A.20}$$

The rotation matrices obey orthonormality;

$$\begin{aligned}
 \sum_m D_{m'm}^{j*}(\alpha\beta\gamma) D_{m''m}^j(\alpha\beta\gamma) &= \delta_{m'm''} \\
 \sum_m D_{mm'}^{j*}(\alpha\beta\gamma) D_{mm''}^j(\alpha\beta\gamma) &= \delta_{m'm''}
 \end{aligned} \tag{A.21}$$

An irreducible tensor of rank L is defined as a set of $2L+1$ functions $T_{LM}(M+L, M+L-1, \dots, M-L)$ which transform under the $2L+1$ -dimensional representation of the rotation group:

$$RT_{LM}^{-1} = \sum_{M'} D_{M'M}^L(\alpha\beta\gamma) T_{LM'} \tag{A.22}$$

Appendix B

Data Processing

The following discussion gives the salient features of subsequent data processing after acquisition, using MATLAB/OCTAVE functions to perform the manipulations. Generally speaking, the data filename for data acquired on a Bruker Avance console is either `fid` or `ser` depending on whether the data is one dimension or multi-dimensional, respectively. To open up a datafile, the file type is `int32` and is for instance the machine used to acquire the data uses UNIX or big-endian byte ordering;

```
fid=fopen('fid',r,'ieee-be');  
[A,count]=fread(fid,Inf,int32);
```

The string `fid` is the filename and the integer `fid` is the file ID. Data is stored in variable `A`, and the number of elements is `count`. Now the acquisition is usually of the form `real`, `imag`, `real` ... in which case one can reassemble the data with the commands:

```
for j=0:(count/2-1);  
w(j+1)=A(2*j+1)+i*A(2*j+2)
```

```
end
```

At this point, it is usually prudent to study the FID to see if early points have been distorted by for instance the probe ring down. These x points are removed by performing a left shift:

```
w=w(x:count/2);
```

The effects of noise or inadvertent apodization of the signal may be reduced by zero filling (simply padding the dataset with zeros, usually to a power of 2) and exponential multiplication. Other data windows may be used, for instance sine bell or Gaussian.

```
x=0:dw:(count-1)*dw;
```

```
w=w.*exp(-x.*lb);
```

where lb is the exponential line broadening in hertz and dw is the dwell time. Following these steps, a Fourier transform is taken, using the FFT [46] algorithm:

```
z=fftshift(fft(z,1024));
```

```
f=-(512:511)/(1024*dw);
```

In this example the argument to `fft` transforms the data, which is padded with zeros to 1024 points. The command `fftshift` is necessary since by convention the zero frequency point is in the middle of the spectra, indicated in the construction of the frequency axis data f . Typically the frequency data is a mix of absorption and dispersion components. A linear phase correction is applied to produce a symmetric, pure absorption spectra for ease of interpretation:

```
z=z.*exp(i*(ph1.*f+ph0));
```

where $ph0$ and $ph1$ are the zeroth and first order phase corrections respectively. At this stage the baseline in the frequency domain is often not flat or worse has significant oscillation. This can be for a variety of reasons, the most prosaic due to a large bandwidth and subsequent loss of early data points due to mechanical

limitations. A simple algorithm can search for the minima in the baseline, a result of the convolution between the desired signal and early truncation. Subsequently a fitted polynomial is subtracted leaving the desired information. After data has been adequately processed it may be examined by a variety of means. In the simplest cases, the frequency of a single peak (for instance from a high resolution liquid's spectra) may give sufficient information. However in Solid State NMR, the frequency spectra are usually complex functions of the interactions discussed thus far, and simulation is necessary in order to extract the useful information.

Appendix C

Computer Programs

```
/* two_q2_g.c; Calculate 2D lineshape, k=?, I=7/2, for Cq and
cs distributions, multiple sites.
GNU GPL. NO GUARANTEES OF FITNESS FOR USE, WARRANTIES IMPLIED
OR GIVEN.
WJB 06/04,01/05, 03/05 */
#include <stdio.h>
#include <stdlib.h>
#include <math.h>
/*variable decs;
loop counters */
int h;
int i;
int j;
int k;
int l;
```

```
/* angle space */
int m;
double tt;
/* n samples cs/cq space */
int n;
/* dimensions f1/f2 */
int p;
int q;
/* no. sites*/
int s;
int r;
int M;
int N;
/*input parameters */
double *a_ptr;
double lm;
double dw;
double du;
double w;
double u;
double kk;
/* angles, functions etc */
double a;
double b;
double *fab_ptr;
double *fib_ptr;
```

```
double wcs;
double wcq;
/* axes */
double *f1_ptr;
double *f2_ptr;
double *qcc_ptr;
double *cs_ptr;
/*spectral distributions, output */
double *fn_ptr;
double *s_ptr;
double cs;
double qcc;
double f2m;
double f1m;
double nuq;
double nm;
double alp;
double ww;
/*function decs*/
int FileOfDoublesSize(FILE *fin);
void ErrorMessage(char *str);
double *BinRead(FILE *fin, int n);
void DispVector(double *ptr, int n);
void FileWrite(FILE *fout, double *ptr, int t);
double *Fib(int r);
double Gam(int n);
```

```

int Mod(int g, int gg);

int main()
{
FILE *fptr1, *fptr2, *fptr3;
char filename1[]="input.bin";
char filename2[]="output.bin";
char filename3[]="samples.bin";
if ((fptr1 = fopen(filename1, "r+b")) == NULL){
ErrorMessage(filename1);
}
else if ((fptr2 = fopen(filename2, "r+b")) == NULL) {
ErrorMessage(filename2);
}
else if ((fptr3 = fopen(filename3, "r+b")) == NULL) {
ErrorMessage(filename3);
}
else {
m=FileOfDoublesSize(fptr1);
/* no. sites */
s=floor((m-9)/9);
a_ptr = BinRead(fptr1,m);
printf("No. of sites: %i\n",s);
/* Initialize */
lm=(a_ptr);
m=(int) *(a_ptr+1);
n=(int) *(a_ptr+2);
}
}

```

```
p=(int) *(a_ptr+3);
q=(int) *(a_ptr+4);
dw=(a_ptr+5);
du=(a_ptr+6);
w=(a_ptr+7);
u=(a_ptr+8);
/* Safety features */
if(m > 20){
m=20;
}
if(p > 1024){
p=1024;
}
if(q > 1024){
q=1024;
}
if(n > 1024){
n=4096;
}
f2_ptr=malloc(p*sizeof(double));
f1_ptr=malloc(q*sizeof(double));
fn_ptr=malloc(p*q*sizeof(double));
s_ptr=malloc(3*s*n*sizeof(double));
f2_ptr=w;
f1_ptr=u;
/* mildly useful output */
```

```

printf("p= %i\n",p);
printf("q= %i\n",q);
printf("m= %i\n",m);
printf("n= %i\n",n);
printf("lm= %e\n",lm);
printf("dw= %f\n",dw);
printf("du= %f\n",du);
printf("w= %f\n",w);
printf("u= %f\n",u);
/* set up freq. axes */
for (i=0;i<p-1;i++){
(f2_ptr+i+1)=*(f2_ptr+i)+dw;
}
for (i=0;i<q-1;i++){
(f1_ptr+i+1)=*(f1_ptr+i)+du*(1+kk);
}
for (i=0;i<(p*q);i++){
(fn_ptr+i)=0;
}
fib_ptr=Fib(20);
M = *(fib_ptr+m-1);
N = *(fib_ptr+m+1);
printf("powder steps: %i\n",N);
/* do for each site */
for (j=0;j<s;j++){
fab_ptr = malloc(N*sizeof(double));

```

```

for (l=0;l<N;l++){
a = 2*M_PI*( (double) (Mod(l*M,N)))/((double) N);
b = acos(1-((2*((double) l)+1)/((double) N)));
(fab_ptr+l) = (1.0/11520.0)*(-54.0-3.0*pow(*(a_ptr+14+9*j),2)+
60.0*(*(a_ptr+14+9*j)*cos(2*a))-(35.0)*pow(*(a_ptr+14+9*j),2)
cos(4.0*a)+(540+30.0*pow(*(a_ptr+14+9*j),2)-480*(*(a_ptr+14+9*j))
cos(2*a)+70*pow(*(a_ptr+14+9*j),2)*cos(4.0*a))*pow(cos(b),2)+
(-630-(35.0)*pow(*(a_ptr+14+9*j),2)+420*(*(a_ptr+14+9*j))*cos(2*a)
-35.0*pow(*(a_ptr+14+9*j),2)*cos(4*a))*pow(cos(b),4));
}
for (k=0;k<n;k++){
if (n==1){
cs = *(a_ptr+9+9*j);
wcs = 1;
qcc = *(a_ptr+11+9*j)+*(a_ptr+12+9*j);
wcq = 1;
}
else { cs = (2.0*(((double) ((double) rand()/((double) RAND_MAX)-0.5))*
(a_ptr+10+9*j)) + *(a_ptr+9+9*j);
qcc = (2.0*(((double) ((double) rand()/((double) RAND_MAX)-0.0))*
sqrt(*(a_ptr+13+9*j))* *(a_ptr+11+9*j)));
wcs = (1/(sqrt(2*M_PI)* *(a_ptr+10+9*j))) *
exp(-pow((cs-*(a_ptr+9+9*j)),2)/(2.0*pow(*(a_ptr+10+9*j),2)));
wcq = pow(qcc,(*(a_ptr+13+9*j)-1.0))*exp(-qcc/(*(a_ptr+11+9*j)))
/(Gam(*(a_ptr+13+9*j))*pow(*(a_ptr+11+9*j),*(a_ptr+13+9*j)));
}
}

```

```

printf("%i,%i,cs = %e\n",j,k,cs);
printf("%i,%i,qcc = %e\n",j,k,qcc+(a_ptr+12+9*j));
printf("weight=%e\n",wcq*wcs);
nuq = 3.0*(qcc+(a_ptr+12+9*j))/42.0;
kk = (double) 3.0;
(s_ptr+j*n+3*k)=qcc+(a_ptr+12+9*j);
(s_ptr+j*n+3*k+1)=cs;
(s_ptr+j*n+3*k+2)=wcs*wcq;
for (i=0;i<p;i++){
for (h=0;h<q;h++){
for (l=0;l<N;l++){
f2m = cs - (2.0 * pow(nuq,2) / (9.0 * lm))*(-(15.0 / 20.0)
(3.0 + pow(*(a_ptr+14+9*j),2)) + 270* *(fab_ptr+l));
f1m = ((3*cs - (2.0 * pow(nuq,2) / (9.0 * lm)) * ((-27.0 / 20.0)
(3.0+pow(*(a_ptr+14+9*j),2)) + 606* *(fab_ptr+l)))) - kk*f2m);
/* Combination L&G*/
(fn_ptr+i*q+h) += 0.8* *(a_ptr+17+9*j)*wcs*wcq / ( *(a_ptr+15+9*j)*
(a_ptr+16+9*j) * 2.0 * M_PI) *exp(-pow((*(f1_ptr+h)-f1m),2)/(2.0*
pow(*(a_ptr+15+9*j),2)))*exp(-pow((*(f2_ptr+i)-f2m),2)/(2.0*
pow(*(a_ptr+16+9*j),2))) +0.2* *(a_ptr+17+9*j)*wcs*wcq* *(a_ptr+15+9*j)/
(pow(*(a_ptr+15+9*j),2)+ pow((*(f1_ptr+h)-f1m),2)) * *(a_ptr+16+9*j)/
(pow(*(a_ptr+16+9*j),2)+ pow((*(f2_ptr+i)-f2m),2)));
}
}
}
}

```

```
}
/* tidy up shop */
free(a_ptr);
free(fib_ptr);
free(fab_ptr);
FileWrite(fp_ptr2, fn_ptr, p*q);
FileWrite(fp_ptr3, s_ptr, 3*n*s);
free(f1_ptr);
free(f2_ptr);
free(fn_ptr);
free(s_ptr);
fclose(fp_ptr1);
fclose(fp_ptr2);
fclose(fp_ptr3);
}
return 0;
}

int FileOfDoublesSize(FILE *fin) {
int z=-1;
double x;
while(!feof(fin)){
fread(&x, sizeof(double), 1, fin);
z++;}
fseek(fin, 0, SEEK_SET);
return z; }

double *BinRead(FILE *fin, int n) {
```

```
double *x_ptr;
x_ptr = malloc(n * sizeof(double));
fread(x_ptr, sizeof(double), n, fin);
fseek(fin, 0, SEEK_SET);
return x_ptr; }

void ErrorMessage(char *str) {
printf("Can't open %s.\n",str);
return; }

void DispVector(double *ptr, int n) {
int i;
for (i=0; i < n; i++){
printf(" %e\n",*( ptr + i)); }
return; }

void FileWrite(FILE *fout, double *ptr, int t) {
fwrite(ptr, sizeof(double), t, fout);
return; }

double *Fib(int r) {
double *f_ptr;
f_ptr=malloc((r+2)*sizeof(double));
f_ptr=0;
(f_ptr+1)=1;
for(i=0;i<r;i++){
(f_ptr+i+2) = *(f_ptr+i+1) + *(f_ptr+i);
}
return f_ptr; }

double Gam(int n){
```

```
if (n <= 1){
return 1; }
else{
return (double) (n-1)*Gam(n-1);
} }
int Mod(int g, int gg){
int yy;
yy= g - gg*floor(g/gg);
return yy;
}
}
% ftx.m; Custom script for 3D-MQMAS WJB 08/05
% Sample: RbNO_3 (87Rb)
% Aq. parameters
% Data Size: 512x72x72 (hypercomplex)
% SWh(F3): 8kHz
% SWh(F2): 8kHz
% SWh(F1): 8kHz
sw1=8e3;
sw2=8e3;
sw3=8e3;
aa=512;
bb=72;
cc=72;
zf3=512;
zf2=64;
```

```
zf1=64;
nspf3=61;
nspf2=-1;
nspf1=-1;
lbf3=30;
lbf2=30;
lbf1=30;
k2=-7/9;
k1=0;
sh2=3000;
sh1=0;
f3ph0=40;
f3ph1=0;
f2ph0=0;
f2ph1=0;
f1ph0=0;
f1ph1=0;
% open raw data (ref. P-237 Bruker Avance proc manual)
fid2=crack('ser',bb);
fid3=zeros(zf3*cc,zf2);
for i=0:cc-1
fid=fid2(i*aa/2+1:(i+1)*aa/2,:);
fid=lsh(fid,nspf3);
pp=1;
%optimize phasing etc;
while (pp==1&& i==1)
```

```

% process F3, construct hypercomplex
spec=ph(swapp(fft(conj(fid),zf3)),f3ph0,f3ph1);
spec=alt(spec');
% process F2
x=0:bb/2-1;
spec=(exp(-lbf2/sw2*x')*ones(1,zf3)).*spec;
spec=lsh(spec,nspf2);
spec=ph(swapp(fft(conj(spec),zf2)),f2ph0,f2ph1);
%shear'n'shift
spec=shear(spec,k2,sw2/sw3);
spec=csl(spec,sh2,sw2);
plot(real(spec));
figure;
plot(real(spec'));
f3ph0=input('f3ph0?');
f3ph1=input('f3ph1?');
f2ph0=input('f2ph0?');
f2ph1=input('f2ph1?');
pp=input('okay?');
end
% process F3, construct hypercomplex
x=0:aa/2-1;
fid=(exp(-lbf3/sw3.*x')*ones(1,bb)).*fid;
spec=ph(swapp(fft(conj(fid),zf3)),f3ph0,f3ph1);
spec=alt(spec');
% apply lorentzian lb F2

```

```

x=0:bb/2-1;
spec=(exp(-lbf2/sw2*x')*ones(1,zf3)).*spec;
% process F2
spec=lsh(spec,nspf2);
spec=ph(swapp(fft(conj(spec),zf2)),f2ph0,f2ph1);
%shear
spec=shear(spec,k2,sw2/sw3);
spec=csl(spec,sh2,sw2);
fid3(i*zf3+1:(i+1)*zf3,:)=spec';
end
% construct axes
ax3=(-zf3/2:zf3/2-1)/zf3*sw3;
ax2=(-zf2/2:zf2/2-1)/zf2*sw2+sh2;
ax1=(-zf1/2:zf1/2-1)/zf1*sw1+sh1;
% do f1 keyboard;
fid3=reshape(fid3',zf3*zf2,cc);
for i=0:zf3-1
fid=fid3(1+i*zf2:(i+1)*zf2,:);
pp=1;
while (i==1&&pp==1)
x=0:cc/2-1;
spec=alt(fid');
spec=(exp(-lbf1/sw1*x')*ones(1,zf2)).*spec;
spec=lsh(spec,nspf1);
spec=ph(swapp(fft(conj(spec),zf1)),f1ph0,f1ph1);
%shear

```

```

%spec=shear(spec,k1,sw1/sw2);
%spec=csl(spec,sh1,sw1);
plot(real(spec));
f1ph0=input('f1ph0?');
f1ph1=input('f1ph1?');
pp=input('okay?');
end
% apply lorentzian lb F1
x=0:cc/2-1;
spec=alt(fid');
spec=(exp(-lbf1/sw1*x')*ones(1,zf2)).*spec;
spec=lsh(spec,nspf1);
spec=ph(swapp(fft(conj(spec),zf1)),f1ph0,f1ph1);
%shear
%spec=shear(spec,k1,sw1/sw2);
fid4(i*zf1+1:(i+1)*zf1,:)=spec;
end
%reduce size for plotting by factor 8
for i=1:zf3/8
for k=1:zf1
for j=1:zf2
fid5((i-1)*zf2+k,j)=fid4(8*(i-1)*zf2+k,j);
end
end
end
clear zf1 zf2 zf3 fid fid2 fid3 f1ph0 f1ph1 f2ph0 f2ph1 f3ph0

```

```

f3ph1 lbf1 lbf2 lbf3 spec sh1 sh2 x aa bb cc i sw1 sw2 sw3 ax1
ax2 ax3 j k;
f_id=fopen('e_output.bin', 'w', 'native');
fwrite(f_id,real(fid5),'double');
fclose(f_id);

; stmqmas.zg pulse progra.

; Based on scheme suggested by D Zhou to GLH/RLV 06/04.

; 2Q/3Q MAS with z-filter, hypercomplex

; CTP = 0 -> +/-2 -> +/-3 -> 0 -> -1

; WJB 06/04, 10/04, 12/04, 02/05, 04/05

#include <Avance.incl>

"d0=(1s*l1/cnst31)-p1/2-p3/2-p2-10u"
"d10=(1s*l2/cnst31)-p3/2-p4/2-10u-p6"

;p111 hard pulse

;p121 soft

;p1 hard 90

;p2 sel 180

;p5,p6 sel 90

;cnst31 spin speed

;d4 z-filter, 3-20u

aqseq 312

1 ze

2 d1

(1u pl11):f1

(2u ph1):f1

2u

```

```

(p1 ph1):f1
(2u pl21):f1
2u
(p2 ph1):f1
d0
(2u pl11):f1
(2u ph3):f1
2u
(p3 ph3):f1
(2u pl21):f1
2u
(p6 ph3):f1
d10
(2u pl11):f1
(2u ph4):f1
2u
(p4 ph4):f1
(1u pl21):f1
(1u ph5):f1
d4
p5 ph5
go=2 ph31
15m mc #0 to 2 F1PH(ip1, id0)
F2PH(rd0& ip3, id10)
exit
ph1 = (8) 0 0 2 2 4 4 6 6

```

$$\text{ph3} = \{0\} * 8 \{2\} * 8$$

$$\text{ph4} = (6) \{0\} * 16 \{1\} * 16 \{2\} * 16 \{3\} * 16 \{4\} * 16 \{5\} * 16$$

$$\text{ph5} = 0$$

$$\text{ph31} = \text{ph4} * 3 - \text{ph1} * 2 - \text{ph3} + \text{ph5}$$

BIBLIOGRAPHY

- [1] *Crystal Physics*. Academic Press, 1965.
- [2] *Modern Quantum Mechanics*. Addison Wesley, 1994.
- [3] A. H. Silver, P. J. Bray. Nuclear Magnetic Resonance Absorption in Glass. I. Nuclear Quadrupole Effects in Boron Oxide, Soda-Boric Oxide, and Borosilicate Glasses. *The Journal of Chemical Physics*, 29:984–990, 1958.
- [4] R. Kumar A. Jerschow. Calculation of coherence pathway selection and cogwheel cycles. *Journal of Magnetic Resonance*, 160:59–64, 2003.
- [5] A. M. Glazer. The classification of tilted octahedra in perovskites. *Acta Crystallographica*, B28:3384–3392, 1972.
- [6] A. Medek, J. S. Harwood, L. Frydman. Multiple-quantum MAS NMR: a new method for the study of quadrupolar nuclei in solids. *Journal of the American Chemical Society*, 117:12779–12787, 1995.
- [7] A. Abragam. *The Principles of Nuclear Magnetism*. Oxford: Clarendon Press, 1962.
- [8] E. Cockayne B. P. Burton. Why $\text{Pb}(\text{B},\text{B}')\text{O}_3$ perovskites disorder at lower temperature than $\text{Ba}(\text{B},\text{B}')\text{O}_3$ perovskites. *Physical Review B*, 60:12542–12545, 1999.
- [9] P. E. Blochl. Projector augmented-wave method. *Physical Review B*, 50:17953–17979, 1994.
- [10] F. Borsa. ³⁹ Nuclear Magnetic Resonance in KMnF_3 and Temperature Dependence of the Generalized Order Parameter. *Physical Review B*, 7:913–917, 1973.
- [11] C. E. Hughes, M. Carravetta, M. H. Levitt. Some conjectures for cogwheel phase cycling. *Journal of Magnetic Resonance*, 167:259–265, 2004.

- [12] H. T. Stokes C. J. Howard. Group-theoretical analysis of octahedral tilting in perovskites. *Acta Crystallographica B*, 54:782–789, 1998.
- [13] C. K. Coogan. Electrostatic field gradients in ionic crystals. *Australian Journal of Chemistry*, 17:1–6, 1963.
- [14] L. E. Cross. Relaxor ferroelectrics. *Ferroelectrics*, 76:241–267, 1987.
- [15] L. E. Cross. Relaxor ferroelectrics: An overview. *Ferroelectrics*, 151:305–320, 1994.
- [16] G. Czjzek. Distribution of nuclear quadrupole splittings of ^{57}Fe in amorphous ferric fluorides: Structural Implications. *Physical Review B*, 25:4908–4910, 1982.
- [17] D. H. Zhou, G. L. Hoatson, R. L. Vold. Local structure in perovskite relaxor ferroelectrics: high resolution ^{93}Nb 3QMAS NMR. *Journal of Magnetic Resonance*, 167:242–252, 2004.
- [18] D. H. Zhou, G. L. Hoatson, R. L. Vold, F. Fayon. Local structure in perovskite relaxor ferroelectrics by ^{207}Pb NMR. *Physical Review B*, 69:134104(10), 2004.
- [19] D. Trumeau J. P. Coutures J. Virlet P. Florian P. J. Grandinetti D. Massiot, B. Touzo. Two-dimensional magic-angle spinning isotropic reconstruction sequences for quadrupolar nuclei. *Solid State Nuclear Magnetic Resonance*, 6:73–83, 1996.
- [20] M. Capron I. King S. Le Calve B. Alonso J-O. Durand B. Bujoli Z. Gan G. Hoatson D. Massiot, F. Fayon. Modelling one- and two-dimensional solid-state nmr spectra. *Magnetic Resonance in Chemistry*, 40:70–76, 2002.
- [21] J. F. Stebbins D. R. Spearing.
- [22] D. M. Grant D. W. Alderman, M. S. Solum. Methods for analyzing spectroscopic lineshapes. nmr solid powder patterns. *Journal of Chemical Physics*, 84:3717–3725, 1986.
- [23] P. K. Davies. Cation ordering in complex perovskites. *Current Opinion in Solid State & Materials Science*, 2000.

- [24] D.J. States, R. A. Haberkorn, D. J. Ruben. A Two-Dimensional Nuclear Overhauser Experiment with Pure Absorption Phase in Four Quadrants. *Journal of Magnetic Resonance*, 48:286–292, 1982.
- [25] E. Cross. Lead-free at last. *Nature*, 432:24–25, 2004.
- [26] R. G. Eades E. R. Andrew, A. Bradbury. Removal of dipolar broadening of nuclear magnetic resonance spectra of solids by specimen rotation. *Nature*, 183:1802–1803, 1959.
- [27] F. Chu, I. M. Reaney, N. Setter. Role of defects in the ferroelectric relaxor lead scandium tantalate. *Journal of the American Ceramic Society*, 78:1947–, 1995.
- [28] F. Chu, N. Setter, A. K. Tagantsev. The spontaneous relaxor-ferroelectric transition of $\text{Pb}(\text{Sc}_{0.5}\text{Ta}_{0.5})\text{O}_3$. *Journal of Applied Physics*, 74:5129–5134, 1993.
- [29] F. Fayon, I. Farnan, C. Bessada, J. Coutres, D. Massiot, J. P. Massiot. Empirical Correlations between ^{207}Pb NMR Chemical Shifts and Structures in Solids. *Journal of the American Chemical Society*, 119:6837–6843, 1997.
- [30] G. Shirane F. Jona. *Ferroelectric Crystals*. Dover, 1993.
- [31] S. G. Louie F. Mauri, B. G. Pfroemer. Ab initio theory of nmr chemical shifts in solids and liquids. *Physical Review Letters*, 77:5300–5303, 1996.
- [32] R. R. Ernst G. Bodenhausen, H. Kogler. Selection of coherence-transfer pathways in nmr pulse experiments. *Journal of Magnetic Resonance*, 58:370–388, 1984.
- [33] G. Czjek, J. Fink, F. Gotz, H. Schmidt, J. M. D. Coey, J-P. Rebouillat, A. Lienard. Atomic coordination and the distribution of electric field gradients in amorphous solids. *Physical Review B*, 23:2513–2530, 1981.
- [34] P. Green G. E. Peterson, P. M. Bridenbaugh. NMR Study of Ferroelectric LiNbO_3 and LiTaO_3 . I. *The Journal of Chemical Physics*, 46:4009–4014, 1967.
- [35] G. L. Hoaston, D. H. Zhou, F. Fayon, D. Massiot, R. L. Vold. ^{93}Nb magic angle spinning NMR study of perovskite relaxor ferroelectrics $(1-x)\text{Pb}(\text{Mg}_{1/3}\text{Nb}_{2/3})\text{O}_3-x\text{Pb}(\text{Sc}_{1/2}\text{Nb}_{1/2})\text{O}_3$. *Physical Review B*, 66:224103(13), 2002.

- [36] Z. Gan. Double-quantum filtered stmas. *Journal of Magnetic Resonance*, 164:369–372, 2003.
- [37] Z. H. Gan. Isotropic NMR Spectra of Half-Integer Quadrupolar Nuclei Using Satellite Transitions and Magic-Angle Spinning. *Journal of the American Chemical Society*, 122:3242–3243, 2000.
- [38] P. J. Grandinetti. Does phase cycling work for nuclei experiencing strong nuclear quadrupolar couplings? *Solid State Nuclear Magnetic Resonance*, 23:1–13, 2003.
- [39] X-W. Zhang H. Gui, B-L. Gu. Order-Disorder Transition in (A'A'')BO₃ and A(B'B'')O₃ Complex Perovskite Crystals. *Journal of the American Ceramic Society*, 79:381–384, 1996.
- [40] J. Bieron, I. P. Grant, C. F. Fischer. Nuclear quadrupole moment of scandium. *Physical Review A*, 56:316–321, 1997.
- [41] J. Cavanagh, J. Titman, J. Keeler. Suppression of uninformative peaks in two-dimensional relayed-NOESY spectra. *Magnetic Resonance in Chemistry*, 26:1093–1096, 1988.
- [42] J. Iniguez, D. Vanderbilt, L. Bellaiche. First principles study of (BiScO₃)_{1-x}(PbTiO₃)_x piezoelectric alloys. *Physical Review B*, 67:224107, 2003.
- [43] J. J. Fitzgerald, S. Prasad, J. Huang, J. S. Shore. Solid State ⁹³Nb NMR and ⁹³Nb Nutation Studies of Polycrystalline Pb(Mg_{1/3}Nb_{2/3})O₃ and (1-x)Pb(Mg_{1/3}Nb_{2/3})O₃/xPbTiO₃ Solid-Solution Relaxor Ferroelectrics. *Journal of the American Chemical Society*, 122:2556–2566, 2000.
- [44] E. J. Baerends J. Poater, E. van Lenthe. Nuclear magnetic resonance chemical shifts with the statistical average of orbital-dependent model potentials in kohn-sham density functional theory. *Journal of Chemical Physics*, 118:8584–8593, 2003.
- [45] M. C. Payne F. Mauri J. R. Yates, C. J. Pickard. Relativistic nuclear magnetic resonance chemical shifts of heavy nuclei with pseudopotentials and the zeroth-order regular approximations. *Journal of Chemical Physics*, 118:5746–5753, 2003.
- [46] J. W. Tukey J. W. Cooley. An algorithm for the machine calculation of complex fourier series. *Mathematics of Computation*, 19:297–301, 1965.

- [47] H. A. Harwig J. W. Weenk. Calculation of electrostatic fields in ionic crystals by a bertaut method. *Journal of the Physical Chemistry of Solids*, 36:783–789, 1975.
- [48] H. A. Harwig J. W. Weenk. Calculation of electrostatic fields in ionic crystals based upon the ewald method. *Journal of the Physical Chemistry of Solids*, 38:1047–1054, 1977.
- [49] P. J. Grandinetti K. E. Vermillion, P. Florian. Relationships between bridging oxygen ^{17}O quadrupolar coupling parameters and structure in alkali silicates. *Journal of Chemical Physics*, 108:7274–7285, 1998.
- [50] J. Padilla L. Bellaiche and David Vanderbilt. Heterovalent and A-atom effects in $\text{A}(\text{B}'\text{B}'')\text{O}_3$ perovskite alloys. *Physical Review B*, 59:1834–1839, 1999.
- [51] L. Bellaiche, D. Vanderbilt. Electrostatic model of atomic ordering in complex perovskite alloys. *Physical Review Letters*, 81:1318–1321, 1998.
- [52] L. Farber, P. K. Davies. Influence of Cation Order on the Dielectric Properties of $\text{Pb}(\text{Mg}_{1/3}\text{Nb}_{2/3})\text{O}_3$ - $\text{Pb}(\text{Sc}_{1/2}\text{Nb}_{1/2})\text{O}_3$ (PMN-PSN) Relaxor Ferroelectrics. *Journal of the American Ceramic Society*, 86:1861–1866, 2003.
- [53] M. Bak, J. T. Rasmussen, N. C. Nielsen. SIMPSON: A General Simulation Program for Solid-State NMR Spectroscopy. *Journal of Magnetic Resonance*, 147:296–330, 2000.
- [54] B. F. Shchegolev E. V. Charnaya M. G. Shelyapina, V. S. Kasperovich. Ab initio cluster calculations of electric field gradients at the transition-metal sites in the ferroelectric LiNbO_3 and LiTaO_3 . *Proceedings of the 15th European Experimental NMR Conference*, 2000.
- [55] C. E. Hughes M. H. Levitt, P. K. Madhu. Cogwheel phase cycling. *Journal of Magnetic Resonance*, 155:300–306, 2002.
- [56] P. M. Woodward M. Lufaso. Prediction of the crystal structures of perovskites using the software program SPuDS. *Acta Crystallographica B*, 57:725–738, 2001.
- [57] J. C. Slater M. M. Saffren. An augmented plane-wave method for the periodic potential problem ii. *Physical Review*, 92:1126–1128, 1953.

- [58] M. Wensell, H. Krakauer. Comparison of [111] and [001] B-site stacking order in PZN-type relaxor ferroelectrics. *Journal of Physics and Chemistry of Solids*, 61:309–313, 2000.
- [59] P. P. Man. Second-order quadrupole effects on hahn echoes in fast-rotating solids at the magic angle. *Physical Review B*, 55:8406–8424, 1997.
- [60] P. P. Man. Scaling and labeling the high-resolution isotropic axis of two-dimensional multiple-quantum magic-angle-spinning spectra of half-integer quadrupole spins. *Physical Review B*, 58:2764–2782, 1998.
- [61] P. P. Man. *Encyclopedia of Analytical Chemistry*, chapter Quadrupole Couplings in Nuclear Magnetic Resonance. John Wiley & Sons Ltd, Chichester, 2000.
- [62] N. Setter, L. E. Cross. The role of B-site cation disorder in diffuse phase transition behavior of perovskite ferroelectrics. *Journal of Applied Physics*, 51:4356–4360, 1980.
- [63] L. Emsley P. Hodgkinson. Numerical simulation of solid-state nmr experiments. *Progress in Nuclear Magnetic Resonance Spectroscopy*, 36:201–239, 2000.
- [64] P. Juhas, I. Grinberg, A. M. Rappe, W. Dmowski, T. Egami, P. K. Davies.
- [65] L. Frydman S. Vega P. K. Madhu, A. Goldbourt. Sensitivity enhancement of the MQMAS NMR experiment by fast amplitude modulation of the pulses. *Chemical Physics Letters*, 307:41–47, 1999.
- [66] P. Schwerdtfeger R. Bast. The accuracy of density functionals for electric field gradients. Test calculations for ScX, CuX and GaX (X=F, Cl, Br, I, H and Li). *Journal of Chemical Physics*, 119:5988–5994, 2003.
- [67] A. Gregorovic B. Zalar C. Filipic Z. Kutnjak A. Levstik-R. Pirc R. Blinc, J. Dolinsek. Local polarization distribution and edwards-anderson order parameter of relaxor ferroelectrics. *Physical Review Letters*, 83:424–427, 1999.
- [68] B. Zalar R. Pirc R. Blinc, A. Gregorovic. ^{207}Pb NMR study of the relaxor behavior in $\text{PbMg}_{1/3}\text{Nb}_{2/3}\text{O}_3$. *Physical Review B*, 62:024104(11), 2000.

- [69] B. Zalar R. Pirc V. V. Laguta M. D. GLinchuk R. Blinc, A. Gregorovic. Nuclear magnetic resonance study of the relaxor ferroelectric $\text{Pb}(\text{Sc}_{1/2}\text{Nb}_{1/2})\text{O}_3$. *Journal of Applied Physics*, 89:1349–1354, 2001.
- [70] W. Alexander R. Ernst, G. Bodenhausen. *Principles of nuclear magnetic resonance*. Oxford University Press, 1987.
- [71] W. D. Knight R. M. Corrs. Nuclear Magnetic Resonance of ^{93}Nb in KNbO_3 . *Physical Review*, 96:1285–1293, 1954.
- [72] W. A. Anderson R. R. Ernst. Application of fourier transform sepctrscopy to magnetic resonance. *Review of Scientific Instruments*, 37:93–102, 1966.
- [73] N. F. Ramsey. Magnetic shielding of nuclei in molecules. *Physical Review*, 78:699–703, 1950.
- [74] N. F. Ramsey. Chemical effects in nuclear magnetic resonance and in diammagnetic susceptibility. *Physical Review*, 86:243–246, 1952.
- [75] S. A. Smith, T. O. Levante, B. H. Meier, R. R. Ernst. Computer Simulations in Magnetic Resonance. An Object Oriented Programming Approach. *Journal of Magnetic Resonance*, 106a:75–105, 1994.
- [76] S. Wimperis S. E. Ashbrook. Satellite-Transition MAS NMR of Spin $I=3/2, 5/2, 7/2$, and $9/2$ Nuclei: Sensitivity, Resolution, and Practical Implementation. *Journal of Magnetic Resonance*, 156:269–281, 2002.
- [77] J. Huang J. J. Fitzgerald J. S. Shore S. Prasad, P. Zhao. Pure-phase two-dimensional niobium-93 nutation spectroscopic study of lead metaniobate and the piezoelectric lead magnesium niobate. *Solid State Nuclear Magnetic Resonance*, 14:231–235, 1999.
- [78] J. Huang J. J. Fitzgerald J. S. Shore S. Prasad, P. Zhao. Niobium-93 mpmas nmr spectroscopic study of alkali and lead niobates. *Solid State Nuclear Magnetic Resonance*, 19:45–62, 2001.
- [79] C. P. Slichter. *Principles of magnetic resonance*. Springer-Verlag, 1990.
- [80] R. M. Sternheimer. Effect of the atomic core on the nuclear quadrupole coupling. *Physical Review*, 95:736–750, 1954.
- [81] R. M. Sternheimer. Effect of the atomic core on the nuclear quadrupole coupling. *Physical Review*, 105:158–169, 1957.

- [82] S. Teslic P. K. Davies I-W. Chen H. Chen T. Egami, W. Dmowski. Nature of Atomic Ordering and Mechanism of Relaxor Ferroelectric Phenomena in PMN. *Ferroelectrics*, 206-207:231–244, 1998.
- [83] P. J. Grandinetti T. M. Clark. Dependence of bridging oxygen ^{17}O quadrupolar coupling parameters on Si-O distance and Si-O-Si angle. *Journal of Physics: Condensed Matter*, 15:S2387–S2395, 2003.
- [84] U. Bismayer, V. Devarajan, P. Groves. Hard-mode Raman spectroscopy and structural phase transition behavior in the relaxor ferroelectric lead scandium tantalate, $\text{Pb}(\text{Sc}_{0.5}\text{Ta}_{0.5})\text{O}_3$. *Journal of Physics, Condensed Matter*, 1:6977–6986, 1989.
- [85] U. Piantini, O. W. Sorensen, R. R. Ernst. Multiple Quantum Filters for Elucidating NMR coupling Networks. *Journal of the American Chemical Society*, 104:6800–6801, 1982.
- [86] W. Dmowski, M. K. Akbas, P. K. Davies, T. Egami. Local structure of $\text{Pb}(\text{Sc}_{1/2}\text{Ta}_{1/2})\text{O}_3$ and related compounds. *Journal of Physics and Chemistry of Solids*, 61:229–237, 2000.
- [87] L. J. Sham W. Kohn. Self-consistent equations including exchange and correlation effects. *Physical Review*, 140:1133–1138, 1965.
- [88] P. M. Woodward. Octahedral tilting in perovskites. i. geometrical considerations. *Acta Crystallographica B*, 53:32–43, 1997.
- [89] P. M. Woodward. Octahedral tilting in perovskites. ii. structure stabilizing forces. *Acta Crystallographica B*, 53:44–66, 1997.
- [90] H. T. Kwak Z. H. Gan. Enhancing mqmas sensitivity using signals from multiple coherence transfer pathways. *Journal of Magnetic Resonance*, 168:346–351, 2004.
- [91] P. J. Grandinetti Z. H. Gan. Rotary resonance in multiple-quantum magic-angle spinning. *Chemical Physics Letters*, 352:252–, 2002.
- [92] S. K. Zaremba. Good lattice points, discrepancy, and numerical integration. *Ann. Mat. pura appl.*, 73:293–317, 1966.

VITA

William J Brouwer

William Brouwer was born on June 11, 1976 in Brisbane, Australia. Since an early age, his parents and family fostered a deep and abiding interest in the physical universe and it's workings. He began his primary education at Aspley State School in 1982, secondary education at Wavell State High School in 1989 and tertiary education at the University of Queensland in 1994. William graduated with a Bachelor of Science in 1998, a Bachelor of Science with Honors Class IIA in 1999. In 2000 William entered the PhD program at the College of William and Mary and completed it's requirements in 2005. He and his wife will stay in the United States to pursue further research and hope someday to return to Australia.